WATER FILTRATION AND MACROMOLECULAR TRANSPORT IN THE ARTERY WALL

by

Yaqi Huang

A dissertation submitted to the Graduate Faculty

in Engineering in partial fulfillment of

the requirements for the degree of Doctor of Philosophy.

The City University of New York

1996

This manuscript has been read and accepted by the Graduate Faculty in Engineering in satisfaction of the dissertation requirement for the degree of Doctor of Philosophy.

8/25/96
Date

Professor Sheldon Weinbaum
Chair of Examining Committee

8/26/96
Data

Professor Gerard G. Lowen
Executive Officer

Professor Shu Chien
(University of California, San Diego)

Professor Kung-ming Jan
(Columbia University, College of Physicians and Surgeons)

Professor Roberto Mauri

Professor David Rumschitzki

Professor Sheldon Weinbaum

Supervisory Committee

The City University of New York

Abstract

WATER FILTRATION AND MACROMOLECULAR TRANSPORT IN THE ARTERY WALL

by

Yaqi Huang

Advisors: Professor Sheldon Weinbaum

Professor David Rumschitzki

Theoretical and experimental studies are presented in this dissertation to describe water filtration and macromolecular transport in the artery wall, especially in the subendothelial intima, and to reveal the roles that the thin intima and the internal elastic lamina (IEL) with its fenestrae play in modulating this transport. This transport is believed to be closely related to prelesion events associated with atherogenesis.

In Chapter 2 we propose a new model for the growth of cellular level macromolecular leakage spots in the arterial intima. This model differs from previous studies in that we model and calculate in an ab initio manner the intimal transport parameters based on Frank and Fogelman's (1989) ultrastructural observations of the subendothelial proteoglycan matrix. Using a heterogeneous fiber matrix theory the model predicts that the Darcy permeability and macromolecular diffusivity of the subendothelial intima are two orders of magnitude larger than the corresponding values measured in the media. Numerical results show that convection parallel to the

endothelium is a very significant transport mechanism for macromolecules in the intima in a large region surrounding the leaky cleft. The predictions for the early-time spread of the HRP leakage spots in the intima and the high LDL concentration region surrounding the leaky cell are in close agreement with the experimental measurements (Chuang *et al.*, 1990; Truskey *et al.*, 1992).

In Chapter 3 we consider for the first time the effect of the intimal compaction on the total hydraulic conductivity of the intact artery wall due to changes in the transmural pressure. Our new hypothesis suggests that the compaction due to pressure loading of the proteoglycan matrix in the arterial intima near fenestral pores of the IEL leads to a narrowing of the pore entrance area and a large decrease in the local intrinsic Darcy permeability of the matrix. To quantitatively assess the feasibility of this mechanism, a local two-dimensional model is proposed to study the filtration flow in the vicinity of the fenestral pores in a compressible intima. This model predict that there is a marked non-linear steepening of the intimal pressure profiles near the fenestral pores, which can cause the endothelial indentations in these regions when the intima thins at higher lumen pressures.

In Chapter 4 we design a new *in situ* experiment to characterize the IEL's fenestrae in rat aorta, to test whether intimal compression due to transmural pressures occurs and to see if this compression is large enough to account for the observed pressure-induced changes in artery wall hydraulic conductivities (Tedgui and Lever, 1984; Baldwin and Wilson, 1993). Electron micrographs of the aorta sections show that the subendothelial intima is, indeed, very compressible. We have measured a near fourfold intimal compaction in rat thoracic aorta at 100 mm Hg compared to its initial

thickness at 0 mm Hg. In both light and electron microscopic observations. we find numerous sites where the endothelium puckers into the fenestral pores at 100 mm Hg. These observations are consistent with the intimal compaction hypothesis and the predictions of our theoretical model.

To my family

Acknowledgments

I would like to express my deepest gratitude and appreciation to my mentor, Professor Sheldon Weinbaum and co-mentor, Professor David Rumschitzki. While working on this research, I benefitted very much from their constant support, guidance and encouragement.

My sincere thanks also to Dr. Kung-ming Jan for his guidance and assistance during the course of my experimental study at the College of Physicians and Surgeons, Columbia University and to Professor Shu Chien, University of California at San Diego, for his advice and support during this research. I also wish to thank Professor Roberto Mauri for his agreeing to serve as a member of my supervisory committee.

I am very grateful to the American Society of Mechanical Engineers (ASME) for my 1996 Melville Medal Award and to the Bioengineering Division of ASME for my 1995/1996 Best Paper Award. I also wish to extend my gratitude to the Center for Biomedical Engineering, a consortium of The City College School of Engineering /CUNY Medical School, CUNY Graduate School and University Center, Hospital for Joint Diseases Orthopaedic Institute/New York University School of Medicine and Hospital for Special Surgery/Cornell University Medical College, for my 1996 Harold Shames Biomedical Engineering Award.

This research is supported by USPHS research grant HL19454 from the National Heart, Lung, and Blood Institute and by grants CBT-8803116 and CTS-8658147 (to D.R.) from the National Science Foundation.

Contents

List of Symbols x

List of Figures xviii

List of Tables xxii

1 Introduction **1**

2 A Fiber Matrix Model for the Growth of Macromolecular Leakage Spots in the Arterial Intima **22**

2.1 Major Difference between the Current Model and Model in Yuan *et al.* (1991) 23
2.2 Mathematical Formulation 25
2.2.1 Model for the Intima 26
2.2.1.1 Fiber Matrix Model in the Subendothelial Intima 27
2.2.1.2 Relationship between Horizonal Velocity and Pressure Gradient 33
2.2.1.3 Filtration Boundary Value Problem for the Intima 35
2.2.2 Model in the Media 41
2.3 Solution for Water Velocity and Pressure Distribution 43
2.4 Results 44
2.4.1 Parameter Values 44
2.4.2 Permeability and Diffusion Coefficient in the Intima 45
2.4.3 Fiber Boundary Layer Effect 47
2.4.4 Pressure Distribution and Resistance of IEL 48
2.4.5 Peclet Number in the Intima 49
2.4.6 Early Time Convective Growth of Leakage Spots in the Intima 51
2.4.7 Structure of the Normal Endothelial Cleft 54
2.4.8 Time Dependent Intimal Concentration Profiles Around Leakage Sites 56
2.4.9 Liposome Growth 60
2.5 Discussion 61

3 A Fiber Matrix Model for the Filtration through Fenestral Pores in a Compressible Arterial Intima **76**

3.1 Introduction 76
3.2 A New Intimal Compaction Hypothesis 79

3.3 Basic Filtration Model for Fenestral Pores 79
3.3.1 Filtration in the Intima and Media 84
3.3.2 Matching Conditions at the IEL Fenestra 86
3.4 Solution of the Boundary Value Problem 87
3.5 Parameter Values 89
3.5.1 Geometric Parameters 89
3.5.2 Hydraulic Conductivities 90
3.6 Results 93
3.6.1 Thickness Dependence of the Darcy Permeability 93
3.6.2 Pressure Drop across the IEL 94
3.6.3 Pressure and Velocity Profiles in the Intima and the Media 95
3.6.4 Relative Resistance of the Intima plus IEL and the Media 96
3.6.5 Pressure-dependent Hydraulic Conductivity 98
3.6.6 Changes of HRP Spot Sizes with Time for Different Lumen Pressures 101
3.7 Discussion 103

4 Structural Changes in Rat Aortic Intima due to Transmural Pressure 121

4.1 Introduction 121
4.2 Methods 123
4.2.1 Animal Experiments 123
4.2.1.1 Aorta Preparation 123
4.2.1.2 Light and Electron Microscopic Observations 124
4.2.2 Quantitative Stereology 125
4.2.2.1 Fractional Area of Fenestral Pores 125
4.2.2.2 The Average Pore Diameter 126
4.2.2.3 Model for Diameter Distribution of Pores 130
4.3 Results 131
4.3.1 Endothelial Indentation 131
4.3.2 The Changes of Intimal and Wall thickness with Pressure 132
4.3.3 Fractional Area and Average Diameter of the Fenestral Pores 134
4.3.4 Diameter Distribution of the Fenestral Pores 135
4.4 Discussion 135

5. Conclusion 149

Appendix A 153

Appendix B 157

Bibliography 160

List of Symbols

Chapter 2:

a	fiber radius
a_f	radius of the fenestra
B	the half width of the wide portion of a normal cleft
C	concentration distribution
D_f	free diffusion coefficient of a solute
D_i	diffusivity of the intima
D_{rm}	lateral diffusion coefficient in the media
D_{zf}	diffusion coefficient in the fenestra
D_{zj}	diffusion coefficient in the leaky cleft
D_{zm}	normal diffusion coefficient in the media
f_x	retardation coefficient in region x
G	Kozeny constant
K_p	Darcy permeability of the intima
$K_{p(CG)}$	Darcy permeability of a pure collagen matrix
K_{peff}	effective Darcy permeability that takes into account the effect of the uper and lower viscous boundary layers
K_{pf}	Darcy permeability of the fenestrae
$K_{p(PG)}$	Darcy permeability of a pure proteoglycan matrix
K_{pm}	Darcy permeability of the media

L_1 distance between the protein strand and the lumen in the nomal cleft

L_2 depth of the pores in the protein strands of the normal cleft

L_3 distance between the protein strand and albuminal margins of the normal cleft

L_i thickness of the intima

L_j depth of the leaky cleft

L_{jt} total junctional length per unit endothelial surface area

L_m thickness of the media

L_{pe} dimensionless hydraulic conductivity of normal endothelium

L_{pf} dimensionless hydraulic conductivity of the IEL with its fenestral pores

L_{pi}^* hydraulic conductivity of the intima

L_{pj} dimensionless hydraulic conductivity of the leaky cleft

L_{pm}^* hydraulic conductivity of the media

N total fiber number in the volum ($\pi\xi^2$ x average monomer length)

P_{eik} local Peclet number defined by $f_i r U_{ik}^*/(\gamma_i D_n)$ in the intima (k=1,2)

P_{em} average Peclet number defined by $f_m W_m^* L_m/(\gamma_m D_{zm})$ in the media

P_{lm} pressure distribution at the IEL-media interface

P_t subendothelial pressure distribution

P_{iave}^* average pressure in the intima

P_L^* pressure in the lumen

R_l effective radius of a leakage site

r_{CF} radius of central filament

r_{CG} radius of collagen

r_{CP} radius of proteoglycan core proteins (PCP)

r_G radius of glycosaminoglycans (GAG)

r_M effective radius of proteoglycan monomer

r_p radius of the pores in the protein strands of the normal cleft

r_s radius of a solute

r^* effective radius of proteoglycans

t_0 delay time before any tracer leaks into the intima

U_{ik} (k=1,2) lateral velocity component in the intima

U_x dimensionless lateral velocity in region x

V total volume of the intima

V_{CG} collagen volume in the intima

V_{PG} proteoglycan volume in the intima

W_f water velocity through the fenestra

W_{Ik} (k=1,2) local-average water velocities across the internal elastic lamina

W_I^* normal velocity distribution across the IEL

W_j water velocity across the leaky cleft

W_m^* average water velocity in the media

W_{njk} (k=1,2) local-average water velocities across the normal.intact endothelial layer

W_x dimensionless normal velocity in region x

α ratio of proteoglycan monomer to central filament lengths in the intima

β ratio of GAG to protein core lengths in the intima

γ_{wx} fractional available volume for water in region x

γ_x volume partition coefficient in the region x

$\gamma_i C_i$ average value of the intimal concentration in the region $r<3.09\ R_I$

ψ_x partition coefficient defined by γ_x/γ_{wx} in region x

Δ open spacing between fibers, δ-2a

ΔR width of the leaky cleft

δ average core protein spacing arranged in an hexagonal array

δ_p pore spacing in the protein strands of the normal cleft

ζ tortuosity factor

ε fractional void volume

ϕ cell turnover parameter defined by R_1^2/ξ^2

ϕ_l fractional area of the fenestra in the IEL, which is defined by a_f^2/ξ_l^2

μ viscosity of the fluid

μ_{eff} effective viscosity of the wide part of a normal cleft

ξ half of the average distance between sites with leaky junctions

ξ_l half of the distance between fenestrae

Superscripts and Subscripts

* denotes a dimensional quantity

$_{CG}$ collagen

$_{CP}$ core protein

$_G$ GAG

$_{lm}$ the exit of the fenestra into the media

$_l$ leaky endothelial junction

$_{li}$ the exit of the leaky junction into the intima

$_{nj}$ normal junctions

$_{PG}$ proteoglycan

x a region of the artery wall (x=i for the intima. I for the IEL. m for the media and j for the leaky junction)

Chapter 3:

C_i dimensionless HRP concentration in the intima

D_{zm}.Drm normal and lateral diffusion coefficients in the media. respectively

G Kozeny constant

h_j ratio of the thickness of the region j to the radius of fenestral pore

k elastic coefficient of the intima

K_p.K_{pi} Darcy permeability of the intima

$K_{p(CG)}$ Dacy permeability of a pure collagen matrix

$K_{p(PG)}$ Dacy permeability of a pure proteoglycan matrix

K_{pm} Darcy permeability of the media

L_{i0}^* thickness of the intima at zero lumen pressure

L_{ic}^*.L_{ic} dimensional and dimensionless critical thickness of the intima

L_j^*.L_j dimensional and dimensionless thickness of the region j

L_p hydraulic conductivity in the artery wall

L_{pe} Hydraulic conductivity in the endothelium

L_{pI} Hydraulic conductivity of the IEL plus the intima

L_{pI-m} Hydraulic conductivity of the IEL (with the intima) plus the media

L_{pm} hydraulic conductivity in the media

L_{pt} total hydraulic conductivity in the intact artery wall

N total monomer number in the volume ($\pi\xi_f^{*2}$ x average monomer length)

P_0^*, P_0 dimensional and dimensionless pressure at the edge of the wall unit in the intima, respectively

P_j^*, P_j dimensional and dimensionless pressure distribution in region j

$\bar{P}_j^*, \bar{P}_j$ dimensional and dimensionless average pressure in region j

P_L^* pressure in the lumen

P_{Lc}^* critical pressure

R^* effective radius of proteoglycan aggregates

R_l effective radius of a leaky cell

R_e hydraulic resistance of the endothelium

R_I hydraulic resistance of the IEL plus the intima

R_{I-m} hydraulic resistance of the media plus IEL

R_m hydraulic resistance of the media

r^*, r dimensional and dimensionless radial coordinate in cylindrical coordinates

r_{CF}^* radius of central filament

r_{CG}^* radius of collagen

r_{CP}^* radius of proteoglycan core proteins (PCP)

r_f^* radius of the fenestra

r_G^* radius of glycosaminoglycans (GAG)

r_M effective radius of proteoglycan monomer

U_j^*, U_j dimensional and dimensionless lateral velocity in region j

W^* averages normal velocity

W_f^* water velocity through the fenestra

W_{fi}, W_{fm} dimensionless water velocity through the fenestra

W_j^*, W_j dimensional and dimensionless normal velocity in region j

z^* normal coordinate in cylindrical coordinates

z_j dimensionless normal coordinate in the region j

α ratio of proteoglycan monomer to central filament lengths in the intima

β ratio of GAG to protein core lengths in the intima

γ_m HRP porosity of the media

ΔR width of the leaky cleft

δ average core protein spacing arranged in an hexagonal array

$\delta_{(CG)}$ average collagen spacing

ε fractional void volume (for proteoglycan)

ε_0 fractional void volume at zero lumen pressure (for proteoglycan)

$\varepsilon_{(CG)}$ fractional void volume (for collagen)

$\varepsilon_{(CG)0}$ fractional void volume at zero lumen pressure (for collagen)

ϕ cell turnover parameter defined by the fractional area of the leaky cell

μ viscosity of the fluid

ξ_1^*, ξ_1 dimensional and dimensionless wall unit radius, respectively

Superscripts and Subscripts

* denotes a dimensional quantity

$_j$ a region of the artery wall (j=i for the intima and m for the media)

Chapter 4:

A_{IEL} test area of the IEL surface

A_{pore} total pore area in A_{IEL}

a minor axe of an elliptical pore or the radius of a circular pore

b major axe of an elliptical pore

C_{pore} mean value of the pore perimeter

h wall thickness

h_0 wall thickness at 0 mm Hg pressure

L side length of a square test area

L_A length of pore perimeter per unit test area

L_L length of lineal intercepts per unit length of test line

L_{pore} total length of pore openings for a given test line

L_{pore} mean length of pore openings in L

N number of fenestral pores in the A_{IEL}

N_L number of fenestral chords per unit length of test line

p cutting probability

P_L number of intersections per unit test line length

R effective radius for the elliptical pore

r radius of aorta at 0 mm Hg pressure

r_0 radius of aorta

S IEL area per pore, defined by A_{IEL}/N

S_{pore} mean value of the pore area

ϕ fractional pore area defined by A_{pore}/A_{IEL}

List of Figures

1.1 Frank and Fogelman's (1989) ultrastructural observations of the extracellular subendothelial proteoglycan matrix that their rapid freeze etching technique preserves. 19

1.2 Small craters (arrows) appear on the endothelial surface of the canine carotid artery fixed at 80 mmHg pressure (from Lee and Chien, 1979). 20

1.3 Endothelial indentation above the fenestral pore in the rat thoracic aorta fixed at 100 mmHg pressure. EC: endothelial cell. Bar=5μm. 21

2.1 Schematic illustration of the periodic wall unit for the mathematical model of the filtration processes across the arterial wall. Fig. shows endothelial layer with leaky endothelial cell (EC) at origin. SI (subendothelial intima) with fiber matrix, and IEL (internal elastic lamina) with fenestra and media. $R_2=R_1+\Delta R$. Intimal thickness and radius of periodic wall unit are not drawn to scale. 64

2.2 Sketch of simplified fiber matrix model for calculating the void volume of the region considered. (a) is the top view of the region. δ is the average fiber spacing, r_M is the monomer radius and ξ is the radius of the cylindrical region. (b) shows the structure of proteoglycan aggregate. α is the length ratio of the total monomers to the central filament. 65

2.3a The ratio of the permeability of proteoglycans to the permeability of the collagen fibers as a function of the fractional volume of collagen. 66

2.3b Darcy permeability K_p as a function of the core protein spacing δ for $\alpha=5, \infty$ and $\beta=5, 15$, for proteoglycans with and without collagen. The curve denoted by * derives from a calculation similar to Levick's (1987). The tortuosity factor ζ is $1-(V_{CG}+V_{PG})/V$. 67

2.4 Diffusion coefficient D_i as a function of the fiber spacing δ for $\alpha=\infty$ and $\beta=5, 15$, for proteoglycans with and without collagen. The solute radius r_s is 3.0 and 11 nm, which is representative of HRP and LDL, respectively. 68

2.5 The ratio (Eq. (2.15)) of the effective permeability to the Darcy permeability (K_{peff} / K_p) as a function of the fiber spacing δ for $\alpha = \infty$ 69

and β=5. 15. for proteoglycan with and without collagen. The intima thickness L_i=100. 200nm and 500nm.

2.6 Pressure distributions in the intima (P_i) and at the IEL-media interface (P_{Im}). and the normal velocity distributions across the IEL (W_I^*). ϕ_I is the fractional area of fenestra in the IEL. L_i=200nm. P_{iave}^*/P_L^* and the Peclet number of the media were fixed at 0.47 and 4.4. respectively. for all curves. 70

2.7 The local Peclet number distribution in the lateral direction in the intima (P_{ei2}). ϕ_I is the fractional area of fenestrae in the IEL. The distance between the fenestrae is $2\xi_I$=20μm. Lpm=2.0x10^{-11} cm^2-s/g. K_p=1.0x10^{-12}cm^2 and D_i=4.12x10^{-7}cm^2/s (for HRP). L_i=0.2μm. 71

2.8 Early time growth of the leakage spots. Comparison of the theoretical prediction for the advancing edge of the convective front or convective-diffusive (curve 2) front and experimental results for growth in spot size. Curves 1.2: ϕ_I=0.002 and L_i=200nm. Curve 3: ϕ_I=0.002 and L_i=1μm. Curve 4: ϕ_I=0.01 and L_i=1μm. L_{pm}^*=3.0x 10^{-11} cm^2-s/g. δ=30nm. α=10. β=5. and t_0=25 seconds for curves 1-4. Curve 5: ϕ_I=0.001. L_{pm}=2.6x10^{-10} cm^2-s/g, K_p=K_{pm} (from Yuan. 1991). Curve 6: ϕ_I=0.005. L_{pm}=0.9x10^{-10} cm^2-s/g. K_p=K_{pm} (from Yuan. 1991). P_{em}=4.46. P_{iave}^*/P_L^*=0.47 for curves 1-3. 72

2.9 Solution for the hydraulic conductivity for normal endothelial clefts with pores in the junctional strand whose cross sectional shape is either circular with a 5.5nm radius (curve 1) or rectangular with height. 2b = 20 nm and length. 2d = 44nm (curve 2). The horizontal line is the predicted value of L_{pc} when P_{em}=4.46 and P_{iave}^*/P_L^*=0.47. 73

2.10 Time-dependent HRP concentration distributions in the intima for ϕ_I=0.002. ξ_I=20μm. K_p=1.08x10^{-12}cm^2 and D_i=4.12x10^{-7}cm^2/s (δ=30nm. α=10 and β=5). D_{zm}= 8.4x10^{-9}cm^2/s. K_{pf}=K_p. D_{zf}=D_i. L_i=200nm and t_0=25 seconds. P_{em}=4.46 and P_{iave}^*/P_L^*=0.47. γ_i=γ_I=γ_j=1 and γ_m=0.08. f_i=f_I=f_j=1 and f_m=0.3. K_{pf} and D_{zf} are the permeability and diffusivity in the fenestra. respectively. 74

2.11 LDL concentration distributions in the intima at t=10 minutes for ϕ_I=0.005. ξ_I=15μm.K_p=1.08x10^{-12}cm^2 and D_i=6.02x10^{-8}cm^2/s (δ=30nm. α=10 and β=5). D_{zm}= 5.4x10^{-10}cm^2/s. L_{pm}^*=L_{pI}^*=8x10^{-11} cm^2/s. and W_m^*=2.8x10^{-6}cm/s. K_{pf}=K_p. D_{zf}=D_i. L_i=1μm and t_0=25 seconds. γ_i=γ_I=0.5 and γ_j=1. f_i=f_I=0.75 and f_j=1. K_{pf} and D_{zf} are the permeability and diffusivity in the fenestra. respectively. 75

3.1 Schematic illustration of the local. periodic wall unit around a fenestral pore. The intima under a nondeformable endothelium is 111

compressible: L_{i0}^{*} is the initial intimal thickness at zero transmural pressure.

3.2 Sketch of simplified proteoglycan matrix model for calculating the void volume of the region considered. (a) is the top view of the region. (b) shows the structure of proteoglycan aggregate. 112

3.3 Darcy permeability K_p as a function of the intimal thickness ratio L_i^{*}/L_{i0}^{*}. 113

3.4 The local pressure distributions on the upper (intima side. P_i) and lower (media side. P_m) IEL surfaces for different intimal thicknesses. The matching conditions at the fenestral pore are equations (3.11a). (3.11b) and (3.11c) for L_i^{*}=50 nm and equation (3.11c) for all other intimal thicknesses. L_{i0}^{*}=500 nm. 114

3.5 The local pressure distributions at z^{*}=0. $0.5L_i^{*}$ and L_i^{*} in the intima for intimal thickness L_i^{*}=200 nm. L_{i0}^{*}=500 nm. 115

3.6 The ratio of the resistance R_l across the IEL plus the intima to the resistance R_m across the media as the function of L_i. 116

3.7 The comparison between the L_{pl} value predicted by the present model and that obtained using the previous model in Huang *et al.* (1994). L_{pl-m}=5.32 x 10^{-8} cm/s/mmHg at $L_i^{*}=L_{i0}^{*}$=500 nm. 117

3.8 The non-linear relationship between the lumen pressure and the intimal thickness. L_{pm}=11.0 x 10^{-8} cm/s/mmHg. L_{pe}=18.0 cm/s/mmHg and k=22. 118

3.9 Comparison of the model's pressure-dependent hydraulic conductivity in the intact artery wall with the experimental measurements from Tedgui and Lever (1984) and Baldwin and Wilson (1993). 119

3.10 The predicted time dependent HRP spot sizes for several different transmural pressures in the rabbit arterial intima. L_{pm}=11.0 x 10^{-8} cm/s/mmHg. L_{pe}=18.0 cm/s/mmHg and k=22. R_l=15 μm. 120

4.1 Schematic diagram of experimental setup for the perfusion *in situ* under a controlled pressure. 139

4.2 (a): the IEL surface with the fenestral pores cut by the thin strip: (b) Measured $L_{pore}(x)$ and the mean value L_{pore}. 140

4.3 Schematic illustration of the geometrical parameters showing elliptical pores in a pressurized aorta. 141

4.4	Serial section light micrographs traversing one fenestral pore. The thickness of each section is 200 nm. Magnification x 920.	142
4.5	Model for deriving the relationship between the measured data obtained from the transverse sections. which are random chords across the pore. and the real diameters of the pores.	143
4.6a	Electron micrograph of a typical endothelial indentation above the fenestral pore in the rat thoracic aorta fixed at 100 mm Hg pressure. Magnification x 12,000.	144
4.6b	Light micrograph of a typical endothelial indentation above the fenestral pore in the rat thoracic aorta fixed at 100 mm Hg pressure. Magnification x 2700.	144
4.7	Light micrograph showing the shape of the IEL at 0 mm Hg pressure. Magnification x 920.	145
4.8a	Electron micrograph showing the intimal thickness for 0 mm Hg pressure. Magnification x 8,000.	146
4.8b	Electron micrograph showing the intimal thickness for 100 mm Hg pressure. Magnification x 8,000.	146
4.9	Measured data for total length of pore openings and number of pores in each test IEL line.	147
4.10	Comparison of the measured distribution of the pore dimensions and the predicted distribution of the pore diameters.	148

List of Tables

1.1a	The measured hydraulic conductivity with and without endothelium in rabbit aortas by Tedgui and Lever (1984)	12
1.1b	The measured hydraulic conductivity with and without endothelium in rabbit aortas by Baldwin and Wilson (1993)	13
2.1	Baseline values of the constants and parameters	44
2.2	The hydraulic conductivity L_{pm}^{*} of the media and the Darcy permeability K_p of the intima used in Fig. 2.8 for different ϕ_f and L_t	53
3.1	Some parameters used in the calculations for the HRP spot size	90
4.1a	Mean intimal thickness at 0 mm Hg lumen pressure	133
4.1b	Mean intimal thickness at 100 mm Hg lumen pressure	133
4.2	Fractional area and average diameter of pores	134

Chapter 1

Introduction

The macromolecular transport of lipoproteins in the artery wall, especially their spread in the subendothelial intima, is believed to be closely related to prelesion events associated with atherogenesis (Ross, 1986; Weinbaum *et al.*, 1988; Weinbaum and Chien, 1993; Nerem and Levesque, 1983). This transport has been the subject of numerous experimental (Bratzler *et al.*, 1977; Fry, 1983; Smith and Staples, 1982; Lin *et al.*, 1988, 1989, 1990; Chien *et al.*, 1988; Chuang *et al.*, 1990; Wu *et al.*, 1990; Stemerman *et al.*, 1986) and theoretical studies (Truskey *et al.*, 1981; Fry, 1985, 1987; Tzeghai *et al.*, 1986; Weinbaum *et al.*, 1985, 1988b; Wen *et al.*, 1988; Yuan *et al.*, 1991), to mention a few.

In this dissertation we wish to explore at the cellular level the relationship between water filtration and macromolecular transport in the subendothelial intima and the formation of the early foam cell lesion. The primary objectives of this research were (i) to develop theoretical methods to estimate intimal transport parameters from structural observations of intimal matrix and to predict the growth of HRP and LDL's leakage spots in the intima; (ii) to test the quantitative feasibility of a new hypothesis which proposes that intimal filtration properties can be greatly altered by compaction

due to transmural pressure; and (iii) to directly examine, using experimental methods, whether the endothelium indents over the IEL fenestral pores at higher lumen pressures, and whether the arterial intima allows for the significant compression, proposed in (ii).

Macromolecules, such as LDL, can cross the endothelium and enter the subendothelial intima. The search for the transendothelial pathway has been the subject of continuous controversy for more than two decades (see summary in Weinbaum *et al.*, 1988a; Weinbaum and Chien 1993). Until the middle of the 1980s, many investigators believed that large molecules, such as LDL, whose diameter is 22 nm, crossed the endothelium in those regions where there was denuding endothelial injury (Ross and Glomset, 1976) or enter the subendothelial tissue through vesicle translocation or connected vesicle channels (Simionescu *et al.*, 1978). However, scanning electron microscopic studies in arteries demonstrated that the endothelium is continuous, and there is no evidence of denudation, except for regions where advanced lesions were present (Davies and Bowyer, 1975; Clark and Glagov, 1976; Reidy and Schwartz, 1980). Experimental studies (Bundgaard *et al.*, 1979, 1983; Chien *et al.*, 1982; Baldwin and Chien, 1988) also suggested that vesicles are not the transendothelial pathway for LDL transport.

A relatively recent discovery has been the isolation at the cellular level of transient, macromolecular, endothelial leakage spots associated with the leaky junctions of cells that were either dying or in mitosis (Lin *et al.*, 1988, 1989; Chuang *et al.*, 1990; Truskey *et al.*, 1992). The leaky junction-cell turnover hypothesis for the large pores in arterial endothelium was first proposed by Weinbaum and co-workers (1985) on the

basis of a mathematical model in which it was demonstrated that a tiny fraction of cells with leaky endothelial clefts could account for the experimentally observed regional variations in endothelial macromolecular permeability. This hypothesis suggests that the primary transendothelial pathway for LDL transport is the transient pores associated with widely scattered. leaky junctions of cells in turnover whose interendothelial cleft and surface fiber layer are temporarily disrupted.

Stemerman *et al.*'s study (1986) gives the first experimental evidence suggesting that the macromolecular leaks might be widely scattered. Weinbaum *et al.* (1988) and Wen *et al.* (1988) developed a time-dependent diffusion models to elucidate the origin of these leakage sites at the cellular level. which led to a series of experiments (Lin *et al.*. 1988. 1989. 1990: Chien *et al.*. 1988: Chuang *et al.*. 1990: Wu *et al.*. 1990) to identify the transendothelial pathway and to confirm the leaky junction-cell turnover hypothesis. In the experiments performed by Lin *et al.* (1988. 1989). the results showed that 99% of the cells in mitotic (M) phase were associated with EBA (Evans blue albumin conjugate) leakage and that 80% of cells in M phase were leaky to LY-LDL (Lucifer yellow-LDL). These leaky cells in M phase could account for about 30% and 45% of all leakage sites for EBA and LY-LDL. respectively. Further studies (Lin *et al.*. 1990) showed that the dying or dead endothelial cells were responsible for 37% of total EBA leaky foci.

The subendothelial initiation and growth of liposomes is believed to be the triggering mechanism for monocyte entry and the formation of the early foam cell lesion (Simionescu *et al.*. 1990). Based on the experimental results (Chuang *et al.*.

1990; Frank and Fogelman, 1989; Schwenke and Carew, 1989; Simionescu *et al.*, 1990). Yuan *et al.* (1991) advanced a new hypothesis suggesting that there is a co-localization of liposome formation and cellular level endothelial leakage, and that the size and frequency of the leakage spots are directly related to the formation and growth of the subendothelial lipid liposomes. Therefore, the size of the leakage spots, which is modulated by both the lateral convection and diffusion of LDL in the intima, is crucial for estimating liposome growth.

Experiments after two hours of LDL labeling reveal that only a small fraction of the LDL molecules entering through the leaky junction bind to the proteoglycan matrix to form nucleation sites for small lipid vesicles in the subendothelial intima (Nievelstein *et al.*, 1991). The frequency of vesicle clusters formed after two hours of labeling suggest that only a few nucleation sites form in the vicinity of each leakage site. About 4 to 8 days after cholesterol-feeding begins, the extracellular concentration of LDL starts to increase non-linearly in the rabbit abdominal aorta (Schwenke and Carew, 1989). This sharp increase appears to be related to the appearance of clusters of lipid vesicles, which after 10 days of cholesterol-feeding have been observed to form large aggregates in the intima (Frank and Fogelman, 1989). From Chuang *et al.*'s (1990) experimental results one can estimate leaky junction lifetime as about one hour (Yuan *et al.*, 1991). This indicates that before the small vesicle clusters in the intima grow or fuse to form large aggregates the leaky junction must close. A leak of high LDL concentration, has, however, left small liposomes of extracellular matrix-bound LDL that dissipates over time scales that are much larger than a few days. If we

assume that LDL enters the artery wall nearly exclusively through leaky clefts. further increase in growth of a small lipid cluster will only occur when another leaky junction appears in close enough proximity for the LDL molecules entering through the latter leaky junction to reach the small lipid clusters previously formed. This is equivalent to requiring that the distance between the two leakage sites should be less than the diameter of the central region of the leakage spot. where the intimal concentration is sufficiently high.

The studies on HRP by Stemerman *et al.* (1986). Chuang *et al.* (1990) and Barakat *et al.* (1992) show that the HRP spots grow to 150-200 μm diameter after only one minute in both rabbit and rat aorta. The experiments performed in Chuang *et al.* (1990) measured the growth of subendothelial HRP spots beneath an endothelial leakage site as a function of the time after tracer injection. The HRP spot grows rapidly (on the order of minutes) and then seems to approach a plateau diameter 200 - 250 μm that. for times longer than four minutes. is hard to distinguish from the background labeling because of tracer leakage through intact clefts. However. the experiments with radioactively labeled LDL in squirrel monkey (Tompkins *et al.*. 1989) reveal a spot size that is still typically about 200 μm dia. after 30 minutes of labeling. suggesting that there may be little additional growth after four minutes. This rapid growth of the HRP spots is far greater than what could be achieved by diffusion.

Autoradiographic studies (Truskey *et al.*. 1992) with ^{125}I-LDL in the vicinity of localized endothelial leakage sites in rabbit aorta show that the average area of a mitotic leakage spot after 10 minutes is about 3000 μm^2. In these experiments. Truskey et al.

measured intimal LDL concentrations (based on the density of grain counts) of nearly 60% of the luminal concentration. They were puzzled by these measurements since these concentrations greatly exceeded the estimated available volume for LDL (<0.1) using the measured available space for ^{125}I-albumin in rabbit aorta (Tedgui and Lever. 1987).

A number of theoretical models have been developed to describe the transport processes in the artery wall in recent years (Truskey *et al.*. 1981: Fry. 1985. 1987: Tzeghai *et al.*. 1986: Weinbaum *et al.*. 1985. 1988b: Wen *et al.*. 1988: Yuan *et al.*. 1991). With the exception of Yuan *et al.* (1991). all previous models of macromolecular transport in the artery wall. whether one-dimensional (Truskey *et al.*. 1981: Fry. 1985. 1987) or two-dimensional (Tzeghai *et al.*. 1986; Weinbaum *et al.*. 1985. 1988b: Wen *et al.*. 1988). consider either diffusion alone or diffusion coupled with convection solely in a direction normal to the endothelial surface. One dimensional transport models cannot describe spot growth. and the earlier two dimensional models in which the intimal pressure is uniform in the direction parallel to the endothelium do not allow for a horizontal convection of water and solute in the intima.

Yuan *et al.* (1991) considered for the first time the nonuniform subendothelial pressure field which controls the distribution of water flux through leaky and normal clefts and the role that the IEL with its fenestra plays in modulating this distribution. The numerical results in Yuan *et al.* (1991) showed that pressure gradients parallel to the endothelium (henceforth "lateral" or "horizontal") associated with cellular level leakage sites are the dominant feature of convective-diffusive transport in the intima.

Using this non-uniform filtration model, the authors attempted to explain the rapid early-time growth of HRP leakage spots (150-200 μm dia. after 1 minute) observed in rabbit and rat aorta (Stemerman *et al.*, 1986; Chuang *et al.*, 1990). This growth was one to two orders of magnitude faster than could be achieved by diffusion. While the model in Yuan *et al.* (1991) qualitatively simulated this rapid early time growth, the predicted growth rate of the HRP spots from 30 seconds to four minutes after injection was still several times slower than the measurements in Chuang *et al.*(1990).

A major impediment to using any of the existing convective transport models of the artery wall is the absence of any experimental data for the Darcy permeability K_p or the hydraulic conductivity L_{pi}^* and for the diffusivity D_i of the intima. Because the normal intima is very thin compared to the media, it is difficult to measure transport parameters such as Darcy permeability or hydraulic conductivity separately for each region. Consequently, all existing models have assumed that K_p and D_i are the same in the intima as in the media. Experimental measurements of L_{pi}^* and D_i have been based on average values for the combined intima and media. Because of the former's small relative thickness, these average values do not properly describe the intima. In contrast, Lark *et al.*'s (1988) immunolocalization studies with monoclonal antibodies have revealed that the intima has a vastly different proteoglycan (PG) structure than the media and that the matrix in the fenestral pores of the IEL has a structure which appears to be a continuation of the intimal, rather than the medial, matrix. Both normal and thickened intimas stain intensely for chondroitin sulfate proteoglycan (CSPG) while the media only stains diffusely. Earlier studies by Wight and Hascall (1983) have

shown that smooth muscle cells in the media synthesize large amounts of both CSPG as well as the much more densely packed proteoglycan, dermatan sulfate (DSPG).

Chemical fixation causes a collapse of extracellular PG matrix. Recently, a non-chemical, ultra-rapid freezing and rotary shadow etching electronmicroscopic technique has been developed to preserve the three-dimensional structure of the PG matrix. In the first study of this nature of subendothelial matrix, Frank and Fogelman (1989) observe an unexpectedly sparse matrix with an average spacing between matrix elements of 30-40 nm (see Fig. 1.1). These numbers happen to be typical of aggregated proteoglycan monomers arranged along a central filament of hyaluronic acid. Irrespective of this identification, the observed spacing reveals that intimal matrix is far less dense than previously realized, and far less dense than the matrix in the media.

The rotary shadow freeze-etchings of the intimal matrix in Frank and Fogelman (1989) and Nievelstein *et al.* (1991) do not show the GAG sidechains of the proteoglycan monomers. This suggests that the experimental procedure either did not preserve these components of the matrix or that the chondroitin sulfate component of the GAG has condensed along the proteoglycan core protein PCP. *In vivo* one would expect the GAG sidechains to be extended due to the high negative charge density of the disaccharide units in solution. A similar difference in the appearance of the GAG is observed in *in vitro* studies of CSPG from bovine nasal cartilage (Buckwalter and Rosenberg, 1982) where carbon and nitrocellulose films were used to quantify the structural organization of CSPG. On carbon films the GAG sidechains were extended and had a spacing of typically 7-9 nm between chains, whereas on the nitrocellulose

films the GAG was condensed along the length of the PCP.

The central question for the structure of intimal proteoglycan matrix is not whether the GAG sidechains are extended, but whether they are an effective barrier to the transport of LDL and also smaller macromolecules such as HRP (6 nm dia.) whose dimensions approach the spacing of the sidechains. The collapsibility of the GAG sidechains indicates that they are highly flexible and will not be a formidable obstacle to transport unless the fibers are ordered and form a molecular sieve. If the GAG does form a molecular sieve, this transport barrier can be clearly observed as demonstrated in the recent study of Adamson and Clough (1992) of the structure of the endothelial surface glycocalyx in frog mesentery capillaries. Using ferritin (10 nm dia.) as a tracer, these investigators showed that the ferritin molecules were only able to penetrate 20 to 30 nm beyond the surface of the matrix when the perfusate contained plasma proteins. In contrast, in the presence of Ringer solution the GAG was clumped and offered little resistance to transport. Plasma proteins and in particular albumin are necessary for the GAG to be ordered. A sophisticated three-dimensional model has been developed in Weinbaum *et al.* (1992) to describe transport through this ordered GAG structure.

These discrepancies and the new experimental results summarized above have motivated a revised model of the artery wall in which the PG matrix in the intima and in the fenestral openings of the IEL have a different structure than media matrix (Huang *et al.*, 1994; Chapter 2). We have extended the random fiber matrix theory (Curry and Michel, 1980; Curry, 1984, 1986) developed for capillary permeability to a heterogeneous PG matrix which includes both proteoglycans (glycosaminoglycans

(GAG), core proteins and central filaments) as well as collagen fibrils following procedures similar to those proposed in Levick (1987). The results of this model lead to the very important prediction that the value of K_p in the intima is of the order 10^{-12} cm^2, which is two orders of magnitude larger than the measured K_p for the media (Vargas *et al.*, 1979). Similar differences are predicted for the intimal diffusion coefficient D_i. This much less dense intimal structure allows for a much larger available volume for LDL and predictions for intimal concentration that are consistent with the measurements in Truskey *et al.* (1992). The close agreement between theory and experiment for the growth of the HRP and LDL spots in the intima thus strongly supports this structural prediction.

Since the artery wall is a deformable elastic structure having internal stresses which depend on the transmural pressure, the filtration properties of the artery wall change substantially as the transmural pressure increases (Baldwin *et al.*, 1992, 1993; Lever and Sharifi, 1987; Tedgui and Lever, 1984, 1987). These changes in the geometry and the distributions of stress in the artery wall lead to changes in the filtration coefficient L_p (the ratio of the transmural flux to pressure difference) which describes the hydraulic conductivity of the artery wall per unit surface area. Experimental measurements of L_p, since they are based on lumen area, take into account the increase in radius of the artery wall with increasing transmural pressure. These measurements, however, provide only indirect information on the more detailed structural changes that occur in the arterial intima, the thin subendothelial region above the first layer of elastic lamina that comprises ~ 1% of the artery wall thickness, and

in the media. The L_p of the endothelium itself is believed to be independent of pressure unless the experimenter administers or the endothelium itself releases chemical mediators (Baldwin and Wilson, 1993).

Several investigators (Baldwin *et al.*, 1992, 1993; Tedgui and Lever, 1984) have measured the hydraulic conductivity L_p in large arteries and the effect of transmural pressure on L_p. Tedgui and Lever (1984) study the influence of transmural pressure and endothelial removal on fluid filtration across the artery wall in the rabbit thoracic aorta *in vitro* (Table 1.1a). The results show that the hydraulic conductivity of the total wall, L_p=4.00x10^{-8} cm/s-mmHg at 70 mmHg lumen pressure and 2.44x10^{-8} cm/s-mmHg at 180 mmHg lumen pressure, changes with the transmural pressure in an intact wall. In later studies Lever and Sharifi (1987) show that significant changes in L_p occurred between 70 and 100 mmHg and that there is no further change at higher pressures. In contrast, the hydraulic conductivity for a de-endothelialized artery, L_p=5.36x10^{-8} cm/s-mmHg and 5.27x10^{-8} cm/s-mmHg at 70 and 180 mmHg lumen pressure, respectively, is almost invariant with pressure.

Baldwin *et al.* (1992, 1993) have performed the most recent studies investigating the effect of lumen pressure on aortic hydraulic conductivity (Table 1.1b). The major differences between their experimental method and the experimental protocol in Tedgui and Lever (1984) is that Baldwin *et al.* first relax the smooth muscle cells with $NaNO_3$ and then perform the experiments *in situ*. The hydraulic conductivity values in Baldwin and Wilson (1993) show that for the intact artery, L_p at 50 mmHg is significantly greater than its value at higher pressures, but L_p does not vary significantly between 75

and 150 mmHg; this result is qualitatively similar to Lever and Sharifi's (1987) although the error bar in Baldwin *et al.*'s 50 mmHg value calls its significance into question. For a de-endothelialized artery and the same transmural pressures, there is a twofold increase in L_p above that for the intact vessel for transmural pressures $P_L^* \geq 75$ mmHg, which is consistent with the measurements by Tedgui and Lever (1984) for P_L^*=180 mmHg. But, the value of L_p at 50 mmHg is almost the same as that in the intact artery. In contrast to Tedgui and Lever's experiment, where the hydraulic conductivity of the de-endothelialized artery does not change, Baldwin and Wilson [3] observe a 30 percent increase in L_p for the de-endothelial artery when the pressure increases from 50 to 75 mmHg, but no change at all higher pressures. Note, however, that there is a large error bar for the measurements in the de-endothelialized artery at 50 mmHg lumen pressure in the in situ experiments. Except for the results at 50 mmHg, the results from these two studies, as summarized in Tables 1.1a and 1.1b, are basically consistent.

Table 1.1a The measured hydraulic conductivity with and without endothelium in rabbit aortas by Tedgui and Lever (1984)

Pressure	Hydraulic Conductivity $x10^8$ cm/(s·mmHg)	
mmHg	Intact endothelium	Denuded endothelium
70	4.00±1.31	5.36±1.62
180	2.44±0.80	5.27±0.84

Table 1.1b The measured hydraulic conductivity with and without endothelium in rabbit aortas by Baldwin and Wilson (1993)

Pressure	Hydraulic Conductivity $x10^8$ cm/(s·mmHg)	
mmHg	Intact endothelium	Denuded endothelium
50	7.42±4.00	7.41±4.08
75	4.14±1.67	10.19±1.91
100	4.54±0.89	10.00±2.20
125	4.26±0.51	9.66±2.20
150	5.00±0.66	10.53±2.83

To describe the pressure-dependence of the hydraulic conductivity in Tedgui and Lever (1984), Kim and Tarbell (1994) present a one-dimensional poroelastic transport model. They propose that it is the compaction of the arterial media which leads to the observed decrease in the hydraulic conductivity with increasing transmural pressures in the intact artery wall. A strain-dependent permeability function in the arterial media together with a fiber matrix theory described by Curry (1984) predicts a spatial variation of fiber size and the transmural pressure dependence of the transport properties. However, Tedgui and Lever's (1987) observation that the ^{14}C sucrose space in an intact artery wall remains essentially unchanged upon pressurization with water to 70 or 180 mmHg does not seem consistent with a compaction leading to a 40% decrease in hydraulic conductivity. In the present model we shall assume that, at least for thick walled intact arteries, there are only minor changes in the medial extracellular space with pressure. For veins and small arteries, However, Short *et al.*'s (1995) recent abstract suggests that compaction may play an important role, especially at high

pressures where the compliance of the wall is rapidly decreasing. The situation is also more complicated for de-endothelialized vessels where the effects of compaction and hydration compete (Klanchar and Tarbell, 1987).

In contrast, if the thin intima between the deformable endothelium and the IEL is compressible, the compaction of the intima in the vicinity of the fenestral pores in the IEL can change the measured hydraulic conductivity significantly as the transmural pressure in the intact artery wall increases. That is, the changes in hydraulic conductivity of the artery wall with pressure might be due primarily to the compressibility of the intima, the deformation of the endothelium and partial blockage of the fenestral pores, *rather than* to significant changes in the structural properties of the media. The present study in Chapter 3 (Huang *et al.*, 1996) examines this new hypothesis. The scanning electron micrograph in Fig. 1.2 suggests the qualitative feasibility of this concept. One observes in this micrograph, which was fixed *in situ* at 80 mmHg, that there are small crater-like indentations in the endothelial surface. The dimensions of these indentations, 2 - 4 μm diameter, are of the same order as the depressions one would anticipate if the endothelium were to deform above the fenestral pores in the more rigid internal elastic lamina under the lumen pressure. New experiments (Chapter 4) provide strong evidence in support of such endothelial indentations above the fenestral pores at higher pressure. We fixed rat thoracic aorta *in situ* at 100 mmHg transmural pressure. Using random consecutive sectioning we observe numerous indentations of the endothelium into the fenestral pores, particularly in regions where the endothelium is thin, i.e. far from the cell nuclei. Fig. 1.3 shows

a typical microphotograph of an endothelial indentation. Such indentations are absent for transmural pressures below 50 mmHg.

The experimental results regarding the intimal matrix (Frank and Fogelman, 1989; Lark *et al.*, 1988; Wight and Hascall, 1983) suggest that the intima should be more compressible than the media. Using a simple geometric model to predict the measured porosity values in the media (Tedgui and Lever, 1987), 0.42 and 0.08 for sucrose and albumin, respectively, we have estimated the average open spacing Δ between the GAG side chains of the medial proteoglycans. This simple model predicts $\Delta \approx 7$ nm. In contrast, we estimate the intimal porosity for sucrose and albumin for the relaxed artery to be 0.92~0.93 and 0.84~0.88, respectively. Thus the intima is relatively sparse and, therefore, an ideal candidate for pressure-compression.

The model in Chapter 2 (Huang *et al.*, 1994) does not take into account that an increasing lumen pressure might decrease the thickness of the intima. Instead, it treats the intimal region, considered over length scales large compared with a single endothelial cell, as a non-deformable layer with a uniform background pressure, except for regions very close to a rare (a few in 10,000) endothelial cell with a leaky cleft. It characterizes the IEL by a single parameter L_{pI} which is the ratio of the average velocity across the IEL to the difference between the intimal pressure and the pressure in the media just beneath the IEL. The expression for L_{pI} in Yuan *et al.* (1991) and Huang *et al.* (1994) derives from a local model of the flow through a single fenestra which spreads into the media and is driven by a uniform pressure in the intima. However, if the intima compresses under load, the resulting decrease of the average

fiber spacing of the intimal proteoglycan matrix can lead to a significant decrease in the intimal Darcy permeability K_p. In addition, the narrowing of the intima can radically change the character of the fenestral flow to a blocked converging flow that is driven by a significant intimal pressure gradient. Thus, consideration of intimal compressibility forces us to formulate a new local, i.e., on the scale of a single endothelial cell, model for flow through a fenestral hole in Chapter 3 (Huang *et al.*, 1996). This model will provide a new theory for L_{pl}, which is an important input into the model in Huang *et al.* (1994) for the transport in the artery wall over a much larger length scale characteristic of the several thousand cells that surround a single cellular level leakage site. This model also examines the resulting effect of transmural pressure on spot size growth.

As noted, our studies (Huang *et al.*, 1994, 1996; Yuan *et al.*, 1991) suggest that the internal elastic lamina with its fenestral pores plays a significant role in macromolecular transport. As such, the IEL structural parameters at physiological pressures are crucial parameters in artery wall transport models. Roach and co-workers have performed several *in vitro* studies on the structure of the IEL in human cerebral arteries (Campbell *et al.*, 1981), sheep thoracic aorta (Song and Roach, 1983), rabbit thoracic aorta (Potter and Roach, 1983), canine thoracic and abdominal aortas (Song and Roach, 1984) and young and old porcine aortas (Dunmore *et al.*, 1990). After removing all non-elastin tissue components with caustic agents the investigators observe the fenestrations using the scanning electron microscope to determine the shape, size and the density of the fenestral pores. But, to our knowledge there are no experiments

which show the local structural changes of the artery wall in the vicinity of the fenestral pores with the lumen pressure. However, this information is very important in understanding the changes in the transport properties of the artery wall with increased lumen pressure.

This dissertation includes three major chapters, one devoted to each of the three related principle objectives mentioned at the beginning of this Introduction. In Chapter 2, we develop a heterogeneous fiber matrix model for the growth of cellular level macromolecular leakage spots in the arterial intima. The theoretical approach directly models and calculates in an ab initio manner the intimal transport parameters using direct ultrastructural observations of subendothelial protoglycans PG and collagen fibrils obtained from the rapid freeze etching electronmicroscopic studies of Frank and Fogelman (1989) and Nievelstein *et al.* (1991). The predictions of this mathematical model indicate that there are large differences in permeability between intimal and medial interstitial matrix. The new model predictions for the growth of HRP leakage spots show far superior agreement with experiments (Stemerman *et al.*, 1986; Chuang *et al.*, 1990) than the initial model for intimal transport in Yuan *et al.* (1991).

Chapter 3 advances a new hypothesis for the structural changes in the intima that lead to the markedly different responses in L_p observed when an intact or denuded artery wall is subject to increasing transmural pressures (Baldwin *et al.*, 1992, 1993; Tedgui and Lever, 1984). It proposes a local two-dimensional model for the filtration through fenestral pores in a compressible intima to test the quantitative feasibility of this hypothesis. This model considers the variation of the Darcy permeability of the

collagen-proteoglycan matrix as a function of intimal compaction and predicts the local velocity profiles and pressure distribution in the vicinity of the fenestra pores in both the intima and the media for prescribed changes in intimal thickness. The model also estimates the relative changes in hydraulic resistance between the IEL plus the intima and the media that result if there is intimal compression and partial blockage of the fenestral pores.

In Chapter 4. we experimentally test our hypothesis that the endothelium indents over the fenestral pores of the IEL at higher lumen pressures. and that the arterial intima allows for significant compression. We conduct our experiments at two limiting pressures 0 and 100 mm Hg, the former corresponding to the relaxed state of the intima and the latter to a physiological pressure that happens to be in the range where the observed hydraulic conductivity dependence on the transmural pressure has become insensitive to further pressure increases (Baldwin and Wilson. 1993). In this study. we also characterize the fractional area. the average diameter and the diameter distribution of the IEL fenestral pores in the rat thoracic aorta at 0 and 100 mm Hg.

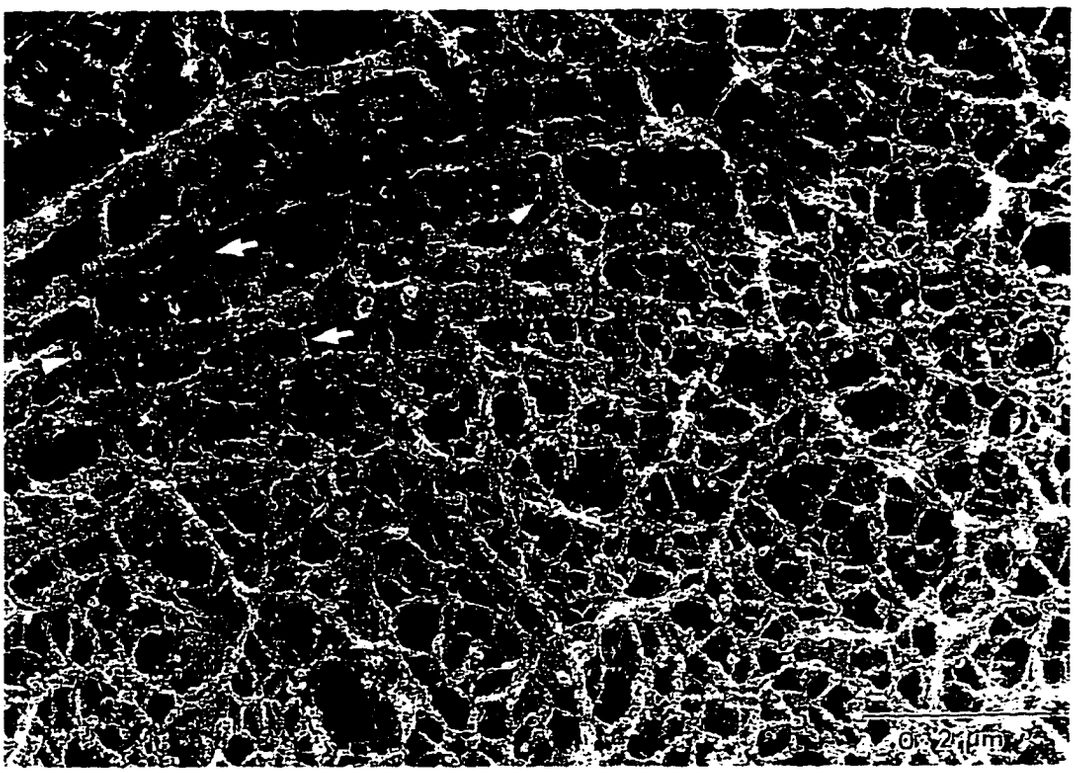

Fig.1.1 Frank and Fogelman's (1989) ultrastructural observations of the extracellular subendothelial proteoglycan matrix that their rapid freeze etching technique preserves.

Fig.1.2 Small craters (arrows) appear on the endothelial surface of the canine carotid artery fixed at 80 mmHg pressure (from Lee and Chien, 1979).

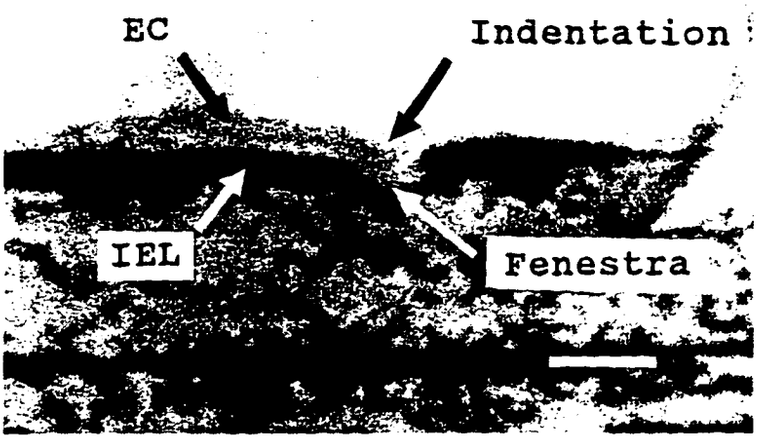

Fig.1.3 Endothelial indentation above the fenestral pore in the rat thoracic aorta fixed at 100 mmHg pressure. EC: endothelial cell. Bar=5μm.

Chapter 2

A Fiber Matrix Model for the Growth of Macromolecular Leakage Spots in the Arterial Intima

In this chapter, a new model is presented for the growth of cellular level macromolecular leakage spots in the arterial intima. Using a heterogeneous fiber matrix theory which includes proteoglycan and collagen components, we first develop a model to predict intimal transport parameters based on Frank and Fogelman's (1989) ultrastructural observations of the extracellular subendothelial proteoglycan matrix that their rapid freeze etching technique preserves. The predicted distributions of the local velocities, pressures, Peclet numbers and macromolecular concentrations show that convection parallel to the endothelium is a very significant transport mechanism for macromolecules in the intima in a large region surrounding the leaky cleft. The predictions of the new model for the early-time spread of the advancing convective-diffusive front from the leakage spots in the intima are in close agreement with the experimental measurements for the growth of HRP spots in Chuang *et al.* (1990). The predicted regions of high concentration surrounding the leaky cell is consistent with the recent measurements of Truskey *et al.* (1992) for LDL spot size in rabbit aorta and the hypothesis advanced in Yuan *et al.* (1991) that there is a co-localization of subendothelial liposome growth and cellular level leakage. Comparison of predicted and

experimentally measured average LDL concentration in leakage spots strongly suggests that there is significant local molecular sieving at the interface between the fenestral openings in the internal elastic lamina and the media.

2.1 Major Difference between the Current Model and Model in Yuan *et al.* (1991)

Yuan *et al.* (1991) present an idealized mathematical model based on the periodic wall unit shown in Fig. 2.1, which is a tissue cylinder of radius ξ and wall thickness L, with a cellular level leakage site at its center. The experiments with rat aorta (Lin *et al.*, 1988, 1989; Chuang *et al.*, 1990) and rabbit (Truskey *et al.*, 1992) show that leaky cells comprise less than 0.05 percent of all endothelial cells and that regions of high LDL concentration surrounding leakage sites are about 20 times this en face area. Between 25 and 30 percent of the cellular level leakages are associated with isolated cells in mitosis and two-thirds of the remaining leakage sites are associated with small clusters of cells surrounding dying cells that are in the process of sloughing off the dying cell (Lin *et al.*, 1990). As hypothesized in Weinbaum *et al.* (1988), both groups of cells have leaky junctions. However, since our calculations below are dimensionless, one can apply them to either case by simply scaling to the equivalent radius R_l of the leakage site of interest and making some minor modifications (e.g., (2.18) below does not apply to the dying cell case). Fig. 2.1 greatly exaggerates both the area occupied by the leaky cell (each leakage site is typically surrounded by 2000 nonleaky cells) and the thickness of the intima (intimal thickness varies between 0.1 and

0.5 μm in rat aorta and 0.5 to 1.0 μm in rabbit aorta and is less than one percent of media thickness).

Yuan *et al.* (1991) assume that the intima, media and fenestral openings in the IEL have the same permeability properties. The monoclonal antibody studies in Lark *et al.* (1988) and a more detailed examination of immunoperoxidase frozen sections (private communication, T. Wight) have revealed that fenestral and intimal matrix stain similarly for CSPG but that both differ distinctly from medial staining. This suggests that the PG matrix in the fenestral pores is a continuation of intimal matrix. The present model for spot size growth, which allows different permeability properties and different available volumes for the matrix in each of these three regions and calculates many of these from first principles, supports this conclusion.

Another important difference between the present model and the model in Yuan *et al.* (1991) is the use of a Brinkman equation to describe the fiber boundary layer effect at the upper (endothelial) and lower (IEL) surfaces of the intima. Since the thickness of the intima, which can be as little as 0.1 to 0.2 μm in rat aorta, is only several times greater than the fiber spacing, the fiber boundary layer effect can be important, and the Brinkman equation (Bird *et al.*, 1960; Ethier and Kamm, 1989), which satisfies no-slip conditions at these upper and lower boundaries, can account for this effect approximately. Tsay and Weinbaum (1991) have carefully examined the use of Brinkman's approximation for flow in a parallel channel with periodic cross-bridging fibers. Their comparison of the Brinkman approximation results and the exact solutions of the Stokes equation for this particular fiber-channel geometry shows that the

Brinkman equation is a very good approximation when the fiber aspect ratio B is greater than five.

Finally, in the earlier model (Yuan *et al.*, 1991) the authors solved two-dimensional transport equations in the media. That model's results show that the pressure distribution just under the IEL is almost uniform because of the strong effect of the IEL. Based on this observation, we introduce the simplifying assumption that the pressure distribution in the media is only a slight perturbation of a one dimensional profile. This assumption significantly simplifies the analytic solutions of the boundary value problem for the filtration flow. The new solution for the velocity field then enters the boundary value problem for the convective-diffusive transport of solute as previously formulated in Yuan *et al.* (1991), but now modified to take account of the differences in matrix structure in the intima, media and fenestral pores.

2.2 Mathematical Formulation

In contrast to macromolecules, which enter primarily through leaky junctions, water enters the intima through both the normal and leaky junctions. The pressure drop across the leaky junction, however, is much smaller than that across the normal junctions. Therefore, large lateral pressure gradients will exist in the intima between the exit of the leaky junction and the remainder of the periodic wall unit. After crossing the leaky cleft, the water flux will spread laterally in the intima and then slowly seep through the fenestral openings in the IEL. Following the ultrastructural dichotomy suggested by Fry (1985, 1987) and applied in Yuan *et al.* (1991), we divide the artery

wall into four layers as shown in Fig. 2.1: the endothelial layer, the subendothelial intima (SI), the internal elastic lamina (IEL) and the media. The loose connective tissue of the adventitia layer is not considered. We assume that the leakage sites can be arranged in a periodic surface array whose number density on a regional basis is the same as the average density in the random array. Define the cell turnover parameter ϕ describing the frequency of leakage sites as R_1^2/ξ^2, where R_1 is the effective radius of a leakage site and 2ξ is the average distance between sites with leaky junctions. The leaky cleft is approximated by a ring-source because the cleft width, R_2-R_1, is much narrower than the radius, R_1, of the leakage site.

Different subscripts distinguish each layer or interface. These are j for the leaky endothelial junction, i for the intima, I for the IEL, m for the media, and nj for normal junctions; ji and Im denote the exit of the leaky junction into the intima and the exit of the fenestra into the media, respectively.

2.2.1 Model for the Intima

In contrast to the media, which contains alternating layers of smooth muscle cells and elastic connective tissue, the lesion-free subendothelial intima is largely comprised of proteoglycan and collagen fibers. In this Chapter, we shall treat the subendothelial intima as an extracellular matrix of heterogeneous fibers and attempt to estimate the permeability K_p of this lamina from first principles.

Generally, the intima is very thin in lesion-free arteries, and can be as small as 100-200nm in rat aorta. One can readily show that the magnitude of the fiber boundary

layer thickness. in which the horizontal velocity adjusts to satisfy the no-slip conditions at the upper and lower surfaces of the intima. is of the order $K_p^{1/2}$. For slender fibers this is of the same order as the half spacing between fibers 15-20 nm observed in freeze etching. For these dimensions one needs to consider the fiber boundary layers near the underside of the endothelium and the top surface of the IEL.

2.2.1.1 Fiber Matrix Model in the Subendothelial Intima

As just noted in Chapter 1. the ultra-rapid freeze etching technique has shown that a proteoglycan matrix with typical spacing of 30-40 nm between the dominant fibers and collagen (radius r_{CG} ~ 20 nm) extends throughout the subendothelial intima. Since the collagen is much thicker than any of the proteoglycan components. and therefore its length per unit volume is much smaller. we shall treat the presence of the collagen separately from that of the proteoglycans and assume. after Levick [30]. that the resistances due to these two populations of fibers simply sum.

$$\frac{1}{K_{p(total)}} = \frac{1}{K_{p(PG)}} + \frac{1}{K_{p(CG)}} \qquad (2.1)$$

Levick calculates $K_{p(PG)}$ as the permeability of the proteoglycan matrix in the presence of collagen via an excluded volume factor. and $Kp_{(CG)}$ for the collagen similarly. In contrast. in order to avoid ad hoc geometric corrections such as excluded volume. our $K_{p(PG)}$ is the permeability of a pure proteoglycan matrix without excluded volume correction. We calculate $K_{p(CG)}$ by multiplying this quantity by the ratio $K_{p(CG)}/K_{p(PG)}$ which we obtain from an exact theory for the hydrodynamic interaction

between fibers for a simplified two-dimensional periodic fiber array. Equation (2.1) then yields the total resistance.

We start with K_p for the proteoglycans. Frank and Fogelman's (1989) images show these fibers, which are much more numerous than the collagen fibrils, to be arranged randomly. K_p for a random matrix comprised of fibers of a single radius a with a void volume ε obeys the Carman-Kozeny expression (Curry and Micheel, 1980; Curry, 1984, 1986)

$$K_p = \frac{a^2 \varepsilon^3}{4G(1-\varepsilon)^2} \tag{2.2}$$

with the Kozeny constant G. For a high fractional void volume ($\varepsilon > 0.9$), the Kozeny constant increases steeply as a function of ε. Happel and Brenner (1965) analyzed the dependence of G on ε for the beds of electrically neutral, uniform cylindrical fibers.

When the cylinders are aligned and the flow is parallel to the cylinders.

$$G_p = \frac{2\varepsilon^3}{(1-\varepsilon)[2\ln(\frac{1}{1-\varepsilon}) - 3 + 4(1-\varepsilon) - (1-\varepsilon)^2]} \tag{2.3a}$$

When the flow is perpendicular to the fibers.

$$G_r = \frac{2\varepsilon^3}{(1-\varepsilon)[\ln(\frac{1}{1-\varepsilon}) - \frac{1-(1-\varepsilon)^2}{1+(1-\varepsilon)^2}]} \tag{2.3b}$$

For cylinders orientated randomly in three planes.

$$G=\frac{2}{3}G_r+\frac{1}{3}G_p \qquad \textbf{(2.3c)}$$

The observed matrix proteoglycan constituents have non-uniform thicknesses. Therefore, in order to use the above relations, one needs to characterize the radii involved and to, define an effective radius r* for the mixture. As already stated both intact and thickened intima are rich in CSPG. Comparison of the spacing (30-40 nm) and dimensions of the fibers in the freeze etching with data from cartilage CSPG (Buckwalter and Rosenberg, 1982) strongly suggests that the observed structure probably represents proteoglycan aggregates arranged along a central filament. Such aggregates typically are comprised of a number of proteoglycan monomers (a proteoglycan core protein PCP (radius r_{CP} ~ 2.0 nm) with CSPG rich glycosaminoglycans GAG (radius r_G ~ 0.6 nm) fibers attached to it) bound to a long central filament of hyaluronic acid. We assume that the radius r_{CF} of the central filament is about 2.0 nm, the same as that of the core protein. The mean distance between the GAG fibers of a monomer seems to be independent of core protein length, whereas the mean distance between monomers in an aggregate seems to be independent of central filament length. We thus introduce the ratios β of the total GAG to total protein core lengths and α of the total protein core to central filament length in the intima (see Fig. 2.2). One can use α and β to calculate a geometric correction for this fiber distribution as described below. Since the GAG fibers are not evident in the freeze fracture picture it is not possible to accurately describe their structure. For reasons that are described in detail in Chapter 1 and the Discussion section of Chapter 2 we have treated the GAG

as if it were aggregated along the core protein of the proteoglycan monomer. While this is the appearance of the GAG in the rotary shadow freeze-etching, this appearance could be an artifact of the experimental protocol. Nevertheless the evidence in the Discussion and Chapter 1 argues that the transport resistance of the GAG is solely due to its excluded volume, which is captured by this description.

We begin by determining an effective monomer radius r_M by finding the uniform radius r_M of the fiber that would have the same total volume as the combined GAG and PCP and the same length as the PCP alone, i.e.,

$$r_M=[\beta r_G^2+r_{CP}^2]^{1/2} \tag{2.4a}$$

An effective radius r^* for the entire matrix or aggregate, if that is what the fibers in the freeze etching actually are, would be the radius of a fiber having both the same total volume and total length of the monomers and the central filament combined or

$$r^*=[\frac{\alpha r_M^2+r_{CF}^2}{\alpha+1}]^{1/2} \tag{2.4b}$$

The value calculated from equations (2.4a,b) for r^* is very close to what one would determine directly from the freeze etching if an average fiber radius were measured, even without the identification of the fibers as protein aggregates.

For estimating the fractional void volume, ε, we consider PCP with an average fiber spacing δ arranged in an hexagonal array (see Fig. 2.2). One can show that the total fiber number N in the area $\pi\xi^2$ for this hexagonal geometry is

$$N=1+3n(n+1)$$

where n=[ξ/δ] and ξ is the radius of the cylindrical region of the intima forming the periodic unit in Fig. 2.1. Since ξ>>δ. N is approximately $3n^2$.

Upon arrangement of the central filaments so that the core proteins extend the entire intimal height L_i and taking account of the additional length due to the central filaments themselves. one finds the volume fraction of proteoglycan to be

$$1-\varepsilon=(\frac{r^*}{\xi})^2(\frac{\alpha+1}{\alpha})N \tag{2.5}$$

The foregoing expressions for r* and ε combine with (2.2) to determine $K_{p(PG)}$ for (2.1). For CSPG. the predominant proteoglycan identified in the monoclonal antibody studies in Lark *et al.* (1988). typical values of α should lie in the range of 3 to 10 and β is about 5-10.

As noted above. we calculate the additional hydraulic resistance due to the collagen using the exact solution of Sangani and Acrivos (1982) for Stokes flow perpendicular to a parallel. periodic array of circular cylinders. It is well known that in Stokes flow the velocity disturbance from cylindrical fibers decays slowly with distance from the fibers and thus the dependence of the permeability on fiber radius might be significantly weaker than one might anticipate purely from geometrical considerations. Tsay and Weinbaum (1991) have shown that the simple approximation.

$$K_p=0.0527a^2(\frac{\Delta}{a})^{2.377} \tag{2.6}$$

where a is the fiber radius and Δ the open spacing between fibers. represents the exact solution in Sangani and Acrivos (1982) to within 10 percent for fiber volume fractions

of less than 0.7. It follows from (2.6) that the ratio of the resistance of the composite proteoglycan fiber of radius r* and collagen fibrils of radius r_{CG} is

$$\frac{K_{p(PG)}}{K_{p(CG)}} = \left(\frac{r_{CG}}{r^*}\right)^{0.377}\left(\frac{\Delta_{PG}}{\Delta_{CG}}\right)^{2.377} \qquad (2.7)$$

As expected, equation (2.7) shows a very weak dependence of the resistance on fiber radius. Fig. 2.3a shows the relative hydraulic resistance of collagen and proteoglycan fibers with increasing collagen volume fraction V_{CG}/V. This accurate solution for a two-dimensional fiber array agrees quite closely with the ratio of permeabilities of a pure proteoglycan and a pure collagen matrix as derived from a random fiber matrix theory, indicating that the relative resistance of the fibers does not depend on the model's assumed matrix periodicity. The fractional volume of collagen estimated from the rotary shadow freeze etching of rabbit intima in Frank and Fogelman (1989) is approximately five percent which gives a value for Δ for collagen of ~ 120 nm. Division of the previous expression for $K_{p(PG)}$ by (2.7) and combination with (2.1) provides the total resistance $1/K_p$.

Turning now to the effective diffusivities, Ogston *et al.* (1973) have derived the diffusion coefficient for a solute of radius r_s in a fiber matrix in terms of its diffusion coefficient D_f in free space as (2.8a).

$$D_i = D_f \exp\left[-(1-\varepsilon)^{1/2}\left(1+\frac{r_s}{r^*}\right)\right] \qquad (2.8a)$$

To compensate for the presence of the collagen, we replace D_f in (2.8a) by D_{feff}.

$$D_{feff}=D_f\zeta\exp[-(\frac{V_{CG}}{V})^{1/2}(1+\frac{r_s}{r_{CG}})] \quad \textbf{(2.8b)}$$

where $\zeta = 1 - (V_{CG} + V_{PG})/V$ is a tortuosity factor. For LDL and albumin, measured values for D_f are available. In the event that data for D_f is unavailable, such as for HRP, we shall appeal indirectly to the Stokes-Einstein equation (Curry, 1984).

$$D_f=\frac{kT}{6\pi\mu r_s} \quad \textbf{(2.9a)}$$

where k is the Boltzman constant and T is the absolute temperature and μ is the fluid viscosity, by taking

$$\frac{D_{f(HRP)}}{D_{f(albumin)}}=\frac{r_{albumin}}{r_{HRP}} \quad \textbf{(2.9b)}$$

Direct use of (2.9a) for, e.g., albumin over-predicts D_f by about one third.

2.2.1.2 Relationship between the Horizonal Velocity and the Pressure Gradient

Since the average spacing between fibers is significant relative to the intimal thickness, we include the fiber-induced velocity boundary layers at the top and bottom boundaries. Use of the Brinkman equation (Bird *et al.*, 1960; Ethier and Kamm, 1989; Tsay and Weinbaum, 1991) instead of Darcy's equation takes this effect approximately into account.

Let u be the velocity in the direction (r) parallel to the endothelium. Using a length scale analysis for the intima that is similar to that used in boundary layer flows, one can show that the viscous diffusion term in the r direction is much smaller than that

in the normal or z direction and that the pressure p is only a function of r. The simplified (Brinkman) equation for the horizontal velocity u(r.z) in the intima at any position (r.z) is

$$\frac{dp}{dr} = -\frac{\mu}{K_p}u + \mu\frac{\partial^2 u}{\partial z^2}, \tag{2.10}$$

where u satisfies the no-slip conditions at the top and bottom boundaries.

$$u = 0 \quad at \quad z = \pm\frac{L_i}{2} \tag{2.11}$$

Here μ is the viscosity of the fluid, and L_i is the thickness of the intima. The variation of u with r is determined by novel boundary conditions applied at the IEL and endothelial surfaces in the next section.

The solution for the horizontal velocity profile in the intima is

$$u = -\frac{K_p}{\mu}\left[1 - \frac{\cosh\left(\frac{z}{\sqrt{K_p}}\right)}{\cosh\left(\frac{L_i}{2\sqrt{K_p}}\right)}\right]\frac{dp}{dr} \tag{2.12}$$

The average velocity ū across the intima is given by

$$\bar{u} = \frac{1}{L_i}\int_{-\frac{L_i}{2}}^{\frac{L_i}{2}} u\,dz \tag{2.13}$$

Integrating equation (2.12), one obtains

$$\bar{u} = -\frac{K_p}{\mu}\left[1 - \frac{\tanh\left(\frac{L_i}{2\sqrt{K_p}}\right)}{\frac{L_i}{2\sqrt{K_p}}}\right]\frac{dp}{dr} \qquad (2.14)$$

If one defines an effective Darcy permeability that takes into account the upper and lower boundary layers as

$$K_{peff} = K_p\left[1 - \frac{\tanh\left(\frac{L_i}{2\sqrt{K_p}}\right)}{\frac{L_i}{2\sqrt{K_p}}}\right], \qquad (2.15)$$

one can write (2.14) for the average velocity ū in the same form as Darcy's law

$$\bar{u} = -\frac{K_{peff}}{\mu}\frac{dp}{dr} \qquad (2.16)$$

2.2.1.3 Filtration Boundary Value Problem for the Intima

For convenience. introduce the following dimensionless variables and parameters

$$U_x = \frac{U_x^*}{\frac{K_{peff}}{K_{pm}} L_{pm}^* P_L^*}, \qquad W_x = \frac{W_x^*}{L_{pm}^* P_L^*}, \qquad P_x = \frac{P_x^*}{P_L^*},$$

$$L_{px} = \frac{L_{px}^*}{L_{pm}^*}, \qquad r = \frac{r^*}{L_m}, \qquad z = \frac{z^*}{L_m}$$

where * denotes a dimensional quantity. U_x. W_x. P_x and L_{px} are the lateral velocity.

normal velocity, pressure, and hydraulic conductivity, respectively, in the region x, whose thickness is L_x. K_{pm} is the permeability of the media. L_{pm}^* is the hydraulic conductivity of the media and P_L^* is the pressure in the lumen. Because the thickness, L_i, of the intima is much smaller than that, L_m, of the media in the lesion-free areas of major arteries, one can integrate all physical variables across the intima in the normal direction. The resulting variables are only functions of the coordinate r. One can treat the water fluxes in the normal direction at the upper and lower boundaries of the intima simply as boundary source terms.

When water flows into the intima through the leaky cleft at $r=R_1$, the lateral velocity is directed radially inward in the region $0\le r<R_1$ (denoted by k=1) and radially outward in the region $R_2<r\le\xi$ (denoted by k=2). Since $R_2-R_1<<R_1$ or ξ, the details of the flow in the region $R_1<r<R_2$ are inconsequential and one can treat this region as a ring-source. From mass conservation,

$$\frac{dU_{ik}}{dr}+\frac{1}{r}U_{ik}=\frac{1}{\eta}[W_{njk}(r)-W_{lk}(r)] \quad , \qquad k=1,2 \tag{2.17}$$

where $\eta = (K_{perl}/K_{pm})(L_i/L_m)$ and U_{ik} (k=1,2) is the lateral velocity component in each region. W_{njk} and W_{lk} (k=1,2) are the local-average water velocities across the normal, intact endothelial layer and the internal elastic lamina, respectively.

Since there are no intact clefts in the region $0<r<R_1$, the normal velocity across the endothelium in this region is

$$W_{nj1}=0 \tag{2.18}$$

W_{nj2}, W_{lk} and the water velocity across the leaky cleft, W_j, are related to the local

pressure drop across the corresponding layer by the hydraulic conductivity relations:

$$W_{nj2}=L_{pe}(1-P_{i2}) \tag{2.19}$$

$$W_{j}=L_{pj}[1-P_{il}(R_1)] \tag{2.20}$$

$$W_{lk}=L_{pl}(P_{ik}-P_{lm}) \tag{2.21}$$

Yuan *et al.* (1991) describe in detail the models used to obtain the dimensionless hydraulic conductivities. L_{pj} for the leaky cleft. L_{pe} for the normal endothelium and L_{pl} for the IEL with its fenestral pores.

We treat the leaky cleft itself as a uniform open channel in which the resistance of matrix components is neglected. The expression for L_{pj} in Yuan *et al.* (1991) is

$$L_{pj}=\frac{(\Delta R)^2}{12\mu L_j L_{pm}^{*}} \tag{2.22}$$

where $\Delta R=R_2-R_1$ is the dimensional width of the leaky cleft and L_j is its depth (length from lumen to tissue side).

The model for L_{pe} approximates the normal endothelial cleft by an open channel with a junction strand that is impermeable to water except for small discontinuities or pores that are located along its length. The pores in the junction strand are assumed to have a cross sectional shape which is circular (Yuan *et al.*, 1991; Tsay *et al.*, 1989) or rectangular (Weinbaum *et al.*, 1992). The final expression for L_{pe} is

$$L_{pe}=[(R_{s1}+R_{s2}+R_{s3})(L_{pm}^{*})]^{-1} \tag{2.23}$$

Three resistances appear in (2.23). R_{s1} and R_{s3} are the resistances of the wide

parts of the cleft on each side of the junction strand. These resistances are calculated using Hele-Shaw flow theory to describe the spreading of the water jets from a periodic array of pores with period δ_p in an otherwise impermeable barrier. R_{s2} is the resistance of the pores in the junction strand. The expressions for R_{sk}, k=1,3, are given in Tsay *et al.* (1989) and Weinbaum *et al.* (1992) by

$$R_{sk}=\frac{3\mu_{eff}}{B^3 L_{jt}}\left[\frac{L_k}{2}+\frac{1}{d^2}\sum_{n=1}^{\infty}\frac{\tanh(\lambda_n L_k)\sin^2(\lambda_n d)}{\lambda_n^3}\right] \quad k=1,3 \qquad \textbf{(2.23a)}$$

$$\lambda_n=\frac{n\pi}{\delta_p} \qquad n=1,2,3...$$

For a circular pore of radius r_p, R_{s2} is given by

$$R_{s2}=\frac{16\mu L_2\delta_p}{\pi r_p^4 L_{jt}} \qquad \textbf{(2.23b)}$$

For a rectangular pore of height 2b and width 2d, (2.23c) replaces (2.23b)

$$R_{s2}=\frac{\mu_{eff}L_2\delta_p}{8b^2 dL_{jt}}\left[\sum_{p=0}^{\infty}\sum_{q=0}^{\infty}\frac{1}{(\theta_p\theta_q)^2(\theta_p^2+\sigma^2\theta_q)}\right]^{-1} \qquad \textbf{(2.23c)}$$

$$\theta_i=(i+\frac{1}{2})\pi, \qquad i=p,\ q, \qquad \sigma=\frac{b}{d} \quad ,$$

where L_1 and L_3 are depths between the protein strand and the lumen and abluminal margins of the cleft, respectively, L_2 and r_p are the depth and radius, respectively, of the pores in the protein strands. B is the half width of the wide portion of the cleft. $d=\pi r_p^2/(4B)$ for the circular pore and L_{jt} is the total junctional length per unit endothelial

surface area. μ_{eff} in Eq. (2.23a,c) is the effective viscosity of the wide part of the cleft: it includes the additional hydraulic resistance of possible cross-bridging fiber matrix components as proposed in the fiber matrix theory of Curry and Michel (1980). Tsay and Weinbaum (1991) derive rigorous analytic expressions for μ_{eff} for the doubly periodic fiber geometry.

L_{PI} derives from a local two-dimensional model, which uses the simplified periodic unit for the fenestral pore interaction (see Yuan *et al.*, 1991). This hydraulic conductivity is

$$L_{pI}=\frac{W_f\phi_I}{1-W_f\phi_I} \tag{2.24}$$

where $\phi_I=a_f^2/\xi_I^2$ is the fractional area of the fenestra in the IEL, a_f is the radius of the fenestra and $2\xi_I$ is the distance between the fenestrae. W_f, the water velocity through the fenestra, is

$$W_f=\frac{(L_m/L_I)(K_{peff}/K_{pm})}{1+G_0(L_m/L_I)(K_{peff}/K_{pm})} \quad , \tag{2.24a}$$

$$G_0=\phi_I+\sum_{n=2}^{\infty}\frac{2a_fJ_1(\mu_n a_f)}{\mu_n^2\coth(\mu_n)\xi_I^2J_0^2(\mu_n\xi_I)} \quad ,$$

where $J_0(x)$ and $J_1(x)$ are the zeroth and the first order Bessel functions, and the values for μ_n (n=1,2,3....) are the roots of eigenvalue equation $J_1(\mu_n\xi_I)=0$.

The dimensionless form for Eq.(2.16) is

$$U_{ik} = -\frac{dP_{ik}}{dr} \qquad k=1,2. \tag{2.25}$$

Conservation of water flux in the intima across the leaky cleft exit region $R_1<r<R_2$ requires that

$$\eta[U_{i2}(R_2) - U_{i1}(R_1)] = \Delta R W_j \tag{2.26}$$

where W_1 is neglected in the region ΔR.

The continuity of pressure at $r=R_1 \approx R_2$, the flow symmetry at $r=0$, and the periodic condition at $r=\xi$ require

$$P_{i2}(R_2) = P_{i1}(R_1) \tag{2.27}$$

$$U_{i1}(0) = 0 \tag{2.28}$$

$$U_{i2}(\xi) = 0 \tag{2.29}$$

Since $R_1 >> \Delta R$, one can consider that (2.26) and (2.27) are satisfied at $r=R_1$.

The convective-diffusion equations for solute transport across the endothelium and in the SI are given by Eqs. (21)-(34) in Yuan *et al.* (1991), where, in order to correct a systematic error in that paper, one should replace f_x in those equations by f_x/γ_x where γ_x is the partition coefficient in the region x of the artery wall.

The source of this error lies in the dimensional convective-diffusion equations from which equations such as (23) and (24) of Yuan *et al.* (1991) derive and the appropriateness of the partition coefficient γ in each of their terms. The continuity equation, being a balance on a unit volume inclusive of obstructions, contains γ, vis..

$\gamma\partial c^*/\partial t^*+\underline{\nabla}\cdot\underline{q}^*=0$, where c^* is the true concentration per unit void space. The diffusive flux must contain an area correction since obstructions reduce the cross-sectional area for diffusion. However, the convective flux term is the product of a sieving coefficient f, the concentration c^* and an average velocity. This "average" velocity is unaffected by γ and thus must be the one that leaves the volumetric flow rate unchanged. It thus convects the true concentration c^* without volumetric correction γ. With diffusivities such as those measured in Tedgui and Lever (1987) we have $\underline{q}^*=-\gamma D\underline{\nabla}c^*+f\underline{u}^*c^*$. In Yuan *et al.* (1991), the latter term erroneously contained a factor γ. Note that this changes (e.g., equations (22), (25), (28), (38), in Yuan *et al.* (1991)) the appropriate definitions of the Peclet numbers in these regions.

2.2.2 Model in the Media

In the earlier model, Yuan et al. solved a two-dimensional Darcy equation for the filtration flow in the media (Yuan *et al.*, 1991). The results show that the pressure distribution, P_{lm}, just under the IEL is almost uniform (see Fig. 6 in Yuan *et al.* (1991)) and thus the lateral velocity in the media is much smaller than in the intima because of the effect of the IEL. Based on this reasoning, we develop a simpler perturbative scheme that begins with the simplifying assumption that the pressure distribution in the media is one-dimensional and, therefore, that P_m is only a function of z. The method then modifies this assumption upon recalculation. From Darcy's law, the average water velocity W_m^0 in the media is given by

$$W_m^0 = \frac{dP_m^0}{dz} \tag{2.30}$$

where W_m^0 is uniform due to mass conservation in the media. Requiring $P_m(0)=0$ at the adventitial surface, (2.30) yields

$$P_m^0 = W_m^0 z \tag{2.31}$$

Thus at z=1, the IEL-media interface,

$$P_{lm}^0 = P_m^0(1) = W_m^0 \tag{2.32}$$

W_m^0, and hence P^0_{lm}, now follow from requiring that the flux across the media be equal to the total flux crossing the endothelium through normal and leaky junctions.

$$W_m^0 = \frac{1}{\pi \xi^2}[2\pi R_1 \Delta R W_j + \int_{R_1}^{\xi} 2\pi r W_{nj2} dr] \tag{2.33}$$

A comparison of the results obtained using the two-dimensional model for the media in Yuan *et al.* (1991) with those obtained herein for U_i, P_i or W_i, reveals that the simplifying assumption of a one-dimensional pressure distribution in the media is reasonable for all hydrodynamic variables. However, accurate tracking of the tracer concentration requires a closer accounting of radial rearrangement of the water flow at the entrance to the media. Thus we introduce P_m^1, U_m^1 and W_m^1 which derive from P_m^0 and W_m^0 by solving the two dimensional flow problem for the media alone, equations (15) - (20) of Yuan *et al.* (1991), but now the velocity W_i has been given by $W_{ik}=L_{pl}(P_{ik}-P_{lm}^0)$. This effectively closes the media's flow problem independently of that in the rest of the artery wall.

The convective-diffusion equations for solute transport in the media are given by Eqs. (35)-(40) in Yuan *et al.* (1991), where, again,one must correct f_m by f_m/γ_m. The velocity field inserted into (38) of Yuan *et al.* (1991) is now the simplified one U_m^1. W_m^1 calculated above.

2.3 Solution for Water Velocity and Pressure Distribution

Substituting $P_{1m}=W_m^0$ into equation (2.21), and solving equations (2.17) through (2.29), one can obtain an analytic solution to the boundary value problem for the velocity and pressure distribution throughout the intima

$$U_{i1}=a_1 I_1(\lambda_{1_1} r) \tag{34}$$

$$U_{i2}=a_2[K_1(\lambda_{1_2} r)-\frac{K_1(\lambda_{1_2}\xi)}{I_1(\lambda_{1_2}\xi)}I_1(\lambda_{1_2} r)] \tag{35}$$

$$P_{i1}=-\frac{1}{\lambda_{1_1}}a_1 I_0(\lambda_{1_1} r)+a_3 \tag{36}$$

$$P_{i2}=\frac{a_2}{\lambda_{1_2}}[K_0(\lambda_{1_2} r)+\frac{K_1(\lambda_{1_2}\xi)}{I_1(\lambda_{1_2}\xi)}I_0(\lambda_{1_2} r)]+a_4 \tag{37}$$

$$W_m^0=\frac{R_1\Delta RL_{pj}[1-\frac{\lambda_7}{\lambda_{1_1}}I_0(\lambda_{1_1}R_1)]+\lambda_9-\lambda_{10}\lambda_8}{\frac{\xi^2}{2}+R_1\Delta RL_{pj}[1+\frac{a_1'}{\lambda_{1_1}}I_0(\lambda_{1_1}R_1)]+\lambda_9+\lambda_{10}a_2'} \tag{2.38}$$

where a_i, a'_1 and λ_i are given in the Appendix A. In addition, the Appendix A includes

the solutions for P_m^1, W_m^1 and U_m^1.

These solutions for the velocity field are used as the input velocity in the solute transport equations for the SI and media, whose solution we discuss below.

2.4 Results

2.4.1 Parameter Values

Table 2.1 gives the baseline values of the constants and parameters used in this model. These values, obtained from the references indicated, are representative of the rabbit aorta,except where indicated.

Table 2.1 Baseline values of the constants and parameters

L_l(μm)	2.0	[84]	ϕ	0.0005	[42]
L_t(μm)	0.1∼0.5 (rat) [a] 0.5∼1.0 (rabbit) [b]		ϕ_l	0.002 ∼ 0.01 (sheep)	[61]
L_l(μm)	1.0	[88]	R_l(μm)	10(rabbit) 15(rat)	[70] [84]
L_m(mm)	0.2	[84]	ΔR(nm)	20	[84]
L_{pt}(cm/cm^2)	2000	[72]	P_{tave}^*/P_L^*	0.5	[75]
B(nm)	10	[9]	γ_m	0.08(albumin)	[67]
L_l/L_j	0.5	[72]	P_{em}	4.4(albumin)	[66]
L_2/r_p	2.0	[72]	D_{rm}/D_{zm}	3.0	[88]
r_p(nm)	5.5	[72]	D_{zm} x10^9 (cm^2/s)	7.2(albumin) 0.54 (LDL)	[67] [70]
ξ_l(μm)	2.5∼20 (sheep)	[61]	D_f x10^7 (cm^2/s)	6.8(albumin) 2.06 (LDL)	[76] [70]
μ(g/cm/s)	0.0072	[32]	P_L^* (mm-Hg)	70	[66]

[a] : S. Chien measurements

[b] : G. Truskey, private communication

$P_{iave}^{\bullet}$ is the average pressure in the intima. γ_m and $P_{em} = f_m W_m^{\bullet} L_m/(\gamma_m D_{zm})$ are the volume partition coefficient and the average Peclet number in the media, respectively. D_{zm} and D_{rm} are the normal and lateral diffusion coefficients in the media, respectively.

The retardation coefficients f_j, f_i, f_f and f_m for the leaky cleft, intima, fenestra and media relate to the partition coefficient $\psi_x = \gamma_x/\gamma_{wx}$ in region x where γ_{wx} is the fractional available volume for water (the value, γ_{wm}=0.5, for the media is roughly estimated from the measured value 0.42 for ^{14}C-sucrose in Tedgui and Lever (1987)). This relation is

$$f_x = 1-(1-\psi_x)^2 \qquad \textbf{(2.39)}$$

and is given in Curry (1984). The term $(1 - \psi_x)^2$ in (2.39) is the reflection coefficient. In our calculation, we have set γ_j=1 and have chosen $\gamma_i = \gamma_f$. For HRP, we have set γ_i=1 and have let γ_m be the measured value for albumin in Tedgui and Lever (1987). For LDL, we have estimated γ_i from the geometrical parameters α, β, δ and $r^{\bullet}$ describing the intimal proteoglycans. From random matrix theory (Curry, 1984) ψ_i is given by

$$\psi_i = \exp[-(1-\varepsilon)(2\frac{r_s}{r^{\bullet}} + \frac{r_s^2}{r^{\bullet 2}})] \qquad \textbf{(2.40)}$$

The value of γ_i is almost equal to ψ_i because $\gamma_{wi} \approx 1$.

2.4.2 Permeability and Diffusion Coefficient in the Intima

The permeability K_p of the intima follows by solving equations (2.1) through

(2.7). Fig. 2.3b shows the relationship between the total permeability K_p and the fiber spacing δ for two values of the ratio β of GAG to protein core lengths spanning the range of reasonable values. Results are shown for proteoglycans alone as well as proteoglycans augmented by collagen. The PG effective radius r^* is based on the typical values a=0.6nm. 2nm and 2nm. for glycosaminoglycans. the protein core of the proteoglycans. and the central filament. respectively. The Darcy permeability K_p increases more rapidly as a function of δ for the smaller value of β. The effect of α for $\alpha \geq 5$ is to raise K_p only very slightly. the results for $\alpha = 5$ and $\alpha = \infty$ not being significantly different. Since the collagen only occupies ~ 5% of the intimal volume. its effect is to decrease the permeability only slightly. Note that a calculation similar to Levick's leads to an almost identical result for small collagen volume fractions. The main point here is that the order of magnitude of K_p, $10^{-12}cm^2$. is a hundred fold greater than 10^{-14} cm^2. the measured value for the media (Vargas *et al.*, 1979). For the observed range of the average fiber spacing. $\delta \approx 30$-40 nm. K_p varies between 0.8 and 2.8x 10^{-12} cm^2 for β in the range 5 to 15.

Fig. 2.4 shows the diffusion coefficient D_i .obtained using Eqs. (2.8) and (2.9). as a function of the fiber spacing δ for the same r^*. for $\beta = 5$ and 15. for $\alpha=\infty$ and for solute radius r_s=3.0 and 11 nm (corresponding to HRP and LDL. respectively). For LDL we simply use the measured values of D_f in Truskey *et al.* (1992) whereas for HRP we use the measured value of D_f for albumin and then correct for the small difference in effective radius using (2.9b). For the parameters chosen. D_i in (2.8) is approximately $D_{feff}\{1-(1+r_s/r^*)(r^*/\delta)[3(\alpha+1)/\alpha]^{1/2}\}$. The figure shows that the diffusion coefficient of the

larger molecule LDL is more than a factor of five smaller than that of the HRP molecule, and that the value of the diffusion coefficient for LDL in the intima is about a hundred fold greater than 5.4×10^{-10} cm^2/s, the measured value for LDL in the media (Truskey, 1992).

2.4.3 Fiber Boundary Layer Effect

The effect of the fiber boundary layers at the endothelial and IEL surfaces is shown in Fig. 2.5, where the relationship between K_{peff}/K_p and fiber spacing δ is plotted from Eq. (2.15) for β = 5, 15, for $\alpha = \infty$, for either proteoglycan alone or PG and collagen and for L_f=100, 200 and 500 nm. Note for δ<25 nm and either value of L_f, K_{peff}/K_p >0.8 and Darcy's law provides a good approximation to the true permeation. For these values of δ, the fiber boundary layer effect is not significant and can be neglected. For larger values of δ, ε approaches 1 and K_{peff}/K_p decreases almost linearly as δ increases. This is to be expected since for large δ, $K_{peff}/K_p \approx 1-(\delta/L_f)[3(\alpha+1)/\alpha]^{1/2}$. For the smallest value of L_f, 100 nm, K_{peff}/K_p decreases the most rapidly as δ increases. As expected, the boundary layer becomes less important as L_f increases and dwarfs $K_p^{1/2}$. The relative effect of the boundary layer varies only slightly with β, becoming greater as the effective fiber radius r* decreases (β=5). For $30 \leq \delta \leq 40$ nm, K_{peff}/K_p lies in the range 0.67 to 0.80 for L_f=100nm, 0.85 to 0.92 for L_f=200nm and 0.95 to 0.97 for L_f=500 nm. The effect of collagen is very small in all cases for the assumed fiber volume fraction of 5 percent.

2.4.4 Pressure Distribution and Resistance of IEL

In this section we shall want to examine (i) the subendothelial pressure distribution P_i and (ii) how the relative hydraulic resistance of the IEL and the media change as a function of the size and spacing of the fenestral openings in the IEL. In Fig.6 we have plotted pressure distribution P_i in the intima, the pressure distribution P_{lm} at the IEL-media interface, and the normal velocity distribution W_l^* across the IEL for several different combinations of ϕ_l and a_f describing the fenestral pore geometry. In these calculations we assume, based on the monoclonal antibody studies of the intimal proteoglycans in Lark *et al.* (1988), that the extracellular matrix in the fenestral pores is a continuation of the intimal matrix and that $K_{pf} = K_p$. Note that P_i remains practically unchanged for different a_f and ϕ_l because we have required that the total resistance of the artery wall remain the same and, in accordance with observation, that roughly half the total transmural pressure drop occurs across the endothelium (Vargas *et al.*, 1979). In addition, the requirement that $P_{em}=f_m^* W_m^* L_m/(\gamma_m D_{zm})=4.4$, the measured value for albumin in rabbit aorta in Tedqui and Lever (1985), fixes the combined IEL-media resistance and therefore essentially fixes W_m and W_l^*. Thus the P_{lm} curves in Fig. 2.6 show the full effect of changing the IEL structure parameters a_f and ϕ_l on the relative resistance of the IEL and the media at fixed total combined hydraulic resistance when L_{pm}^* is adjusted so that $P_{lave}^* \approx 0.47\ P_L^*$.

The P_{lm} curves in fig. 2.6 reveal that when $\phi_l = 0.01$, the fractional resistance of the IEL to the combined resistance of IEL plus media increased from approximately 10 to 30 percent, when a_f is increased from 0.25 to 1.0μm and the pore half spacing ξ_l is

increased from 2.5 to 10 μm. Small pores more frequently spaced have a smaller hydraulic resistance than larger more infrequent pores with the same total pore area (ϕ_f = constant). When ϕ_f= 0.002 the fractional resistance of the IEL in rabbit aorta to total IEL - media resistance increased substantially being 40 percent of the total resistance when a_f = 0.25 μm and 70 percent when a_f = 1.0 μm. That is. more holes (higher ϕ_f) at constant a_f shifts a higher percentage of the resistance to the media. The size and spacing of these fenestral pores correspond closely to the size (0.46 to 2.1 μm dia.) and spacing (5 - 12 μm) observed in straight sections of sheep thoracic and human cerebral arteries (Song and Roach. 1983; Campbell *et al.*. 1981). The morphology of the fenestral holes in rat aorta has not yet been quantified to our knowledge and there could be significant differences between species as well as vessel location.

In general. there is a nonuniform distribution of W_f^* in the SI due to the non-uniformity in P_f. Whereas. W_m^0 from Eq. (2.38) requires only a continuity of the *average* water flux across the IEL rather than local continuity. the solution for W_m^1 does correct for this. The variations in W_f^* have little effect on W_m^0 because the fraction of the total water flux that enters through the leaky cleft is a small fraction of the total trans-endothelial flux. The solutions for W_f^* in Fig. 2.6. therefore. asymptote to nearly the same value for $r>>R_f$. Significant differences in W_f^* due to flow through the leaky cleft are confined to the region $r/R_f < 10$.

2.4.5 Peclet Number in the Intima

The lateral pressure variation drives a lateral spreading flow in the intima. A

local lateral Peclet number which provides a meaningful description of the local ratio of convection to diffusion is $P_{eik}=f_i r U_{ik}^{*}/(\gamma_i D_{ri})$ (see Fig. 2.7), where r is the local radius and the local Peclet number is based on the diffusion coefficient for HRP. In contrast to Fig. 2.6, where we vary the IEL structure and adjusted L_{pm}^{*} so as to keep P_{em} at the measured value of 4.4, in Fig. 2.7 we vary the structure of the IEL while holding the hydraulic conductivity of the media fixed at $L_{pm}^{*}=2.0\times10^{-11}$ cm^2-s/g and letting P_{em} vary (values given in figure). In Fig. 2.7 ϕ_f is varied at a fixed fenestral spacing of ξ_f=10 μm by changing the radius a_f of the fenestra. The value ϕ_f = 0.002, 0.005 and 0.01 corespond to a_f = 0.45, 0.71 and 1.0 μm, respectively. From this figure, we can see that although P_{ei2} changes more rapidly in the lateral direction for ϕ_f=0.01 than for ϕ_f=0.002, the lateral Peclet number of the intima is not very sensitive to the change of ϕ_f. This relative insensitivity demonstrates that K_p of the intima, and not the IEL's pore geometry or area, largely control the lateral intimal pressure gradients that determine U_{ik} and spot size.

An important prediction in fig. 2.7 is the slow horizontal decay of P_{ei}. One observes that $P_{ei} > 1$ in a region that extends up to $r/R_I \sim 10$. Although diffusion is not insignificant, one expects the growth of HRP, albumin and LDL spots to be primarily convection dominated in this region. In contrast, when the permeability properties of the intima and media were assumed to be the same, Yuan *et al.* (1991) predicted that convection is dominant only in the much smaller region $0<r<2.7R_I$, $3.5R_I$ and $5.6R_I$ for ϕ_f=0.02, 0.005 and 0.001 respectively, and the value of ϕ_f had an important effect on spot size.

2.4.6 Early Time Convective Growth of Leakage Spots in the Intima

The experiments performed in Chuang *et al.* (1990) measured the growth of subendothelial HRP spots beneath an endothelial leakage site as a function of the time after tracer injection. The size of this spot is determined by the region containing detectable tracer concentration. The threshold concentration for detectability is not known since it depends on the conditions of the histochemical reaction and photographical exposure. As described by the experimental points in Fig. 2.8. there is an initial time lag t_0 before any tracer leaks into the intima: this is simply due to the finite time it takes the dye to arrive in the aorta from the point of injection (the femoral vein). Subsequently. the HRP spot grows rapidly (on the order of minutes) and then seem to approach a plateau diameter 200 - 250 μm that. for times longer than four minutes. is hard to distinguish from the background labeling because of tracer leakage through intact clefts. However. the experiments with radioactively labeled LDL in squirrel monkey (Tompkins *et al.*. 1989) reveal a spot size that is still typically about 200 μm dia. after 30 minutes of labeling. suggesting that there is may be little additional growth after four minutes. If the growth were diffusion-dominated one would expect a much slower early growth and a continual spread even at long times. These experimental observations and our theoretical predictions in Fig. 2.7 for the local values of P_{el} suggest that one can roughly describe the early time growth of leakage spots by neglecting radial diffusion and considering only an advancing convection front whose leading edge is given by

$$\frac{dR}{dt} = U_{i2}^{*}(R) \ , \quad with \quad R=R_1 \quad at \quad t=t_0 \tag{2.41}$$

where t_0 is a delay time discussed above and U^*_{i2} is obtained from (2.35). This simple convective approximation is compared with the predictions of the full convective-diffusive model (see Fig. 2.10) and the earlier model of Yuan *et al.* (1991) in Fig. 2.8.

For the calculations in Fig. 2.8 a paucity of experimental values has forced us to assume that several input parameters measured in rabbit aorta have similar values in the rat. Thus, we have required that $P_{iave}^{*}/P_L^{*} = 0.47$ and have used the measured value for $\gamma_m = 0.08$ for radioactive albumin in Tedgui and Lever (1987). From (2.39) $f_m = 0.3$. For the intimal matrix in curves 1-4 we have assumed the length ratios $\alpha = 10$ and $\beta = 5$ for the proteoglycans and an average core protein spacing $\delta = 30$ nm. The parameters with the largest uncertainty are those that describe the structure of the IEL, the thickness L_i of the intima and P_{em}. We have, therefore, let these parameters vary to examine the range of behavior. For curves 1, 2 and 3 we have required that $P_{em} = 4.4$ (the measured value for albumin in rabbit aorta Tedgui and Lever (1985)), whereas for curve 4 we have fixed L_{pm}^{*} to be the same as for curve 3 and allowed P_{em} to vary. Curves 1, 3 and 4 describe the simple convective approximation described by equation (2.41). Curve 2 on the other hand,is the theoretically predicted effective edge of the HRP spot obtained from the full convective-diffusive solution for the concentration profiles in Fig. 2.10 that is discussed in detail in Section 2.4.8. The model input parameters for this solution are the same as those used for curve 1. Since the threshold concentration for visibility is unknown, we have selected the effective leading edge to

be the intersection with the horizontal line, C=0.13, in Fig. 2.10 that passes through the region where the gradient changes most rapidly. Table 2.2 gives a summary of the important input parameters that have been varied for the curves in Fig. 2.8.

Table 2.2 The hydraulic conductivity L_{pm}^* of the media and the Darcy permeability K_p of the intima used in Fig. 2.8 for different ϕ_f and L_i

Curve	ϕ_f	L_i (μm)	L_{pm}^* (cm^2-s/g)	K_p (cm^2)	P_{em}
1, 2	0.002	0.2	3.0×10^{-11}	1.08×10^{-12}	4.46
3	0.002	1.0	3.0×10^{-11}	1.08×10^{-12}	4.46
4	0.01	1.0	3.0×10^{-11}	1.08×10^{-12}	5.48

A biproduct of this analysis is a value for the delay time t_0. By trial and error we estimate t_0 as approximately 25 sec. Curves 1 and 3 show the effect of increasing L_i from 0.2 to 1.0 μm. The thickness of the intima can vary significantly along the aorta and is somewhat thinner in the rat than in the rabbit, though no measurements were performed in Chuang *et al.* (1990). These curves predict a roughly 30 percent decrease in spot size for the thicker intima. Curve 2 lies below curve 1 because, as explained above, we used a non-vanishing value of C to predict the visible edge of the spot . Comparing curves 3 and 4 shows the effect of ϕ_f: here as noted above, we have fixed the media permeability, $L_{pm}^* = 3 \times 10^{-11}$ cm - s/g, and let P_{em} vary to reflect the change in resistance of the IEL. The changes in spot size are relatively small, since, as observed in Fig. 2.7, the horizontal velocity in the intima (local Peclet number) is not

very sensitive to ϕ_l.

For comparison, Fig. 2.8 also presents Yuan et al.'s (1991) predictions for ϕ_l = 0.001 and 0.005, where $K_p = K_{pm}$. For $\phi_l = 0.001$ (curve 5) their value for L_{pm} $2.6x10^{-10}$ cm^2-s/g is nearly three times Vargas *et al.* 's (1979) measurements, $L_{pm}=7.9\pm2.9x10^{-11}$ cm^2-s/g, and six times Tedgui and Lever's (1984) measurements, $L_{pm}=4.02\pm1.22x10^{-11}$ cm^2-s/g. However, for ϕ_l=0.005, curve 6, they used a value $L_{pm}=9.0x10^{-11}$ cm^2-s/g, that is much more consistent with the experiment. Clearly their curves greatly underestimate the measured HRP spot size growth. In addition they do not show the delay time t_0.

It is clear from Fig. 2.8 that the new model provides for a much improved agreement for the growth of HRP spot size and that the uncertainty introduced by not having measured values for ϕ_l and L_i is at most 30 percent. This agreement suggests that the parameter values chosen to describe the matrix components in the intima are reasonable. In addition, comparison of these curves with the experimental data and extrapolation to R/R_l=1 gives a very sharp estimate for t_0 that is not directly available from the experimental data.

2.4.7 Structure of the Normal Endothelial Cleft

Even though leakage sites in the endothelium allow passage of macromolecules and water from the lumen into the intima, normal endothelium provides the principal pathway for transendothelial water transport; in fact less than 5 percent of the water flux enters through the leaky cleft. We shall examine two possible junction protein pore structures using our predicted value for the hydraulic conductivity L_{pc} of normal

endothelium. In this junction-pore model the junction strand is treated as a barrier in the interendothelial cleft that is impermeable to water except for pores that are periodically situated along its length. In the first model (Tsay *et al.*, 1989) these pores are circular and represent isolated missing proteins in the junction strand. Weinbaum *et al.* (1992) extend this model to treat periodic and random arrays of cross-bridging fibers as well as pores that are larger rectangular breaks representing several missing proteins, as observed in Bundgaard (1984) in rat heart capillaries. For this latter pore, (2.23c) replaces (2.23b) for the resistance R_{s2} of the junction strand.

The solutions in Fig. 2.9 show how the hydraulic conductivity L_{pe}^* varies as a function of pore spacing $2\delta_p$ for clefts whose junctional pores are circular (5.5 nm radius) or rectangular (2b=20 nm, 2d=44 nm) when there is no fiber matrix in the wide parts of the cleft on each side of the junction protein strand. If one requires that P_{em}=4.4 and P_{iave}^*/P_L^*=0.5, then L_{pe}^* is 8.29×10^{-9} cm/s/cm-H_2O (or 8.46×10^{-12} cm^2s/g). This value of L_{pe}^* is the horizontal line in Fig. 2.9 and its intersection with the L_{pe}^* curves for the two pore geometries determines the pore spacing, $2\delta_p$ for the rectangular pore model (2b=20nm, 2d=44nm) is approximately 70 μm, whereas $2\delta_p$ for the 5.5nm radius circular pore model is about 9 μm. The predicted value of L_{pe}^* is thus satisfied by roughly 1.4 large rectangular pores or 10 circular pores in the perimeter of an endothelial cell. For the large rectangular pore a thin fiber matrix layer would be required at the surface or the entrance to the wide portion of the cleft to provide the molecular sieve. This thin layer does not significantly alter L_{pe}^* but would filter out molecules the size of albumin or larger. For the 5.5 nm radius circular pore this fiber

filter is not necessary since the pore itself would be the molecular sieve. Future experimental investigations of the ultrastructure of normal endothelial clefts in large arteries will be required to distinguish between these models. The above value of $2\delta_p$ = 70 μm for the 44 nm rectangular breaks in the rabbit aorta is more than an order of magnitude greater than the observed pore spacing in rat heart capillaries (Bundgaard. 1984).

2.4.8 Time Dependent Intimal Concentration Profiles Around Leakage Sites

As noted in section 2.4.6. the concentration at the leading edge of the convective front can fall to very low values due to dilution at the endothelial surface arising from filtration through intact clefts and transport through the fenestral openings in the IEL. The model prediction that merits greater scrutiny is the convective-diffusive solution for the time evolution of the tracer's concentration profiles in the intima. Substituting the calculated velocity field given by equations (2.34) and (2.35) into these convective-diffusion equations (see Yuan *et al.*. 1991) and solving. one obtains the time-dependent. intimal concentration profiles surrounding the leakage sites.

In Fig. 2.10. we have plotted the time evolution of the intimal concentration profiles for the HRP spots analyzed in Fig. 2.8. We assume in this calculation that the matrix in the fenestral pores is a continuation of the matrix in the intima and has the same properties: δ = 30 nm. α = 10. β = 5. $K_p = K_{pf} = 1.08 \times 10^{-12} cm^2$ and $D_i/D_{zm} = D_{zf}/D_{zm} = 49.0$

As discussed previously. we do not know the concentration threshold for the

visibility of the HRP reaction product. but if we require this threshold to remain constant the locus of points defined by the intersection of a horizontal line representing this threshold concentration with the C profiles should trace out the advance of this visible front. The excellent agreement between theory (curve 2) and experiment in Fig. 2.8 was obtained by choosing the threshold value of C to fit the data point at t = 4 min.. but. as is clear from fig. 10. large changes in spot size growth would not occur if the threshold value of C were raised or lowered by 50 percent from the chosen value C=0.13. The choice of L_i = 0.2μm is based on recent electron microscopic studies of rat abdominal aorta by the authors.

The theoretical model can also predict the autoradiographically measured size and average intimal concentration of LDL spots observed around leaky cells in M phase in rabbit aorta in the experiments of Truskey *et al.* (1992). In these experiments. the average area of a mitotic leakage spot after 10 minutes was 2990 μm^2 and the average concentration of these intima spots. taking into account the available volume γ_i of the intima. was 0.58 times that of the lumen. The average area of the rabbit endothelial cells in Truskey *et al.* (1992). 300μm^2. corresponds to an effective radius $R_1 \approx 10\mu m$. The average spot size 2990μm^2. has an equivalent radius r = 3.09 R_1. As mentioned earlier. Truskey *et al.* were puzzled by their measurement for the average value of the intimal concentration observed in their spots. This average scaled concentration 0.58 was more than seven times larger than the intimal concentration that would be possible if γ_i were set equal to the measured value γ_m = 0.08 for albumin in Tedgui and Lever (1987). This conclusion was based on the premises that $\gamma_i = \gamma_m$ and molecular sieving

did not occur in the intima. Neither of these assumptions is correct and we shall examine in Fig. 2.11 the changes that occur when $\gamma_i \neq \gamma_m$ and an unstirred layer is created locally in the intima.

In Fig. 2.11 we have plotted five different curves for the predicted intimal LDL concentration profiles surrounding a leakage site after 10 minutes of labeling. For each curve we have required that the measured hydraulic conductivity of the IEL plus media satisfy the measured value, $L_p^* = 4x10^{-8}cm^{-2}$ s/g, in Tedgui and Lever (1984) and that the measured water velocity for a rabbit aorta with endothelium intact be $W_m^* = 2.80x10^{-6}$ cm/s, as in this same study, when $\Delta P = 70$ mm Hg. In choosing the structure of the IEL we have required that the resistance of the IEL and media be equal and hence that $L_{pm}^* = L_{pI}^* = 8x10^{-11}$ cm^2-s/g. This could be achieved with $\phi_I = 0.005$ and $\xi_I = 15\mu m$, which corresponds to a fenestral pore whose radius $a_f = 1.06\mu m$. The parameters that characterize the intimal matrix are $\alpha = 10$, $\beta = 5$, $L_i = 1\mu m$, $\delta = 30nm$ and a calculated minimum value for γ_i for LDL based on this matrix structure, which is 0.5. (It is worth remarking that this value of γ_i is still less than the measured concentration $\gamma_i C_i$ of 0.58. This is not critical because molecular sieving at the IEL-media interface allows for $C_i > 1$). The difference between the curves arises from the assumed values of γ_m and ΔR. We chose γ_m to lie in the range $0.01 < \gamma_m < 0.08$, with the upper value representing the measured value for the smaller molecule albumin, and for ΔR,we took the three values 15, 20 and 25 nm. The experiments with fluorescently tagged LDL in Lin *et al.* (1989) indicate that only a portion of the perimeter of a leaky cleft allowed the passage of LDL. In our idealized model this is accounted for by

allowing ΔR, the average cleft width, to be less than the diameter of the LDL molecule, 22nm. So, for example, reducing ΔR from 25 nm to 20 or 15 nm results in a closing of 1/2 or 5/6 of the perimeter of the leaky cleft since the flow rate goes as $(\Delta R)^3$.

The spot size and the average concentration in the region $r < 3.09\ R_l$ increase significantly as γ_m decreases. These changes readily trace to the rejection of solute at the IEL-media interface. For $\gamma_m = 0.01$, 0.03 and 0.08, $f_m = 0.04$, 0.12 and 0.3 in that order. One observes that for all three values of f_m a local unstirred layer can exist in the intima whose concentration exceeds that in the lumen. Fry *et al.* (1986) have measured this sieving behavior for LDL in deendothelialized in vitro minipig aorta. These investigators observed that for ΔP = 100 mm Hg the concentration of ^{125}I-LDL at the intimal surface was 41 percent greater than in the lumen and that for ^{125}I-albumin this increase was only 15 percent. Our predicted increases in concentration in the vicinity of the leakage site are thus quantitatively in the same range as the measured values in Fry *et al.* (1986).

Increasing ΔR from 15 to 20 to 25 nm decreases the hydraulic resistance of the leaky cleft by approximately a factor of two for each 5 nm increment. If γ_m is held fixed the effect of this increase in ΔR is to significantly broaden the spot since more solute will be swept in through the leaky cleft. Increasing ΔR also increases the concentration under the leaky cell, since the local increase in intimal pressure enhances molecular sieving. These predictions suggest that the large variations in spot size observed in Truskey *et al.* (1992) may be due to the geometry of the leaky cleft, since γ_m should not vary greatly with location. Leakage spots as large as 6000μm^2 were

observed for which $r = 4.4R_1$. This size spot easily falls within the range of parameters plotted in Fig. 2.11. The average values of $\gamma_i C_i$ in the region $r < 3.09\ R_1$ for the two upper curves in Fig. 2.11. bracket the measured value 0.58 in Truskey *et al.* (1992) although their concentration profiles do not decay sufficiently rapidly to yield a spot size of only $3R_1$. The three lower curves in Fig. 2.11. however. provide a better fit with experimental measurement of spot size. but give values of $\gamma_i C_i$ of about 0.4. Despite the fact that we seem to still be unable to match both $\gamma_i C_i$ and the spot size with one set of parameters. the results. particularly the lower three curves. provide a vast improvement over the results that would obtain if $\gamma_i = \gamma_m = 0.08$.

2.4.9 Liposome Growth

The limited growth in the leakage spot size may play an important role in determining the time scale for the development of lipid liposomes in the subendothelial intima of lipid fed rabbits. As we have mentioned in Chapter 1. since we assume that LDL enters the artery wall nearly exclusively through leaky clefts. after the earlier leaky clefts are closed further increase in growth of a small lipid clusters will only occur when another leaky junction appears in close enough proximity for the LDL molecules entering through the latter leaky junction to reach the small lipid clusters previously formed. This is equivalent to requiring that the distance between the two leakage sites should be less than the diameter of the central region of the leakage spot. where the intimal concentration is sufficiently high. Since the lifetime of a junctional leakage. which can be estimated from Chuang *et al.*'s (1990) experimental results. is one hour.

one would need to wait for 2000 hours for another cell with a leaky junction to appear on top of the initial nucleation site if ϕ=0.0005. However, our results for the three lower curves in Fig. 2.11, which correspond best with measured spot size, show that the intimal LDL concentration is greater than 0.2 in a region whose radius is $4R_l$ to $5R_l$. Therefore, about 20 cells would be contained in this region and the waiting time would be reduced to only 100 hours in order for two leakage spots to overlap. This prediction is consistent with the experimental result that there is a 4 to 8 day time lag before the extracellular concentration of LDL in the intima starts to increase rapidly for cholesterol-fed rabbits (Schwenke and Carew, 1989).

2.5 Discussion

At present there is no consensus as to the state of the GAG in the spaces that surround the matrix elements observed in the rapid freeze-etching studies (Frank and Fogelman, 1989; Nievelstein *et al.*, 1991) used to develop the present model. However, the experiments on the growth in spot size (Lin *et al.*, 1988, 1989, 1990; Chien *et al.*, 1988; Chuang *et al.*, 1990; Wu *et al.*, 1990; Stemerman *et al.*, 1986; Truskey *et al.*, 1992) and the comparison of the results of the present theory with the earlier model in Yuan *et al.* (1991) provide formidable definitive evidence that the GAG in intimal matrix is not a significant transport barrier. The autoradiographic studies (Truskey *et al.*, 1992), which show individually labelled ^{125}I-LDL particles (23 nm dia.), provide particularly compelling evidence that the GAG does not significantly obstruct the open spaces between matrix components observed in Frank and Fogelman (1989) and

Nievelstein *et al.* (1991). Figures. 5(C) and (D) in Truskey *et al.* (1992) show a typical distribution of particles surrounding a cellular level leakage site of a cell in mitosis. The LDL particles have spread over an area which is more than ten times that of an individual cell after only ten minutes of labeling *in vivo*. CSPG has side chains which have a nearly ordered spacing of roughly 8 nm when observed on two-dimensional carbon films. This is an artificial situation that might bear little resemblance to their three-dimensional configuration *in vivo*. However, it is intuitively clear that a 23 nm particle could not penetrate an ordered matrix with these dimensions when ferritin, a much small molecule, could not penetrate a related endothelial fiber matrix as noted in Chapter 1. As observed in Adamson and Clough (1992), albumin and other plasma proteins are required to order the GAG and prevent it from aggregating and these molecular components do not readily penetrate the endothelial barrier.

Further convincing evidence that the GAG is either aggregated or does not impede the transport of LDL is the fact that the average concentration of LDL particles in the vicinity of the leakage sites in Truskey *et al.* (1992) was eight fold higher than could be accounted for by the measured available volume for albumin in the media in Tedgui and Lever (1987). This magnitude of increase can not be explained by LDL attaching to intimal matrix or molecular sieving: only a very minor fraction of the LDL that enters the intima attaches to matrix, see Frank and Fogelman (1989) and Nievelstein *et al.* (1991). Also the measured increase in intimal LDL concentration due to molecular sieving was only 41 percent, and this increase only obtained for the extreme case where convection was enhanced by endothelial denudation (see also the

section 2.4.8). In view of these findings the authors have treated the GAG as if it is in an aggregated state with an enlarged effective monomer radius r_M given by Eq. (2.4a).

Before the very convincing en face Hautchen ^{125}I-LDL autoradiographic studies of Truskey *et al.* (1992) appeared, the author attempted many refinements of the original model in Yuan *et al.* (1991) where the transport coefficients for the intima were characteristic of those that would be obtained if the GAG filled the space between the proteoglycan monomers. No combination of intimal thickness, fenestral pore geometry and measured media transport properties came close to predicting the observed growth of HRP spots in the intima. In contrast, the present model provides remarkably good agreement for this growth. An intimal matrix in which an extended GAG forms the principal resistance is thus not only inconsistent with the detailed experimental observations for LDL in Truskey *et al.* (1992), but also for smaller tracer macromolecules which might be able to pass through a molecular sieve that would be formed by an extended ordered GAG matrix structure.

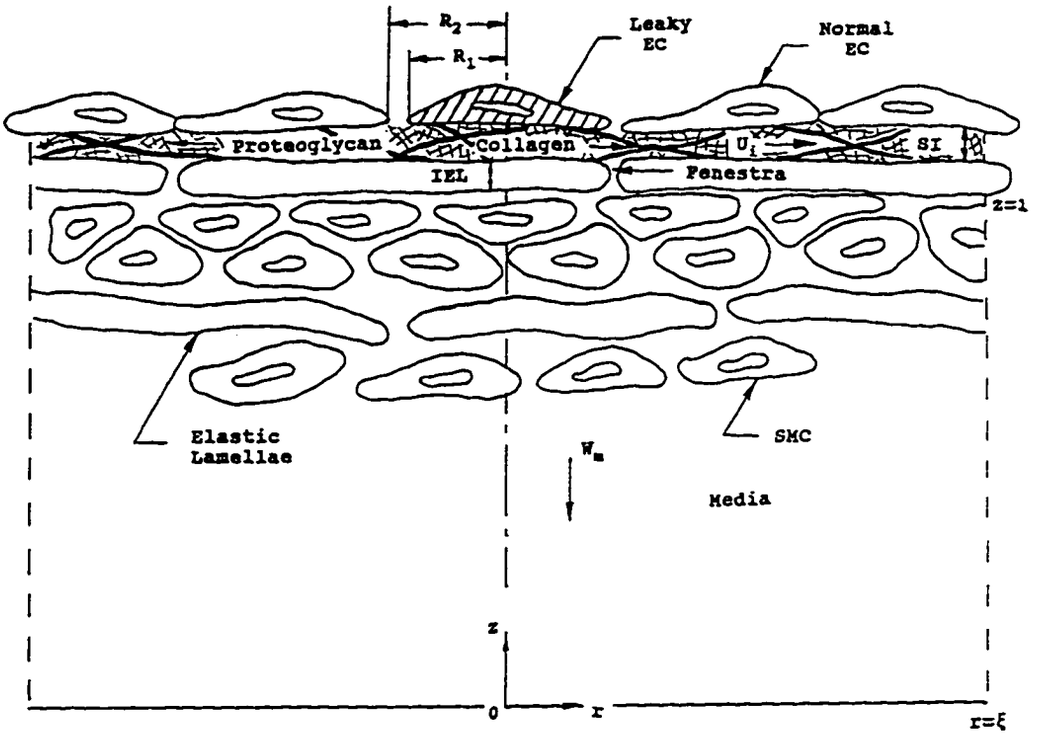

Fig.2.1 Schematic illustration of the periodic wall unit for the mathematical model of the filtration processes across the arterial wall. Fig. shows endothelial layer with leaky endothelial cell (EC) at origin, SI (subendothelial intima) with fiber matrix, and IEL (internal elastic lamina) with fenestra and media. $R_2=R_1+\Delta R$. Intimal thickness and radius of periodic wall unit are not drawn to scale.

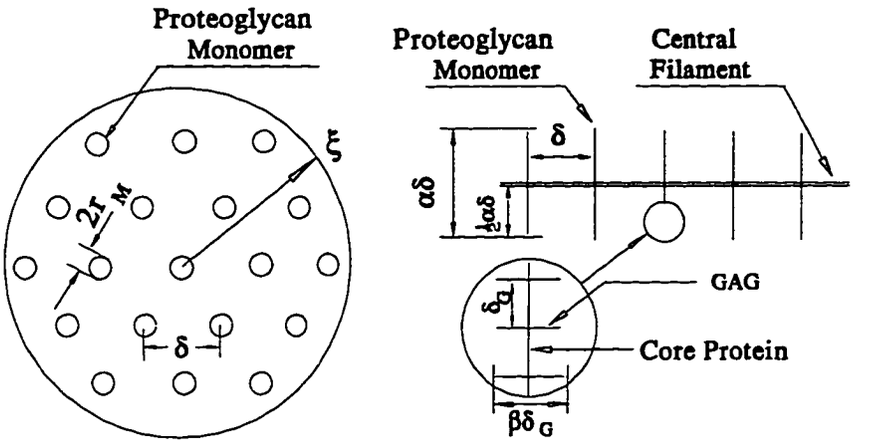

(a) Top View (b) Proteoglycan Aggregate

Fig.2.2 Sketch of simplified fiber matrix model for calculating the void volume of the region considered. (a) is the top view of the region. δ is the average fiber spacing, r_M is the monomer radius and ξ is the radius of the cylindrical region. (b) shows the structure of proteoglycan aggregate. α is the length ratio of the total monomers to the central filament.

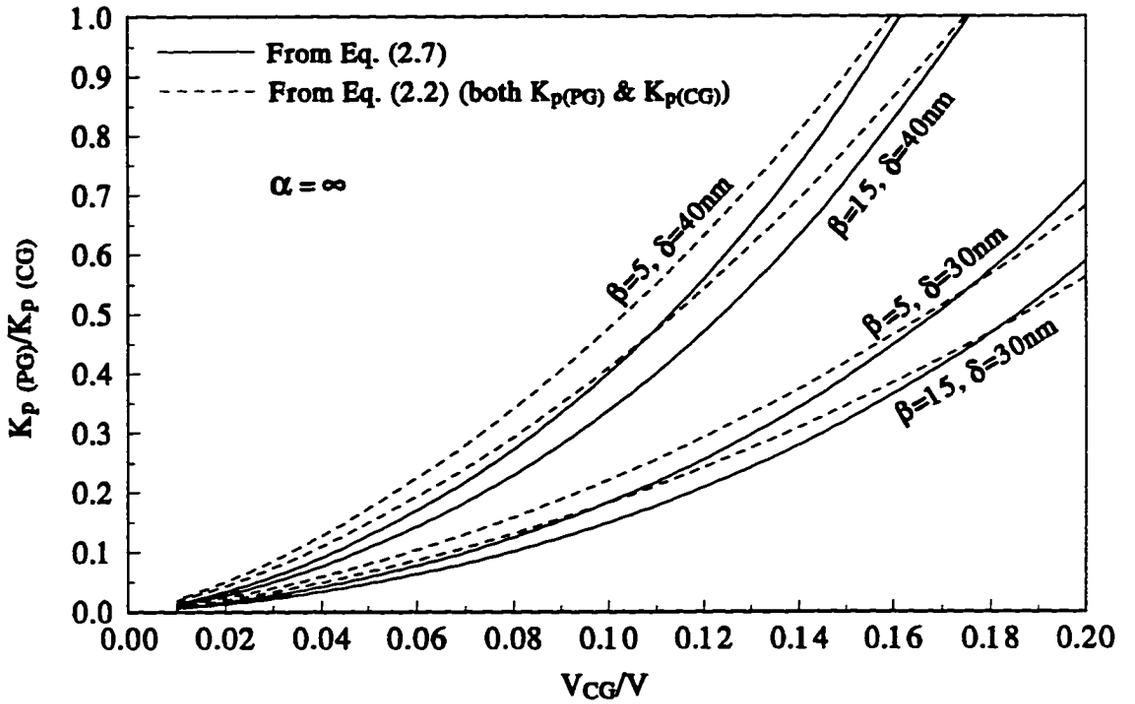

Fig.2.3a The ratio of the permeability of proteoglycans to the permeability of the collagen fibres as a function of the fractional volume of collagen.

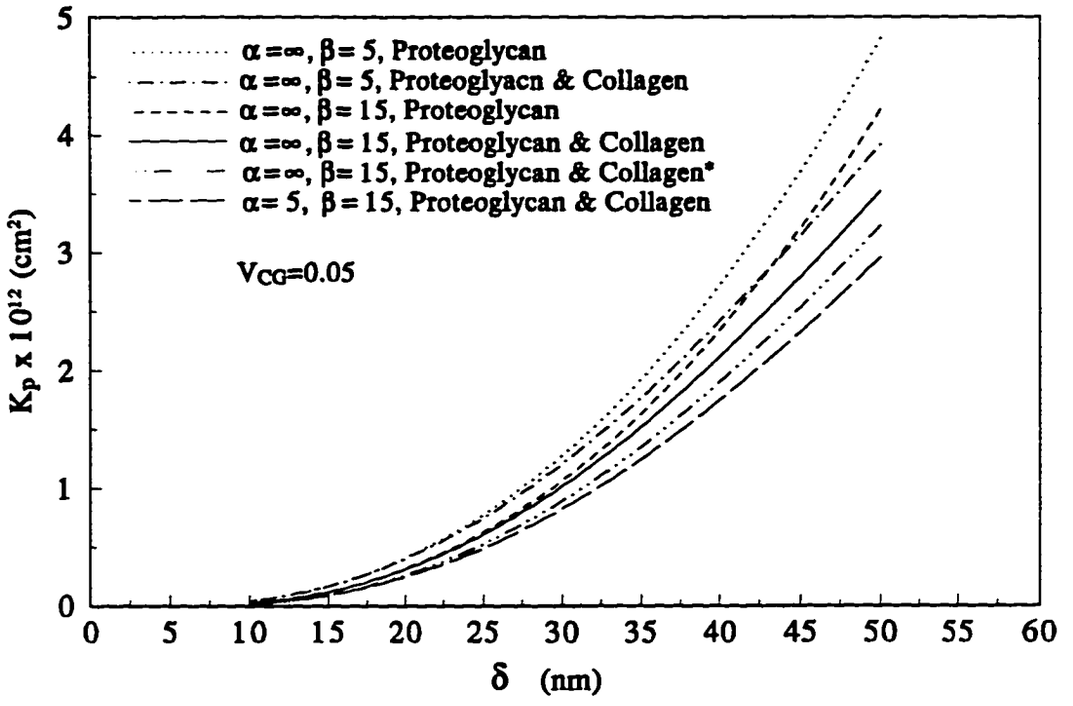

Fig.2.3b Darcy permeability K_p as a function of the core protein spacing δ for α=5, ∞ and β=5, 15, for proteoglycans with and without collagen. The curve denoted by * derives from a calculation similar to Levick's (1987). The tortuosity factor ζ is $1-(V_{CG}+V_{PG})/V$.

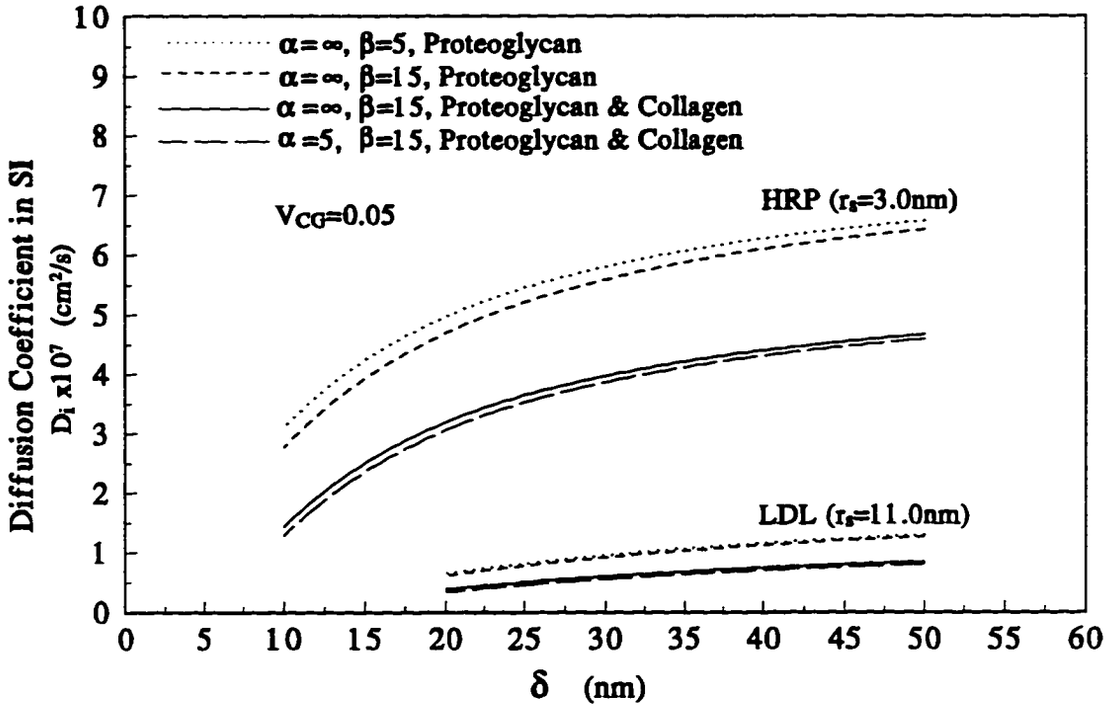

Fig.2.4 Diffusion coefficient D_i as a function of the fiber spacing δ for $\alpha=\infty$ and $\beta=5$, 15, for proteoglycans with and without collagen. The solute radius r_s is 3.0 and 11 nm, which is representative of HRP and LDL, respectively.

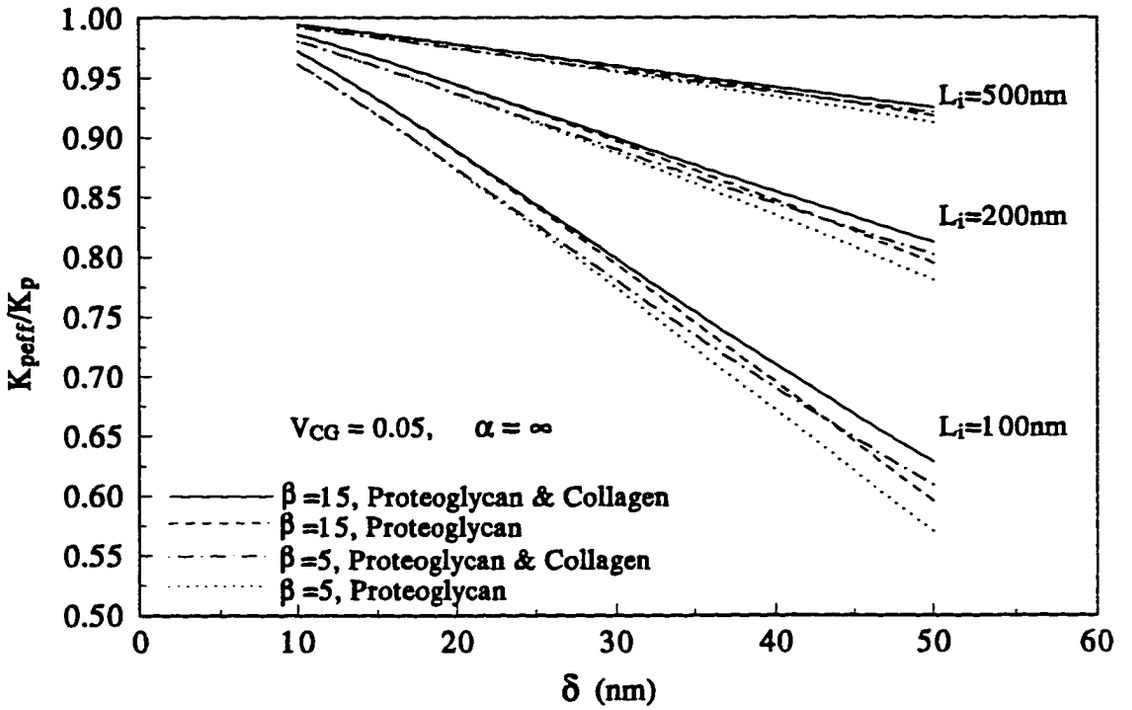

Fig.2.5 The ratio (Eq. (2.15)) of the effective permeability to the Darcy permeability (K_{peff}/K_p) as a function of the fiber spacing δ for α=∞ and β=5, 15, for proteoglycan with and without collagen. The intima thickness L_i=100, 200nm and 500nm.

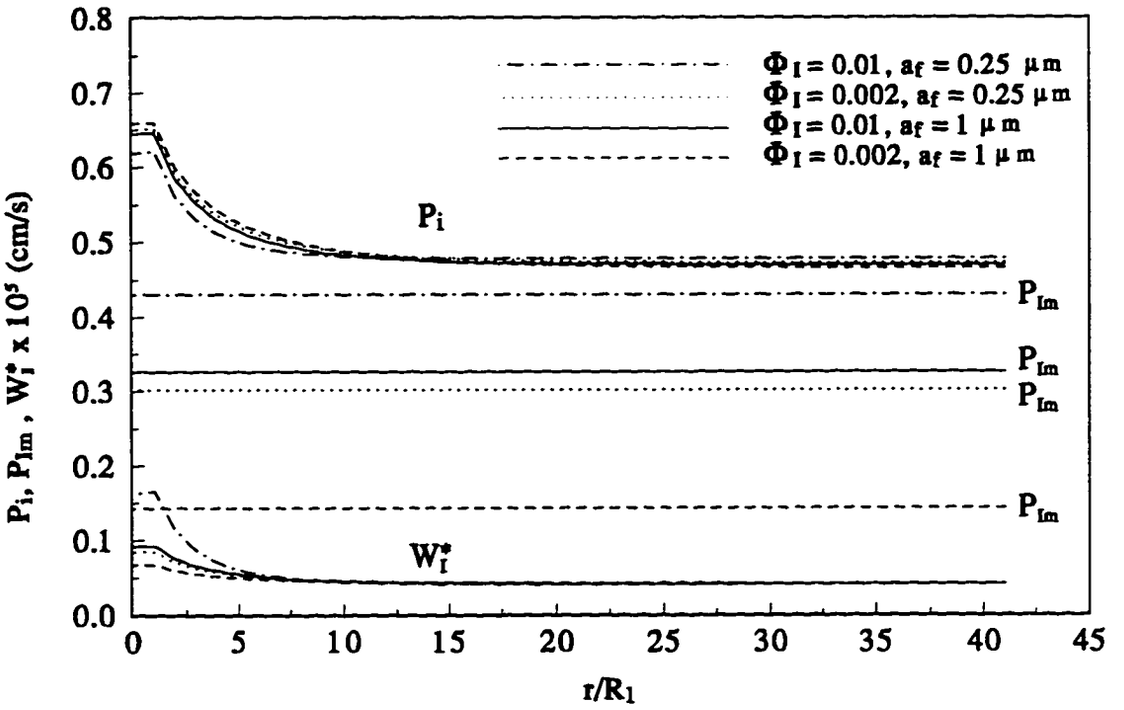

Fig.2.6Pressure distributions in the intima (P_i) and at the IEL-media interface (P_{Im}). and the normal velocity distributions across the IEL (W_I^*). ϕ_I is the fractional area of fenestra in the IEL. L_i=200nm. P_{iave}^*/P_L^* and the Peclet number of the media were fixed at 0.47 and 4.4. respectively. for all curves.

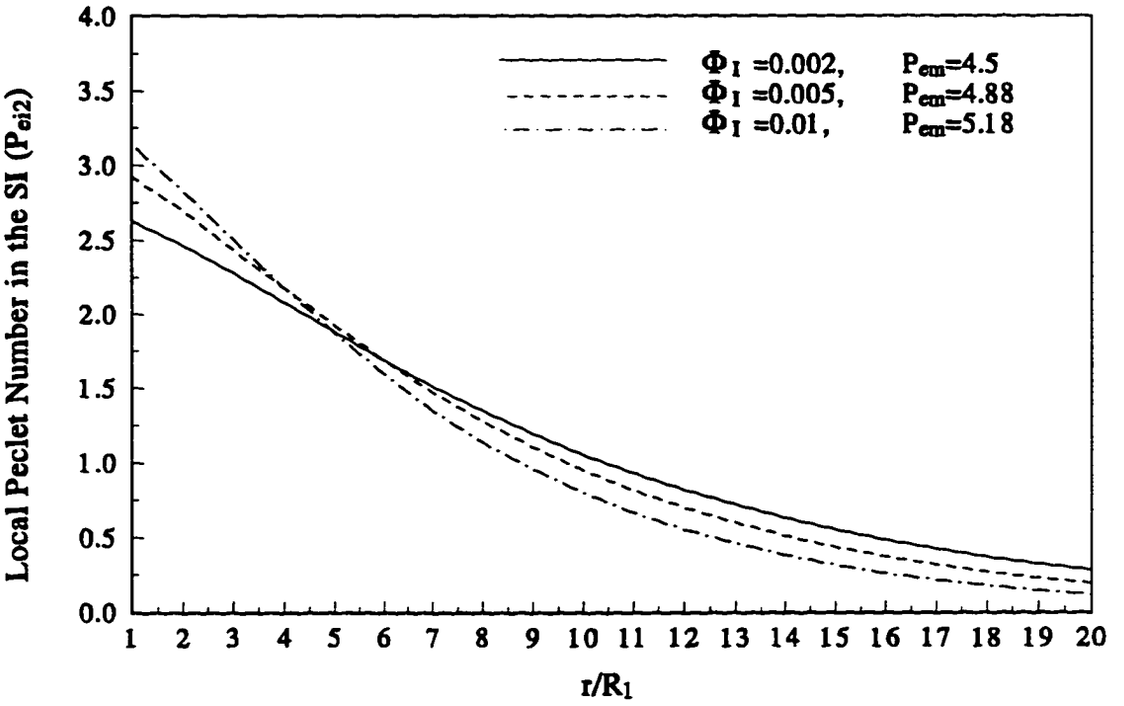

Fig.2.7 The local Peclet number distribution in the lateral direction in the intima (P_{ei2}). ϕ_I is the fractional area of fenestrae in the IEL. The distance between the fenestrae is $2\xi_I$=20μm. Lpm=2.0x10^{-11} cm^2-s/g, K_p=1.0x10^{-12}cm^2 and D_i=4.12x10^{-7}cm^2/s (for HRP). L_i=0.2μm.

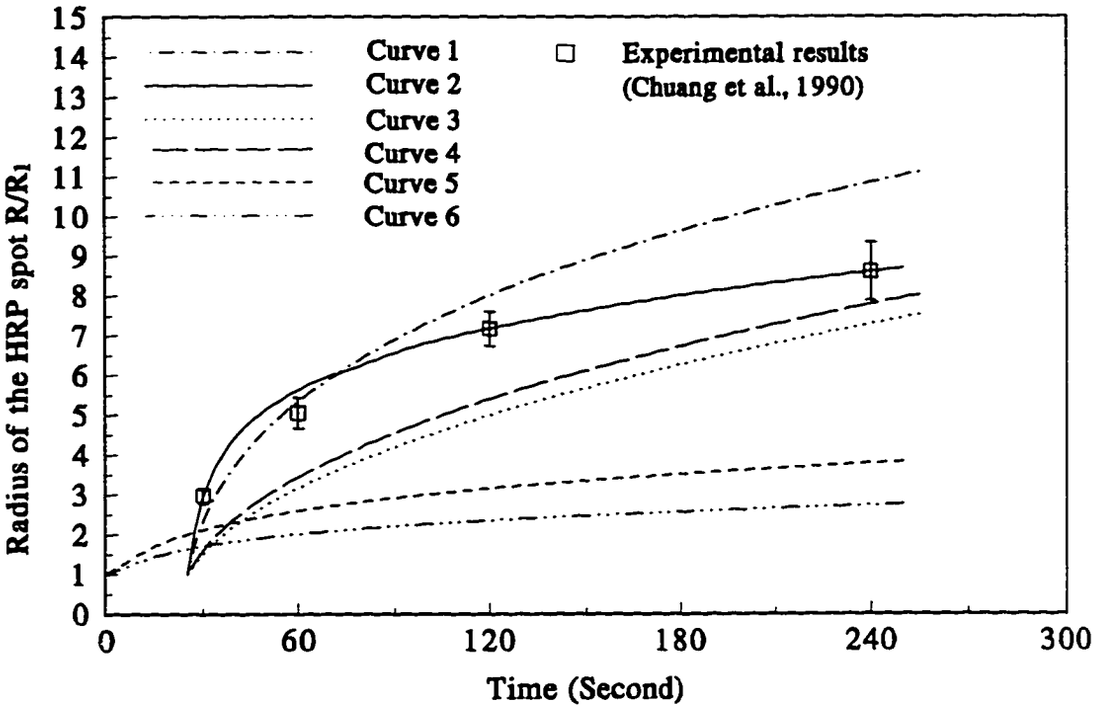

Fig.2.8 Early time growth of the leakage spots. Comparison of the theoretical prediction for the advancing edge of the convective front or convective-diffusive (curve 2) front and experimental results for growth in spot size. Curves 1.2: ϕ_f=0.002 and L_i=200nm. Curve 3: ϕ_f=0.002 and L_i=1μm. Curve 4: ϕ_f=0.01 and L_i=1μm. L_{pm}^*=3.0x 10^{-11} cm^2-s/g, δ=30nm, α=10, β=5, and t_0=25 seconds for curves 1-4. Curve 5: ϕ_f=0.001, L_{pm}=2.6x10^{-10} cm^2-s/g, K_p=K_{pm} (from Yuan *et al.*, 1991). Curve 6: ϕ_f=0.005, L_{pm}=0.9x10^{-10} cm^2-s/g, K_p=K_{pm} (from Yuan *et al.*, 1991). P_{em}=4.46, P_{iave}^*/P_L^*=0.47 for curves 1-3.

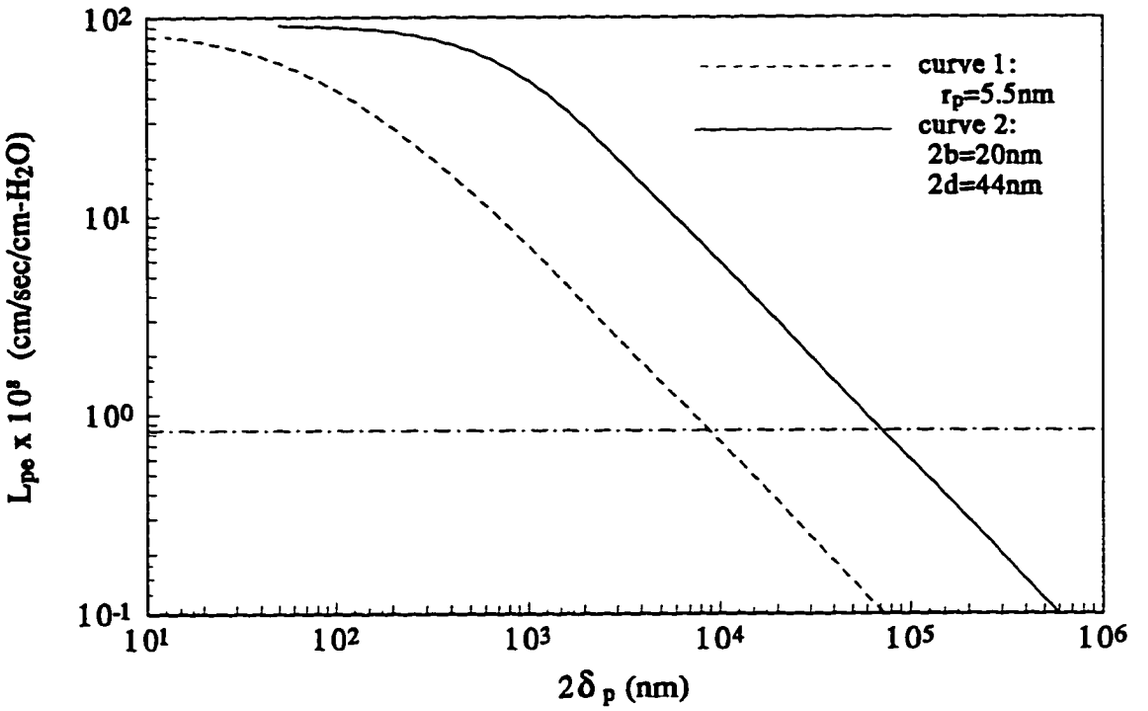

Fig.2.9 Solution for the hydraulic conductivity for normal endothelial clefts with pores in the junctional strand whose cross sectional shape is either circular with a 5.5nm radius (curve 1) or rectangular with height, 2b = 20 nm and length, 2d = 44nm (curve 2). The horizontal line is the predicted value of L_{pe} when P_{em}=4.46 and P_{iave}^{*}/P_L^{*}=0.47.

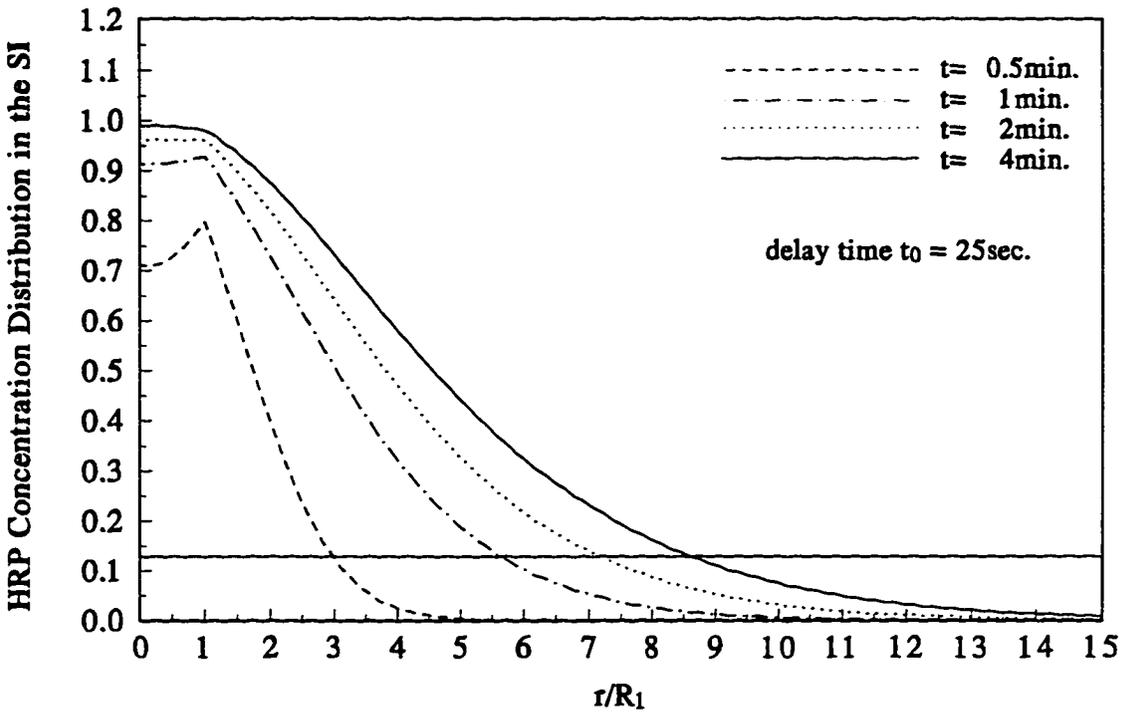

Fig.2.10 Time-dependent HRP concentration distributions in the intima for ϕ_l=0.002, ξ_l=20μm, K_p=1.08x10^{-12}cm^2 and D_i=4.12x10^{-7}cm^2/s (δ=30nm, α=10 and β=5). D_{zm}= 8.4x10^{-9}cm^2/s, K_{pf}=K_p, D_{zf}=D_i, L_i=200nm and t_0=25 seconds. P_{em}=4.46 and P_{iave}^*/P_L^*=0.47. γ_i=γ_l=γ_j=1 and γ_m=0.08. f_i=f_l=f_j=1 and f_m=0.3. K_{pf} and D_{zf} are the permeability and diffusivity in the fenestra, respectively.

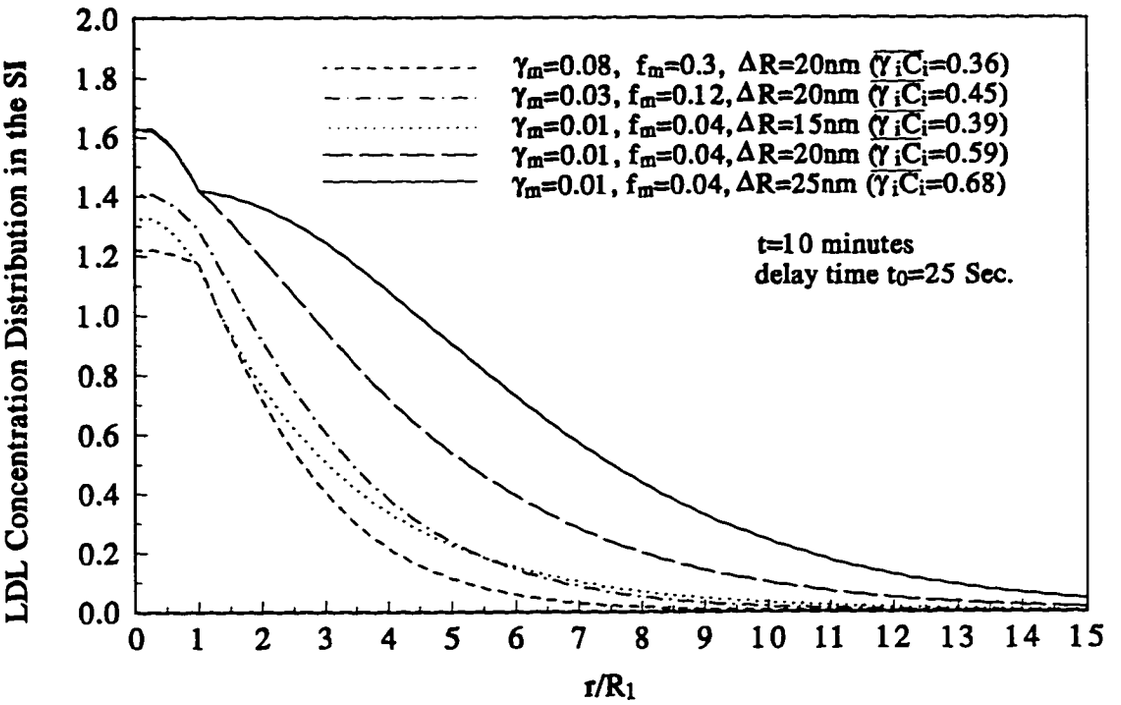

Fig.2.11 LDL concentration distributions in the intima at t=10 minutes for ϕ_l=0.005. ξ_l=15μm, K_p=1.08x10^{-12}cm^2 and D_i=6.02x10^{-8}cm^2/s (δ=30nm. α=10 and β=5). D_{zm}= 5.4x10^{-10}cm^2/s. L_{pm}^*=L_{pl}^*=8x10^{-11} cm^2/s. and W_m^*=2.8x10^{-6}cm/s. K_{pf}=K_p. D_{zf}=D_i. L_i=1μm and t_0=25 seconds. γ_i=γ_l=0.5 and γ_j=1. f_i=f_l=0.75 and f_j=1. K_{pf} and D_{zf} are the permeability and diffusivity in the fenestra, respectively.

Chapter 3

A Fiber Matrix Model for the Filtration through Fenestral Pores in a Compressible Arterial Intima

3.1 Introduction

The transport and accumulation of LDL in the arterial intima and their subsequent oxidation now appear to be critical processes in the formation of the early foam cell lesion (Carew, 1987; Steinberg, 1989; Weinbaum and Chien, 1993). The models in Huang *et al.* (1994) and Yuan *et al.* (1991) show that this transport is convection dominated and that the filtration flow in the intima determines the size of the cellular level macromolecular leakage spots observed in Chuang *et al.* (1990) and Truskey *et al.* (1992). Yuan *et al.* (1991) hypothesize and Yin *et al.* (1996) develop a theory that interprets experiments as supporting the notion that the latter sites are associated with the formation of subendothelial liposomes, the triggering event for the entry of blood borne monocytes into the intima (Simionescu *et al.*, 1986). This chapter develops a quantitative model for assessing how the transmural pressure affects the filtration properties of the intima.

Because the normal intima is very thin compared to the media, it is difficult to measure transport parameters such as Darcy permeability or hydraulic conductivity

separately for each region. In Chapter 2, we developed a model for the growth of macromolecular leakage spots in the arterial intima, in which we model and calculate, in an *ab initio* manner, the intimal transport parameters based on Frank and Fogelman's (1989) ultrastructural observations of the extracellular subendothelial proteoglycan matrix that their rapid freeze etching technique preserves. The model predicts that the order of magnitude of K_p, $10^{-12}cm^2$ in the intima, is a hundred fold greater than the value 10^{-14} cm^2 that (Baldwin *et al.*, 1992, 1993; Tedgui and Lever, 1984; Vargas *et al.*, 1979) measure for the media. Therefore, the intima is much more permeable than the media. The excellent agreement (Chapter 2; Huang *et al.*, 1994) between the predicted early time growth of the subendothelial HRP leakage spots and the experimental measurements in the rat aorta (Chuang *et al.*, 1990), and the consistency of the predicted and experimental subendothelial LDL spot size and average LDL concentration in these spots at 10 minutes in the rabbit aorta (Truskey *et al.*, 1992) provide strong evidence in support for this predicted value of K_p.

In Chapter 2, we treated the intimal region, considered over length scales large compared with a single endothelial cell, as a non-deformable layer with a uniform background pressure, except for the local region near a rare (a few in 10,000) endothelial cell with a leaky cleft. This model characterizes the IEL by a hydraulic conductivity L_{pI} which derives from a local model of the flow, driven by a *uniform* intimal pressure, through a single fenestra which spreads into the media. However, if the intima compresses under load, the spacing decrease of the intimal proteoglycan matrix can lead to a significant decrease in the intimal Darcy permeability K_p. In addition, the

narrowing of the intima can radically change the character of the fenestral flow to a blocked converging flow that is driven by a significant intimal pressure gradient.

In this chapter, we advance a new hypothesis to explain the changes in hydraulic conductivity of an intact artery wall with increasing transmural pressure that Tedgui and Lever (1984) and Baldwin *et al.* (1992, 1993) have observed experimentally. To quantitatively assess the feasibility of this mechanism, a local two-dimensional model is proposed to study the filtration flow in the vicinity of the fenestral pores in a compressible intima and a related expression is derived for the hydraulic conductivity of the IEL. Using a heterogenous fiber matrix theory, which includes proteoglycan and collagen components, we first predict the change in Darcy permeability with intimal thickness L_i. The model then calculates the local velocity profiles and pressure distributions in the intima and media. We estimate the relative change in the resistances of the IEL (with the intima), R_i, and of the media, R_m, as a function of intimal thickness and also predict how transmural pressures alter the growth of an intimal HRP leakage spot, which can be used to design a new experiment to test our new hypothesis.

The basic model in this chapter neglects the non-uniform deformation of the endothelium due to the pressure variation in the intima in order to avoid a much more complicated, non-linear elastohytrodynamic interaction problem. Our primary objectives in this study are to test the feasibility of the basic hypothesis, to provide a rough estimate of the degree of intimal compaction that is necessary to satisfy the measured filtration data, and to identify sensible simplifying assumptions for use in a future non-linear model, if necessary once the basic feasibility is demonstrated.

3.2 A New Intimal Compaction Hypothesis

If the thin intima between the deformable endothelium and the internal elastic lamina (IEL) is indeed compressible. the compaction due to the increase of pressure loading of the proteoglycan matrix in the arterial intima in the vicinity of the fenestral pores of the IEL can result in a large decrease in the local intrinsic Darcy permeability of the matrix and. therefore. can change the measured hydraulic conductivity of the artery wall significantly. That is. the changes in hydraulic conductivity of the artery wall with pressure might be due primarily to the compressibility of the intima. the deformation of the endothelium and partial blockage of the fenestral pores. rather than to significant changes in the structural properties of the media. This hypothesis also suggests that intimal compression has a limiting behavior in which the much stiffer collagen fibrils inhibit further compaction at high pressures after the proteoglycan matrix is maximally compressed.

3.3 Basic Filtrarion Model for Fenestral Pores

The ultrastructural observations in the artery wall. especially in the subendothelial intima (Frank and Fogelman. 1989: Lark *et al.*. 1988: Wight and Hascall. 1983). suggest a local. two-dimensional model for the filtration in the vicinity of fenestral pore in which the value of K_p is dependent on intimal compression. Let us construct (Fig. 3.1) a representative local periodic wall unit that is a circular cylinder of radius ξ_f^* (chosen to give the correct number of fenestrae per unit enface IEL area) with a fenestral pore at its center and a fluid source beneath the endothelium along the

wall unit's perimeter. The figure greatly exaggerates the vertical scale of the intima which can be up to two orders of magnitude smaller than typical distances along the intima. Except for a tiny region (of the order of the intimal thickness) near the cleft, the intimal flow is primarily radial towards the fenestrae. Very little water crosses the endothelial membrane directly, other than through these inter-endothelial clefts. As such, the wall unit's perimeter represents these clefts. We consider only normal clefts, since they vastly outnumber leaky endothelial clefts and account for almost all of the water flow across the endothelium. It is useful to note that the fenestral pores have a typical spacing in rabbit aorta of between 21 and 26 μm and the effective endothelial cell radius is about 15 μm. Thus the rough correspondence of the unit cell perimeter with the inter-endothelial clefts shown in Fig. 3.1 is not far off geometrically, although the placing of the fenestra beneath the center of the cell is an obvious idealization. Since in real arteries there can be more or less than one fenestral pore on average beneath each endothelial cell, we adjust the strength of the source at the perimeter of the periodic unit $r^*=\xi_1^*$ such that the source strength per unit length along the wall unit's perimeter matches the measured endothelial permeability. A more accurate model for the arbitrary placement of the fenestral pores relative to the location of endothelial clefts could be developed following the approach presented in Drumond and Dean (1994) for filtration through the glomerular capillary wall. In the glomerulus one encounters a similar geometry where the epithelial filtration slits are equivalent to the interendothelial clefts and the endothelial fenestra on the capillary side of the basement membrane are equivalent to the fenestral pores in the IEL. This added sophistication is not warranted

to test the quantitative feasibility of the present hypothesis.

After entering the intima along this perimeter, the water then flows towards the center of the wall unit and enters the media though the IEL's fenestral pores. The model treats the IEL as a impenetrable barrier of zero thickness except for its fenestral openings. The question is whether the non-fenestral area of the IEL is also permeable to water? The IEL, which is composed of the amino acids, is an elastin sheet with randomly distributed fenestrae. Perhaps the most remarkable feature of the chemical composition of the elastin is that the small nonpolar residues account for most of its protein. Very few polar residues are present (Walton and Blackwell, 1973). The data for the amino acid composition of elastin from chicken aortas (Seifter and Gallop, 1966) shows that more than 90% of the amino acids in the elastin are nonpolar residues. Since the nonpolar residues are hydrophobic, one can expect that the non-fenestral region of the IEL is most likely impermeable or almost impermeable to water due to high nonpolar residue content. The studies for the growth of the macromolecular leakage spots also support this idea. If the water can easily cross the non-fenestral regions of the IEL and enter the media, the lateral convection in the subendothelial intima will decrease rapidly with distance from the entry site and one would not expect the large macromolecular leakage spots observed in Chuang *et al.* (1990) and Truskey *et al.* (1992) and, especially, the rapid early time growth of HRP leakage spots measured by Chuang *et al.* (1990). Another fact is that the macromolecules, such as HRP, albumin and LDL can only enter the arterial media through the fenestral pores. This also suggests that, at least, the hydraulic resistance of the fenestral openings is much smaller

than that of the non-fenestral region in the IEL. Based on this evidence it is reasonable to assume that the IEL, except for the fenestral openings, is nearly impermeable to water.

As noted above, this initial model neglects the non-uniform deformation of the endothelium due to spatial differences in the transendothelial pressure. Our results will show that this pressure effect is particularly important in a region of 2 to 3 radii from the fenestral pores and, we believe, is responsible for the local indentations of the endothelial surface in Figs. 1.2 and 1.3.

Let j be a dummy index that can take on the values i (intima) and m (media). Let U_j^*, W_j^*, P_j^* and K_{pj} be the dimensional lateral velocity, normal velocity, pressure and Darcy's permeability, respectively, in region j, whose thickness is L_j^*. W_f^* is the fenestra velocity. For convenience, we introduce the following dimensionless (no *) variables and parameters

$$U_j = \frac{U_j^*}{(K_{p_j}/\mu)(P_L^*/r_f^*)}, \quad W_j = \frac{W_j^*}{(K_{p_j}/\mu)(P_L^*/L_j^*)}, \quad W_{f_j} = \frac{W_f^*}{(K_{p_j}/\mu)(P_L^*/L_j^*)}, \quad P_j = \frac{P_j^*}{P_L^*},$$

$$\xi_I = \frac{\zeta_I}{r_f^*}, \quad r = \frac{r^*}{r_f^*}, \quad z_j = \frac{z^*}{L_j^*}$$

As Chapter 2 details, the Darcy permeability of a fiber matrix of proteoglycans obeys the Carman-Kozeny equation (Curry, 1980, 1984, 1986)

$$K_{p(PG)} = \frac{R^{*2}\varepsilon^3}{4G(1-\varepsilon)^2} \tag{3.1}$$

for fiber radius R^* and void volume ε given in terms of geometric parameters α, β and

δ (see Fig. 3.2) by $R^* = \{[\alpha(\beta r_G^{*2} + r_{CP}^{*2}) + r_{CF}^{*2}]/(\alpha + 1)\}^{1/2}$ and $\varepsilon = 1-(R^*/\xi_f^*)^2[(\alpha+1)/\alpha]N$, where N is the total monomer number in the volume ($\pi\xi_f^{*2}$ x average monomer length). The Kozeny constant for uncharged, randomly oriented cylindrical fibers, is (Happel and Brenner, 1965)

$$G=\frac{2}{3}\frac{2\varepsilon^3}{(1-\varepsilon)[\ln(\frac{1}{1-\varepsilon})-\frac{1-(1-\varepsilon)^2}{1+(1-\varepsilon)^2}]}+\frac{1}{3}\frac{2\varepsilon^3}{(1-\varepsilon)[2\ln(\frac{1}{1-\varepsilon})-3+4(1-\varepsilon)-(1-\varepsilon)^2]} \quad (3.2)$$

Moreover, a simple approximate relation from (Tsay and Weinbaum, 1991) relates the Darcy permeability of the collagen matrix $K_{p(CG)}$ and $K_{p(PG)}$ in terms of the two fiber radii (R^* and r_{CG}^*) and the two average fiber spacings (δ and δ_{CG}), viz.,

$$\frac{K_{p(PG)}}{K_{p(CG)}}=(\frac{r_{CG}^*}{R^*})^{0.377}(\frac{\delta-2R^*}{\delta_{CG}-2r_{CG}^*})^{2.377} \quad (3.3)$$

Calculation of $K_{p(CG)}$ from (3.1) and (3.3) or simply from an equation similar to (3.1) give very similar results, as Chapter 2 showed. The overall K_p acts like capacitors in series, being simply the inverse of the sum of the inverses of $K_{p(PG)}$ and $K_{p(CG)}$.

The central difference between the present treatment of K_p and that in Chapter 2 is that here we introduce intimal compressibility by allowing the initial thickness L_{i0}^* to decrease to L_i^* under pressure loading. As such, the void volumes ε and $\varepsilon_{(CG)}$: =1-(volume fraction of collagen) for the proteoglycan and collagen calculations, respectively, are functions of L_i^*, viz.,

$$\varepsilon = 1 - \frac{L_{i_0}^{\cdot}}{L_i^{\cdot}}(1-\varepsilon_0) \ , \quad \varepsilon_{(CG)} = 1 - \frac{L_{i_0}^{\cdot}}{L_i^{\cdot}}(1-\varepsilon_{(CG)_0}) \tag{3.4}$$

where the subscript zero indicates the value defined as ε above (3.2) at zero transmural pressure. Using $\varepsilon_{(CG)}$ one can estimate the average collagen spacing $\delta_{(CG)}$ by assuming that these fibers form a parallel, triangle array.

3.3.1 Filtration in the Intima and Media

Darcy's law governs the relationship between the water velocity and the pressures in the intima i and media m:

$$\underline{V}_j = \underline{\nabla}_j P_j \quad (j=i,m) \tag{3.5}$$

where $\underline{V}_i=(U_i, W_i)$, $\underline{V}_m=(-U_m, W_m)$ and $\underline{\nabla}_j=(\partial/\partial r, \partial/\partial z_j)$ in cylindrical coordinates.

The continuity equation in each region is

$$h_j^2\left(\frac{\partial V_{j_1}}{\partial r} + \frac{V_{j_1}}{r}\right) + \frac{\partial V_{j_2}}{\partial z_j} = 0 \quad (j=i,m) \tag{3.6}$$

where $h_j = L_j^{\cdot}/r_f^{\cdot}$ are the ratios of the intimal and medial thicknesses to the radius of a fenestral pore.

The axisymmetry of the flow at r=0 and the periodicity of the flow in the media at $r=\xi_f$ require

$$\frac{\partial P_j}{\partial r} = 0 \ \ at \ \ r=0 \ \ (j=i,m); \quad \frac{\partial P_m}{\partial r} = 0 \ \ at \ \ r=\xi_f \ . \tag{3.7a,b}$$

Moreover, since we neglect the details of the flow through the endothelial clefts and replace the clefts by a ring source at $r=\xi_l$, whose flow is purely radial, $\partial P_i/\partial r(r=\xi_l)$ is non-zero. We also assume that the intimal pressure P_0 there is independent of z, i.e.,

$$P_i=P_0 \quad at \quad r=\xi_l \,. \tag{3.7c}$$

The intimal pressure P_0 and pressure gradient at $r=\xi_l$ are unknown and are determined as part of the solution of the problem. Except for the ring source at $r=\xi_l$, the endothelium is impermeable. In addition, we assume the adventitia is at the reference pressure. Thus

$$\frac{\partial P_i}{\partial z_i}=0 \quad at \quad z_i=1,\ r<\xi_l; \quad P_m=0 \quad at \quad z_m=-1. \tag{3.8a,b}$$

Since the water is assumed to enter the media only through the fenestral pores, the pressures and velocities must match there. This requires

$$\frac{\partial P_i}{\partial z_i}=0, \quad \frac{\partial P_m}{\partial z_m}=0 \quad for \quad 1\le r\le \xi_l \quad at \quad z_i=0 \tag{3.9a}$$

$$\frac{\partial P_i}{\partial z_i}=W_{f_i}(r) \quad for \quad 0\le r\le 1 \quad at \quad z_i=0 \tag{3.9b}$$

$$\begin{cases} P_m=P_i \\ \dfrac{\partial P_m}{\partial z_m}=W_{f_m}=\dfrac{L_m K_{p_i}}{L_i K_{p_m}} W_{f_i} \end{cases} \quad for \quad 0\le r\le 1 \quad at \quad z_m=0, \tag{3.9c,d}$$

where $W_{fi}(r)$, the normal velocity profile at the pore opening, is unknown. We choose to write the solutions below in terms of L_{pm}: $=K_{pm}/(\mu L_m^*)$ rather than K_{pm}, where L_{pm} is the hydraulic conductivity of the media. Finally, the average intimal pressure

$\overline{P_i}=(2/\xi_1^2)\int_0^1 P_i(r)rdr$ must be such that the overall flow across the artery wall matches the flow across the endothelium.

Thus.

$$L_{p_e}(1-\overline{P_i})P_L^* = \frac{2}{\xi_1^2}\int_0^1 W_f^*(r)rdr \qquad (3.10)$$

where L_{pe} is the (known) hydraulic conductivity of the endothelium. The integral constraint (3.10) closes the problem and allows determination of the unknown pressure P_0 at $r=\xi_1$.

3.3.2 Matching Conditions at the IEL Fenestra

The velocity profile W_f^* across the fenestral pore opening is the critical unknown that links the flow fields in the intima and media. An exact solution of the coupled boundary value problem for intima and media subject to the matching conditions $P_i^*=P_m^*$ and $\partial P_i^*/\partial z^*=\partial P_m^*/\partial z^*$ for $0\le r^*\le r_f^*$ at $z^*=0$ is difficult to obtain because of the mixed boundary conditions (3.9) on the pressure and its gradient. We shall simplify the boundary value problem defined by (3.5)-(3.10) by introducing three separate approximate velocity and pressure matching conditions instead of (3.9c) and (3.9d).

(a) W_f^* uniform, and the pressure matches only at the centerline $r^*=0$, $z^*=0$. Thus.

$$W_f^* = constant, \qquad P_i^* = P_m^* \quad at \quad r^*=0, \quad z^*=0 \qquad (3.11a)$$

(b) W_f^* uniform, and only the <u>average</u> pressure in the region $0\le r^*\le r_f^*$ matches at $z^*=0$. Thus.

$$W_f^* = constant\ , \quad \overline{P_i^*} = \overline{P_m^*} \quad at \quad 0 \le r^* \le r_f^*, \quad z^* = 0 \tag{3.11b}$$

where

$$\overline{P_j^*} = \frac{2}{r_f^{*2}} \int_0^{r_f^*} r^* P_j^*(r^*) dr^* \quad (j = i,\ m).$$

(c) $W_f^*(r)$ fits a cubic polynomial that satisfies $\partial W_f^*/\partial r^* = 0$ at $r^* = 0$. and the pressure is continuous at the locations: $r^* = 0$. $0.5 r_f^*$ and $0.9 r_f^*$ for $z^* = 0$. Thus.

$$W_f^* = (a_0 + c_0 r^2 + d_0 r^3) P_0^*\ , \quad P_i^* = P_m^* \quad at \quad r = 0,\ 0.5,\ 0.9, \quad z^* = 0 \tag{3.11c}$$

where a_0. c_0 and d_0 are undetermined constants to be determined by applying the matching condition (3.11c). P_0^* is the intimal pressure at $r^* = \xi_1^*$.

By comparing the detailed solutions for the two simpler approximations (3.11a) and (3.11b) with the more accurate matching condition (3.11c). we can evaluate how critical the local matching conditions are in determining the global resistance of the IEL. In any case. though. the solutions for the detailed pressure and velocity profiles will only be accurate far from the fenestral pore. since even the three-point matching in (3.11c) does not provide an accurate velocity profile in the pore. That is. since this formulation requires w_f^* to be cubic in r. which is only an approximation to the true shape. it is impossible to match P_i^* and P_m^* everywhere in the pore.

3.4 Solution of the Boundary Value Problem

The general solution of the filtration equations and boundary conditions except for (3.9) and (3.11a.b.c). is

$$P_i = P_0 + P_0 \sum_{n=1}^{\infty} B_n J_0(\lambda_n r) \frac{\cosh[\lambda_n h_i (z_i - 1)]}{\cosh(\lambda_n h_i)} \tag{3.12}$$

$$U_i = -P_0 \sum_{n=1}^{\infty} B_n \lambda_n J_1(\lambda_n r) \frac{\cosh[\lambda_n h_i (z_i - 1)]}{\cosh(\lambda_n h_i)} \tag{3.13}$$

$$W_i = P_0 \sum_{n=1}^{\infty} B_n \lambda_n h_i J_0(\lambda_n r) \frac{\sinh[\lambda_n h_i (z_i - 1)]}{\cosh(\lambda_n h_i)} \tag{3.14}$$

$$P_m = A_1 (z_m + 1) P_0 + P_0 \sum_{n=2}^{\infty} A_n J_0(\mu_n r) \frac{\sinh[\mu_n h_m (z_m + 1)]}{\sinh(\mu_n h_m)} \tag{3.15}$$

$$U_m = P_0 \sum_{n=2}^{\infty} A_n \mu_n J_1(\mu_n r) \frac{\sinh[\mu_n h_m (z_m + 1)]}{\sinh(\mu_n h_m)} \tag{3.16}$$

$$W_m = A_1 P_0 + P_0 \sum_{n=2}^{\infty} A_n \mu_n h_m J_0(\mu_n r) \frac{\cosh[\mu_n h_m (z_m + 1)]}{\sinh(\mu_n h_m)} \tag{3.17}$$

where J_0 and J_1 are the zero and the first-order Bessel functions, respectively. λ_n and μ_n are the roots of the eigenvalue equations $J_0(\lambda_n \xi_1)=0$ (n=1, 2, ... ∞) and $J_1(\mu_n \xi_1)=0$ (n=2, 3, ... ∞), respectively. $P_0=P_i(r=\xi_1)$, the intimal pressure at the edge of the wall unit, is given by

$$P_0 = \frac{L_{p_e}}{A_1 L_{p_m} + L_{p_e}\left[1 + \frac{2}{\xi_1^2} \sum_{n=1}^{\infty} B_n \frac{1}{\lambda_n} J_1(\lambda_n \xi_1)\right]} \tag{3.18}$$

The unknown coefficients A_n and B_n in the general solution (3.12) to (3.17) depend on which of the matching conditions (3.11a,b,c) equations (3.12) — (3.17) must satisfy. If (3.11a) or (3.11b) applies, then A_n and B_n depend only on the pressure at the

centerline or on the average pressure across the fenestral pore, respectively. If (3.11c) applies, then A_n and B_n depend on the three unknown constants a_0, c_0 and d_0 that appear in the polynomial for the velocity profile. The Appendix B lists the solutions for the coefficients in all three cases.

3.5 Parameter Values

3.5.1 Geometric Parameters

Based on the data in Potter and Roach (1983) we chose the average radius r_f^* of the fenestral pores as 0.8 μm and the radius of wall unit ξ_f^* as 12 μm, which corresponds average fenestral density of 2210/mm^2. The radii of the proteoglycan core proteins, r_{CP}^*, central filament, r_{CF}^*, glycosaminoglycans, r_G^*, and collagen, r_{CG}^*, in the intimal matrix are 2 nm, 2 nm, 0.6 nm and 20 nm, respectively (Chapter 2). The ratio α of the total GAG to total protein core lengths and the ratio β of the total protein core to central filament lengths in the intima are 10 and 5, respectively (Chapter 2). From Frank and Fogelman (1989) one can estimate $\delta \sim 30 - 40$ nm. We use δ=40 nm for the relaxed intima. The thickness L_{i0}^* of the intima at zero transmural pressure is assumed to be 500 nm.

Table 3.1 gives the other major parameters involved only in the calculations for the time-dependent growth of the HRP spot size (Fig. 3.10) using the convective-diffusive equations in Yuan *et al.* (1991) and Huang *et al.* (1994).

Table 3.1 Some parameters used in the calculations for the HRP spot size

ϕ	0.0005	[21]	γ_m (albumin)	0.08	[31]
R_l (μm)	15	[32,36]	D_{zm} (cm^2/s) (HRP)	8.4×10^{-9}	[15]
ΔR (nm)	20	[36]	D_{rm}/D_{zm}	3	[39]

where ϕ is the cell turnover parameter defined by the fractional area of the leaky cell: R_l is the effective radius of a leaky cell: ΔR is the width of the leaky cleft: γ_m is the HRP porosity of the media (using the value for albumin): and D_{zm} and D_{rm} are the normal and lateral diffusion coefficients in the media, respectively.

3.5.2 Hydraulic Conductivities

As described in Chapter 1, it is useful to think in terms of hydraulic conductivities which are the constants of proportionality relating the pressure difference driving force with the fluid velocity response. The L_p's in this problem are those of the media, IEL, endothelium, media+IEL and media+IEL+endothelium. They are, respectively, L_{pm}, L_{pl}, L_{pe}, L_{pm-l}, L_{pt}.

From Table 1.1, the average value of L_{pm-l} is 5.32×10^{-8} cm/s/mmHg for Tedgui and lever's (1984) experiments or 10.1×10^{-8} cm/s/mmHg for Baldwin and Wilson's (1993). Since the equations defining the L_ps are linear, the combined conductivity relates to the constituent conductivities via

$$\frac{1}{L_{p_{l-m}}} = \frac{1}{L_{p_m}} + \frac{1}{L_{p_l}} \quad \textit{and} \quad \frac{1}{L_{p_t}} = \frac{1}{L_{p_{l-m}}} + \frac{1}{L_{p_e}}. \qquad \textbf{(3.19a,b)}$$

Although (3.19a) relates L_{pm} and L_{pl}, L_{pm} is also part of the solutions (equations

(3.12) to (3.18)).That is. since at steady state. the water flow across each arterial layer must the same. one can average the solutions (3.12) and (3.15) for the pressure fields and (3.17) for the velocity and require:

$$\overline{W^*} = L_{p_f}(\overline{P_i^*} - \overline{P_m^*})_{z=0} = L_{p_m}\overline{P_m^*}|_{z=0} \qquad \textbf{(3.20a,b)}$$

Inserting (3.12) and (3.15) and solving. one finds

$$\frac{L_{p_m}}{L_{p_f}} = \frac{R_f}{R_m} = \frac{1}{A_1}\left[1 + \frac{2}{\xi_f^2}\sum_{n=1}^{\infty} B_n \frac{1}{\lambda_n} J_1(\lambda_n \xi_f)\right] - 1 \qquad \textbf{(3.21a,b)}$$

The resistance R_j: = $1/L_{pj}$: j=i. m. Equations (B.9) and (B.10) in the Appendix B give the expressions for A_1 and B_n.

As pressure compacts the intima. the character of the fenestral flow changes and this impacts the calculated value of L_{pf}. On the other hand. our model presumes that L_{pm} is independent of transmural pressure. Thus. it is important to evaluate L_{pm} at a fixed intimal compaction. say none ($L_i^* = L_{i0}^*$). by comparing the calculated L_{pf-m} with its measured value in de-endothelialized artery. and maintaining this value of L_{pm} for all intimal compressions. Thus. in order to find L_{pm}. one guesses a value for L_{pm}. calculates L_{pf} via (3.21) at $L_i^* = L_{i0}^*$ and checks if their inverses add up to the experimental value. If not. one adjusts L_{pm} accordingly and repeats. The converged results are L_{pm}=11.0 x 10^{-8} cm/s/mmHg for Tedgui and Lever and 20.9 x 10^{-8} cm/s/mmHg for Baldwin and Wilson. The Darcy permeability K_{pm} of the media is $K_{pm} = L_{pm}\mu L_m^*$. where μ=0.0072 g/cm/s is the viscosity of the water (Holman. 1986) at 35°C and L_m^*=125 μm is the thickness of the media (Baldwin *et al.*. 1992; Tedgui and Lever. 1984). For all other

values of L_i^* we retain the same value of L_{pm} and calculate $L_{pl}(L_i^*)$ via (3.21).

Similarly, L_{pe} should be independent of pressure for a given artery preparation. One can fix a rough estimate of its value by using the least stressed/compressed intima configuration for which L_{pt} data are available in table 1.1 (70 mmHg (Tedgui and Lever) or 50 mmHg (Baldwin and Wilson)) in equation (3.19b). This equation also needs an appropriate value for L_{pl-m}. As we shall see below L_{pl-m} depends on the extent of intimal compaction when this compaction leads to a non-uniform intimal pressure. Such a case obtains only when the intima is compressed to significantly less than 40% of its unstressed value (cf., Fig. 3.4 below). For less compaction, which we presume is the case for the lowest pressures in table 1.1 (this is consistent with Fig.3.8 below), the intimal pressure remains uniform. So L_{pl-m} should be insensitive to decompression or, in fact, to the presence of the endothelium. Thus for L_{pl-m} in the estimate of L_{pe} we simply use the average L_{pl-m} for each of Tables 1.1a and 1.1b. We then allow L_{pe}, which should actually derive from uncompressed intima data which are not available, to vary by a few percent in order to fit the entire set of table 1.1 data as plotted in Fig. 3.9 below. The results for L_{pe} are 18.0 x 10^{-8} cm/s/mmHg for Tedgui and lever and 29.3 x 10^{-8} cm/s/mmHg for Baldwin and Wilson. Again, one retains these same values of L_{pe} for all lumen pressures.

With all of the L_p's known, it is possible, in a macroscopic way, to determine how $\overline{P_i^*}$ and $\overline{P_m^*}$ relate to P_L^* from the relationship between P_L^* and L_i^*. By the same argument as led to (3.20) one has

$$\overline{W^*}=L_{p_e}(P_L^*-\overline{P_i^*})=L_{p_{t-m}}\overline{P_i^*}=L_{p_t}P_L^* \qquad \textbf{(3.22a,b,c)}$$

or.

$$\overline{P_i^*}=\frac{L_{p_e}P_L^*(L_i^*)}{L_{p_{t-m}}(L_i^*)+L_{p_e}}=(1-\frac{L_{p_t}(L_i^*)}{L_{p_e}})P_L^*(L_i^*) \qquad \textbf{(3.23a,b)}$$

$$\textit{and}\quad \overline{P_m^*}=\frac{L_{p_{t-m}}(L_i^*)}{L_{p_m}}\overline{P_i^*}(L_i^*). \qquad \textbf{(3.23c)}$$

3.6 Results

3.6.1 Thickness Dependence of the Darcy Permeability

Fig. 3.3 shows the relationship between the intimal permeability K_p and the intimal thickness obtained from equations (3.1) and (3.3). It includes the effects of both proteoglycans and collagen fibers. The background value $K_p=2.2\times10^{-12}$ cm^2 for the undeformed matrix comes from the fiber matrix theory and the parameter values similar to those in Chapter 2. It assumes an average proteoglycan monomer spacing of 40 nm and a fractional collagen volume of 5% (Chapter 2; Huang *et al.*, 1994) for the reference permeability at zero transmural pressure. One observes in Fig. 3.3 that the Darcy permeability decreases rapidly with the decrease of intimal thickness. The value of K_p at $L_i^*=0.2L_{i0}^*$ is one order of magnitude lower than that at $L_i^*=L_{i0}^*$. This change in K_p significantly affects the local velocity profile and pressure distribution in the vicinity of the fenestral pores in the intima.

3.6.2 Pressure Drop across the IEL

Fig. 3.4 predicts the pressure distributions[1] above and below the IEL at L_i^*=50 nm for all three matching conditions and for the third condition (3.11c) at other intimal thicknesses. For a given L_i^* the major difference in the pressure distributions for the three different matching conditions, especially for (3.11b) and (3.11c), is in the fenestral pore region $r^*/r_f^* \leq 1$. Clearly, approximation (3.11c) is superior to (3.11a) or (3.11b) since this approximation most closely satisfies the continuity of pressure across the pore opening $r \leq 1$. However, if one is interested in only the average pressure drop or average change of the filtration resistance across the IEL, the result obtained by approximation (3.11b) is close to that given by (3.11c), since the area occupied by the fenestral pore is small compared to $\pi\xi_1^{*2}$. For all calculations presented below, we stick with (3.11c).

Fig. 3.4 shows that the pressure decreases from the edge ξ_1^* to the center of the wall unit on the intima side and that there is a qualitative change in behavior as well as in $P_i(\xi_1)$ as the thickness of the intima decreases in response to an increasing transmural pressure. For L_i^* = 50 nm, most of the pressure drop occurs in the intima in a region of several pore radii surrounding the fenestral opening, whereas for $L_i^* > 200$ nm, most of the pressure drop occurs in the media.

---

[1] Note that Fig. 3.4 plots the pressure, dedimensionalized by the lumen pressure P_L^* that corresponds to a given intimal compaction. At this point P_L^* is not known and one cannot yet determine the dimensional pressure in Fig. 3.4. Section 3.6.5 below develops a theory relating L_i^*/L_{i0}^* and P_L^* and combining Figs. 3.8 and 3.4 yields these dimensional profiles.

One anticipates that if the endothelium is deformable and the local deformation is proportional to the local transendothelial pressure difference, the large drop in intimal pressure as one approaches the fenestral pore would lead to a large, marked non-linear endothelial deformation: it would steepen near the edge of the pore and bottom out over the fenestral pore. The scanning electron micrograph in Fig. 1.2 reveals this qualitative behavior where at pressures above ~ 80 mmHg, small crater-like depressions appear in *en face* studies of the endothelial surface. These surface indentations, first observed in Lee and Chien (1979), had previously been unexplained. It is really interesting that simply following the prediction of our theoretical model, we have found endothelial indentations over the fenestral pores at a higher lumen pressure (100 mmHg) in our newly performed *in situ* experiment in the rat thoracic aorta (Fig. 1.3).

3.6.3 Pressure and Velocity Profiles in the Intima and the Media

Because (a) the size of the fenestral pore, $2r_f^*$, is much smaller than the spacing between two pores, $2\xi_f^*$, (b) the thickness, L_i^*, of the intima is much smaller than ξ_f^* and the thickness, L_m^*, of the media, and (c) Darcy flow cannot satisfy a boundary condition on the tangential component of the velocity at z=0, 1, the pressure distribution and velocity profiles in the intima should and do exhibit a nearly one-dimensional (radial only) behavior, except in the immediate vicinity of the fenestral pore. Fig. 3.5, despite some inaccuracy in the pore yielding an artifactual oscillation of P_m in Figure 3.4, shows this. So the velocity profile is one-dimensional for $r^* > 1.2\ r_f^*$ and almost so in the fenestral region as well. Thus a more complex elastohydrodynamic model for a

deformable endothelium may also assume one-dimensional intimal profiles. In the media, results not shown indicate that the small maxima in the pressure and velocity profiles near the fenestral pore disappear within a distance of $0.02L_m^*$ from the IEL lower surface: thus the flow there is also almost one dimensional, though here in z.

It should be pointed out that the polynomial velocity profiles (3.11c) across the fenestral opening for different L_i^* are qualitatively different from those obtained for Poiseuille flow in a circular tube or Sampson flow through a circular orifice at low R_e (Sampson, 1891). The maximum velocity occurs near the edge of the pore and not at its center. These profiles are similar to Zeng and Weinbaum's (1994) recent solutions for the Hele-Shaw potential flow profiles through periodic orifices in a planar barrier in a channel. This is not surprising because the filtration flow through the fenestral pores in the artery wall, like Hele-Shaw orifice flow, is a potential flow problem.

3.6.4 Relative Resistance of the Intima plus IEL and the Media

The experimental results in Tedgui and Lever (1984) and in Baldwin and Wilson (1993) for de-endothelialized rabbit aortas indicate that the hydraulic conductivity, and hence the filtration resistance of the media, do not vary significantly with transmural pressure. Such a result is consistent with our model since in the absence of the endothelium there is no intimal compression and no occlusion of the fenestral entrances. Therefore, the present calculation assumes $L_{pl\text{-}m}$ for a denuded aorta is pressure-independent.

Since the resistance of the media is pressure-invariant in our model, the increase

in total wall resistance is due solely to the compaction/compression of the intima (a decrease in K_p) and the obstruction of the fenestral openings via a decrease in L_i^*. This, in turn, affects the calculated pressure and L_{pl} via (3.21) and thus the total wall resistance. Fig. 3.7 shows the change in the resistance R_f of the IEL plus the intima, relative to that of the media, R_m, as a function of L_i^*/L_{i0}^* for L_{i0}=200 or 500 nm and r_f^*=0.8 or 2.0 μm. One observes that the ratio of R_f/R_m changes slowly from L_i^*/L_{i0}^* = 1 to 0.4. However, there is a steep increase in R_f/R_m for $L_i^*/L_{i0}^* < 0.25$. The resistance R_f has two components: the lateral resistance of the flow towards the pore edge r_f^* in the intimal matrix (upper branches in Fig. 3.4) and the resistance due to the spreading of the flow from the fenestral pores in the media (lower branches in Fig. 3.4). Comparing Fig. 3.6 with Fig. 3.4, one concludes that the spreading resistance of the flow after it has passed through the fenestral pores primarily determines R_f when the thickness of the intima $L_i^*/L_{i0}^* > 0.4$, whereas when $L_i^*/L_{i0}^* < 0.25$ the flow resistance of the intima becomes dominant. It is this latter resistance which leads to the rapid increase in R_f/R_m displayed in Fig. 3.6. This figure also shows the effects of the unstressed thickness L_{i0}^* of the intima and the radius r_f^* of the fenestral pore on the resistance ratio R_f/R_m. For $L_i^*/L_{i0}^* > 0.4$, no significant change occurs in R_f with L_{i0}^*. However, there is a large increase in R_f as the L_{i0}^* decreases from 500 nm to 200 nm for $L_i^*/L_{i0}^* < 0.25$ at fixed L_i^*/L_{i0}^*. The change in R_f with decreasing r_f^* at fixed fenestral spacing $2\xi_f^*$ = 24 μm is also significant. The values of R_f/R_m for r_f^* = 0.8 μm are approximately 2 ~ 2.5 times as large as for r_f^* = 2.0 μm (six times the fenestral area) for the same value of L_{i0}^*.

Fig. 3.7 compares the hydraulic conductivity of the IEL with the intima, L_{pI}, obtained by the present model with that estimated using the earlier model (Chapter 2: Yuan *et al.*, 1991). The results show that the previous L_{pI} in Chapter 2 is the limiting case of the present results in which there is no compression (nearly uniform intimal pressure, see Fig. 3.4) and the pressure across the fenestral hole is matched only at $r^*=0$.

3.6.5 Pressure-dependent Hydraulic Conductivity

Fig. 3.6 demonstrates that the ratio of the hydraulic resistance of the IEL plus the intima to that of the media increases very rapidly when higher transmural pressures thin the intima to less than about one-fifth of its initial value. When R_I increases rapidly, this value of L_i^*/L_{i0}^* is insensitive to the initial intimal thickness. However, one should expect little additional compaction once the lumen pressure exceeds a "critical pressure" P_{Lc}^* at which collagen fibers principally bear the normal load. The typical radius, ~ 20 nm, of a collagen fiber far exceeds the radius, ~ 2 nm, of the proteoglycans' protein core; thus the collagen is much stiffer than the proteoglycan component. One anticipates that the hydraulic conductivity of the intima plus the IEL will remain almost constant once the lumen pressure exceeds this "critical pressure". Since the fractional volume of collagen is < 0.05 in the unstressed state (Chapter 2: Huang *et al.*, 1994), our simple geometric model for the intimal collagen matrix predicts that the "critical thickness" L_{ic}^* is about 14 percent of its unstressed value at this "critical pressure" if compaction takes place only in the z direction and leaves the x, y directions unaffected. The fractional volume of collagen should therefore be

approximately 0.35 at this critical compaction.

To predict the changes in Tedgui and Lever (1984) and Baldwin and Wilson (1993) of the hydraulic conductivity with transmural pressure in the intact artery wall, we still need an equation for $L_i^*(P_L^*)$. Assume a simple Hookean relationship between the lumen pressure and the intimal thickness for $P_L^* \le P_{Lc}^*$

$$P_L^* - \overline{P_i^*} = k\left(1 - \frac{L_i^*}{L_{i_0}^*}\right), \tag{3.24}$$

with an intimal elastic coefficient k that is independent of the transmural pressure. Recall that (3.24) is a non-linear relationship $L_i^* = L_i^*(P_L^*, L_{i0}^*; k)$ since the average intimal pressure $\overline{P_i^*}$ is a function of L_i^*. From (3.23) and (3.21), P_i^* depends on whether $P_L^* < P_{Lc}^*$ or $P_L^* \ge P_{Lc}^*$, i.e.,

$$\overline{P_i^*} = \begin{cases} \dfrac{L_{p_e}}{\dfrac{L_{p_m}}{[R_i(L_i^*)/R_m]+1} + L_{p_e}} P_L^* & (P_L^* < P_{Lc}^*) \\ \dfrac{L_{p_e}}{L_{p_{t\text{-}m}}(L_{i_c}^*) + L_{p_e}} P_L^* & (P_L^* \ge P_{Lc}^*) \end{cases} \tag{3.25}$$

Therefore, (3.24) and (3.25) give an implicit expression for $L_i^*(P_L^*)/L_{i0}^*$ for $P_L^* < P_{Lc}^*$:

$$P_L^* = \left[1 + \frac{L_{p_e}}{L_{p_m}}\left(\frac{R_i(L_i^*/L_{i0}^*)}{R_m} + 1\right)\right] k\left(1 - \frac{L_i^*}{L_{i_0}^*}\right) \quad for \quad P_L^* < P_{L_c}^* \tag{3.26a}$$

$$\frac{L_i^*}{L_{i_0}^*} = \frac{L_{i_c}^*}{L_{i_0}^*} \quad for \quad P_L^* \geq P_{L_c}^* \tag{3.26b}$$

$L_{pt}(L_i^*)$ follows simply from (3.23b) and (3.25). L_{pt} with (3.26) give the $L_{pt}(P_L^*)$.

Fig. 3.8 is a plot of Eq. (3.26), showing the variation of intimal thickness with lumen pressure. This calculation sets the hydraulic conductivity L_{pm} of the media to 11.0 x 10^{-8} cm/s/mmHg, the hydraulic conductivity L_{pe} of the endothelium to 18.0 x 10^{-8} cm/s/mmHg, the elastic coefficient k of the intima to 22 $(mmHg)^{-1}$ and the "critical thickness" L_{ic} of the intima to 0.13. The value of k is obtained by scaling the model to Tedgui and Lever's (1984) measured data for an intact artery wall in the upper part of Fig. 3.9. As the lumen pressure increases from 0 to 50 mmHg the intimal thickness decreases almost linearly from $L_i^*/L_{i0}^*=1$ to about 0.5. A non-linear decrease of the intimal thickness then appears with further increase in lumen pressure until $P_L^*=P_{Lc}^* \sim$ 135 mmHg. Once the lumen pressure exceeds the "critical pressure" no further intimal compaction occurs.

Fig. 3.9 compares the theoretical predictions for L_p and the experimental measurements in Tedgui and Lever (1984) and Baldwin and Wilson (1993). It takes the "critical thicknesses" $L_{ic}^*/L_{i0}^* \approx 0.13$ and 0.16 for Tedgui and Lever (1984) and Baldwin and Wilson (1993), respectively. The agreement is good. The Discussion section explains why the experimental results in Tedgui and Lever (1984) and Baldwin and Wilson (1993) may differ.

3.6.6 Changes of HRP Spot Sizes with Time for Different Lumen Pressures

The impetus for developing the two-dimensional artery wall convective-diffusive models in Yuan *et al.* (1991) and Huang *et al.* (1994) was to explain the observed time-dependent growth of an HRP spot that derives from a cellular level leakage site. The leakage is assumed to occur along the perimeter of a single, rare endothelial cell allowing the transport of lumen macromolecules into the rat thoracic aorta artery wall. Although accomplishing this task quite well, the model in Chapter 2 (Huang *et al.*, 1994) assumes an incompressible intima with transport properties that are independent of lumen pressure. One anticipates that the growth of the HRP spots will be significantly reduced in an compressible intima due to (i) the reduction in the intimal L_p (reduced lateral convection) with increased lumen pressure, (ii) the decrease in the retardation coefficient and (iii) the lower diffusive permeability due to the intimal compaction. It is difficult to estimate these effects for the rat aorta, because there is no available experiment that has measured the variation of L_{pi} with P_L^* in the rat. However, one can use the experiments in Tedgui and Lever (1984) and Baldwin and Wilson (1993) and the theoretical predictions in Figs. 3.6, 3.7, 3.8 and 3.9 to predict the effect of P_L^* and intimal compaction on the growth of HRP leakage spots in the rabbit aorta.

We have combined the present model for the compaction of rabbit intima with our convective-diffusive transport model in Chapter 2 to predict the change of the time dependent HRP concentration profiles, and thus leakage spot sizes, with transmural pressure. Fig. 3.10 compares two cases at various pressures: (1) a compressible intima whose Darcy permeability, K_p, molecular diffusivity, available volumes for HRP, and

retardation coefficient in the intima are functions of lumen pressure: and (2) an incompressible intima whose permeability properties are independent of lumen pressure. Figs. 3.8 and 3.9 (Tedgui and Lever's data) give the relations between L_i^*/L_{i0}^* and P_L^* and L_p and P_L^*. respectively. To identify the edge of the spot we calculate the HRP concentration profile $C_i(r)$ for various times. Since one does not know a priori the threshold value of C_i for the HRP reaction product's visibility. we have chosen the visible edge of the spot at large times (4 minutes in the rat aorta experiment in Chuang *et al.*, 1990) to determine this value of C_i. Once this value is chosen. this same absolute cutoff must be used for all other times. As demonstrated in Fig. 8 of Huang *et al.* (1994) an excellent agreement for the growth of spot size with time results for a threshold C_i of 0.1. When the intima is incompressible. the long time asymptotic spot size appears to be independent of pressure; the higher pressure serves only to shorten the time needed to reach its asymptotic size. The reason for this is that since the spread of the tracer is convection-dominated and since the flow satisfies Darcy's law. i.e.. potential flow. the stream lines are pressure-independent: increasing the pressure simply increases the velocities along the stream lines without changing their shapes.

In contrast. with intimal compaction. the asymptotic size of the HRP spot at 4 minutes decreases by 17% when P_L^* increases from 50 to 70 mmHg and it decreases an additional 35% when P_L^* increases further to 100 mmHg. Moreover. the time needed for the spot to reach its asymptotic size decreases rapidly as the pressure increases. being about a minute at 100 mmHg rather than more than four minutes at 50 mmHg. The predicted spot sizes for the rabbit aorta with an incompressible intima are about 2/3

the values for the rat aorta predicted in Chapter 2. This difference is primarily due to the different distribution of the hydraulic resistance in the rat and rabbit artery walls. The hydraulic resistance of the endothelium, R_e, is probably similar for both the rat and rabbit. However, the arterial media of rabbit is significantly thicker. This leads to a larger value for the resistance R_{I-m} of the media plus IEL in the rabbit than in the rat. The pressure drop across the endothelium should, therefore, be significantly smaller for the rabbit than that for rat. The smaller transendothelial pressure drop will decrease the lateral convection in the intima. In the prediction for rat in Chapter 2 (Huang *et al.*, 1994), we assumed that the hydraulic resistance ratio R_e/R_{I-m} was about 1. In the present prediction for rabbit aorta, we chose R_e/R_{I-m}, after considering the effect of the intimal compaction on the total hydraulic conductivity, to be about 0.3.

3.7 Discussion

Based on the results in Figures 3.6 and 3.9, and the measurements of L_p in table 1.1, we anticipate that the endothelium, especially in the area over the fenestral pore, deforms substantially at lumen pressures in excess of 75-100 mmHg and that the local compaction of the intima in these areas may exceed 80% of the initial unloaded intimal thickness. This deformation should be accompanied by a non-linear steepening of the pressure gradient approaching the pore edge and large changes in the local hydraulic conductivity of the intima. These changes should also lead to a significant decrease in the effective entrance area of the fenestral pore if the pore opening is partially covered by the collapsed endothelium. To estimate this non-linear effect of endothelial

deformation on the total filtration resistance, one would need to construct an elastohydrodynamic model to relate the local endothelial deformation to the local transendothelial pressure difference.

These results stand in contrast to the assumption of a rigid intima in Chapter 2 and the theory for L_{pl} there that assumes a uniform intima pressure. In the present model, only when the intima is relaxed (~500nm) is the intimal pressure almost independent of r^* in Fig. 3.4. On the other hand, with severe compaction ($\leq$200nm) the intimal pressure profiles, far from being flat, have large gradients. This leads to substantial changes in L_{pl} from the earlier theory of Chapter 2, as in Fig. 3.8.

The origin of the differences between the experimental results in Lever and Sharifi (1987), Tedgui and Lever (1984) and in Baldwin and Wilson (1993) is still unclear. In the experiment performed by Baldwin and Wilson (1993) the hydraulic conductivity in the intact artery wall drops significantly from 50 mmHg to 75 mmHg lumen pressure. However, in the experiments of Tedgui and Lever (1984) and Lever and Sharifi (1987), the large decrease in hydraulic conductivity in the intact artery wall occurs when the transmural pressure increases from 70 to 100 mmHg. In either case, there seems to be little change in L_p for very low transmural pressures, a sharp decrease in L_p over a higher pressure range, and then a stabilization of L_p at pressures above 100 mmHg. This behavior is consistent with the theoretical predictions in Figs. 3.6 and 3.9. The sharp increase in R_l in Fig. 3.6 occurs abruptly and would be predicted by a linear elastic model for the intimal compaction of the proteoglycan fibers. The stiffening of the matrix for pressures > 100 mmHg is necessary to explain the constancy of L_p at

very high pressure. One major difference in the experimental protocols between Tedgui and Lever (1984) and Baldwin and Wilson (1993) is that Baldwin and Wilson (1993) introduced a muscle relaxant into the arteries before commencing measurement. This treatment might result in a much softer tissue. One observes in Baldwin *et al.* (1992) that the IEL is nearly flat at 50 mmHg after administration of a muscle relaxant, and this might explain the difference in behavior at the lower lumen pressures in Tedgui and Lever (1984) and Baldwin and Wilson (1993). In contrast, the scanning electron micrograph in Lee and Chien (1979) shows that, in the absence of muscle relaxant, the IEL surface is highly undulated at transmural pressures of 50 mmHg or less. The presence of the muscle relaxant leads to a different stress distribution in the inner layers of the artery wall at the lower lumen pressures. Since the combined stress is a sum of the local hoop tension and the pressure distribution in the wall, it is clear that the latter would change if the state of the IEL were altered from compression to tension following treatment of the aorta with a muscle relaxant.

One aspect of Lever and Sharifi's (1987) results, the effect of differing concentrations of albumin, is beyond the scope of the present model. They find that increasing the BSA concentration from 2 to 7 g/ml systematically decreases L_p at all pressures between 70 and 180 mmHg, by about the same, large amount and constant lower L_ps are obtained at higher pressures. These results suggest concentration polarization rather than the binding of albumin to surface glycocalyx since both concentrations of BSA far exceed the levels of BSA that were required to saturate the albumin binding sites in the surface glycocalyx of capillary endothelium, Michel (1988).

Thus, if binding were the dominant mechanism for the decrease in L_p one would expect the same result for both BSA concentrations. The fact that L_p still appears to asymptote to constant (lower) values of L_p at the higher pressures for both concentrations of BSA is consistent with our hypothesis that the collagen component of intimal matrix resists intimal compaction at high transmural pressures. Once the intimal proteoglycans have been compressed there should be no further change in the flow pattern in the intact artery if the porosity of the media does not change. As a result, the concentration polarization should also approach a limiting value, as observed in Lever and Sharifi (1987).

In contrast to the intact artery, the present model is not adequate to conclusively explain the behavior of the denuded vessels in Tables 1.1a, b. Our model simply suggests that in the absence of an endothelium and an intima to compress, the wall's conductance should be pressure independent, as observed. However, in the absence of an endothelial barrier, medial hydration can tend to swell the wall. As shown in Tedgui and Lever (1987), whereas there are only very minor variations in the ^{14}C sucrose space (porosity) in an intact vessel, whether it is relaxed or at 70 or 180 mm Hg, there can be as large as a 17% increase in this available space in deendothelialized artery at the high convective velocities corresponding to 180 mm Hg (There is no significant increase in porosity between relaxed and 70 mm Hg pressurized arteries). This porosity change is the net observed effect, and includes hydration as well as any tendency towards medial compaction, the former clearly dominating at 180 mm Hg. Equations (3.1) and (3.2) predict that such large changes in porosity should lead to an 80 percent

increase in the Darcy permeability. It is thus an unexplained puzzle, irrespective of whether one accepts the notion of medial compaction as the operative mechanism in the control of L_ps, as to why the L_ps at 70 and 180 mm Hg for the denuded vessel in Table 1.1a are the same. The data in Tedgui and Lever, 1987 show a uniform distribution of the ^{14}C sucrose space at all pressures, thereby negating hydration non-uniformity as an explanation.

Curmi *et al.* (1990) report another set of relevant data for which some have invoked a medial compaction hypothesis. These investigators, using serial sectioning, measure the albumin and LDL concentration profiles across the artery wall after two hour incubations at 70 and 160 mmHg. Interestingly, they find that the concentration of albumin is an order of magnitude higher at the higher pressure throughout the wall, while that of the LDL at 160 mmHg is 50 times its value at the lower pressure near the lumen side and relaxes to just a few times its low pressure value about half way through the wall. Moreover, when the 30 minute incubation with albumin or LDL is followed by a 30 minute tracer-free washout period, both performed at 160 mmHg, nearly all the albumin clears from the wall. In contrast, the LDL concentration decreases by 40% in the section closest to the lumen and is otherwise completely retained in the wall.

Since convective transport scales linearly with pressure, the magnitude of the LDL increase at 160 mmHg is far larger than convection could explain. Moreover, the LDL profile shape is consistent neither with steady convection nor with steady diffusion. If medial compaction were the cause of the LDL trapping, then LDL would

have just as difficult a time entering the media as leaving it, and one would not observe the high LDL concentrations in the wall at all. Fry's (1986) experiments with denuded minipig aorta provide some measure of the magnitude of the concentration polarization of LDL in medial matrix. The molecular sieving by the superficial layers of the artery wall produce a 40 percent increase in the intimal LDL concentration at 100 mm Hg. While one can argue that this tissue is very likely hydrated, one asks whether the roughly five percent changes in measured porosity of intact arteries in Tedgui and Lever (1987) between 70 and 180 mm Hg would be of sufficient magnitude to produce such drastic changes in transport (Peclet number) in the superficial layers of the intima. The theoretical prediction for the change in effective diffusivity with average fiber spacing using random matrix theory in Fig. 4 of Huang *et al.* (1994) suggest otherwise.

We believe that a more likely explanation of the 50 fold increase in concentration of the LDL is that, first, there may be a large increase in macromolecular permeability of the endothelium at high pressure (see next paragraph); and second, LDL may either bind to medial matrix or to medial smooth muscle cells and/or be internalized by these cells. Although the intima comprises probably no more than 10% of the first wall section, according to our theory it possesses a much higher available volume for LDL than the media. Since other studies have shown that only a small fraction of the LDL that enters the intima binds there, intimal LDL washout could then account for the 40 percent drop in LDL concentration that occurs in the first wall section . Unfortunately, Curmi et al. did not continue their washout experiment to distinguish binding from medial compaction by subsequently dropping the pressure to

70 mmHg for 30 minutes and seeing if the accumulated LDL then washed out.

Since albumin is nearly completely removed after a 30 minute washout, it neither binds nor becomes matrix-entrapped. While concentration polarization of albumin by endothelial surface glycocalyx is consistent with the observations of Adamson (1990), Adamson and Clough (1992) of the surface matrix layer in microvessels, it is difficult to explain the sieving of albumin in the deeper subendothelial tissue. Even at high filtration rates in denuded minipig aorta, Fry (1986) observed only a 15% increase in albumin concentration due to concentration polarization. The authors suggest that at 160 mmHg, either the integrity of the endothelial junctions is compromised or new endothelial pores for macromolecules that are beyond the resolution of Curmi *et al.*'s *en face* micrograph have formed. Michel (private communication) has observed the appearance of fenestral-like openings near the clefts of frog mesentery endothelium at high capillary pressures. These pores might provide an additional pathway for large molecules. Finally, the absence of an intimal spike in the albumin accumulated at 160 mmHg suggests that the IEL's fenestrae present no significant transport barrier for albumin. In summary, while one cannot rule out medial compaction in the intact artery as the cause of the dramatic changes in the albumin and LDL profiles at 160 mm Hg in Curmi *et al.*, (1990), other explanations appear to better fit the magnitude of the observed changes.

Fig. 3.10 suggests a new experiment to test our basic hypothesis. One anticipates that there will be a large reduction in the growth of HRP spots in the rabbit aorta when P_L^* increases from 50 to 100 mmHg if the intima is indeed compressible and little

change if it is firm. Another interesting prediction in Fig. 3.10 is the rise time to achieve the asymptotic spot size. At high pressure this rise time is very short. The large intimal resistance causes the convective flow through the leaky cleft that would normally be parallel to the endothelium to be partially redirected towards the media.

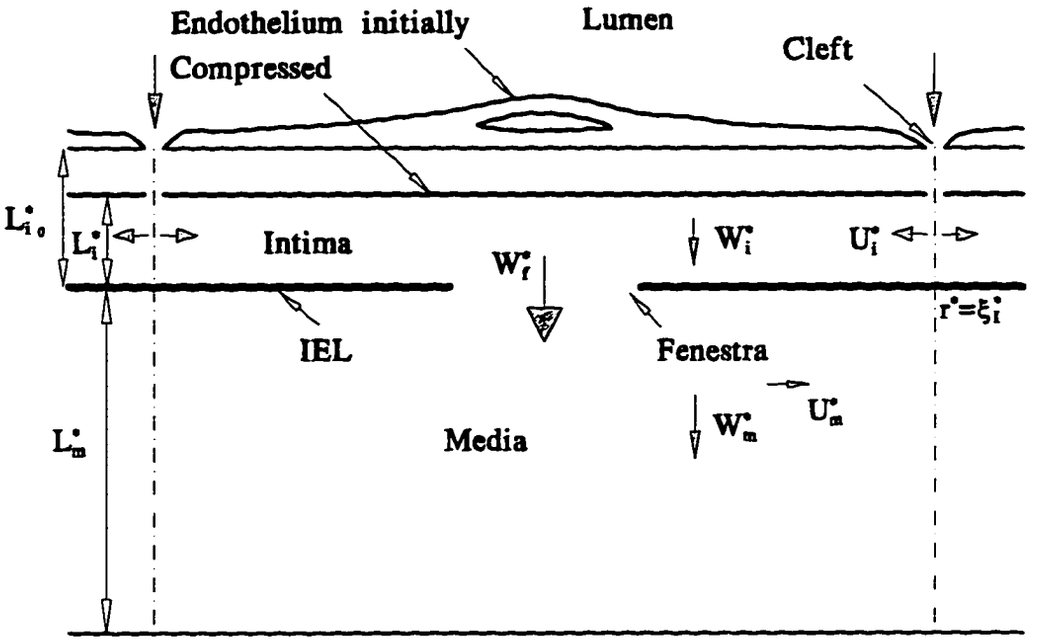

Fig.3.1 Schematic illustration of the local, periodic wall unit around a fenestral pore. The intima under a nondeformable endothelium is compressible; L_{i0}^* is the initial intimal thickness at zero transmural pressure.

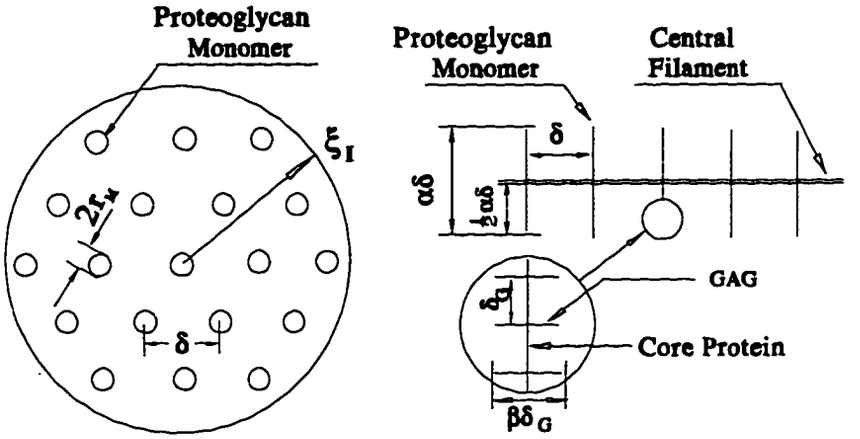

(a) Top View **(b) Proteoglycan Aggregate**

Fig.3.2 Sketch of simplified proteoglycan matrix model for calculating the void volume of the region considered. (a) is the top view of the region. (b) shows the structure of proteoglycan aggregate.

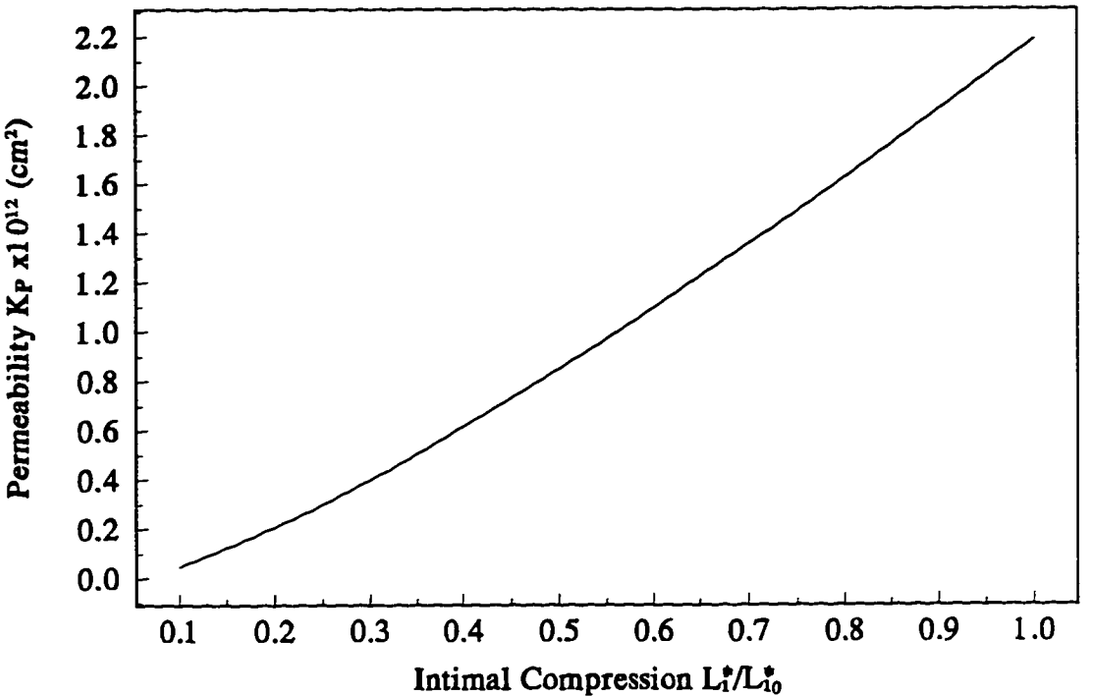

Fig.3.3 Darcy permeability K_p as a function of the intimal thickness ratio L_i^*/L_{i0}^*.

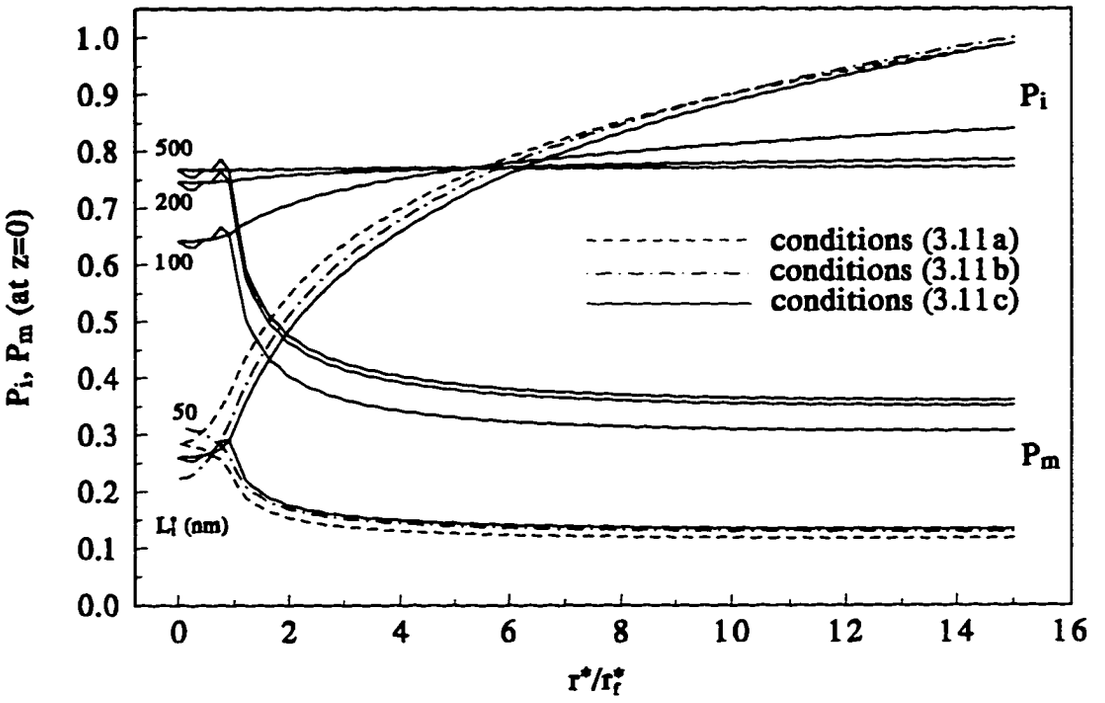

Fig.3.4 The local pressure distributions on the upper (intima side, P_i) and lower (media side, P_m) IEL surfaces for different intimal thicknesses. The matching conditions at the fenestral pore are equations (3.11a), (3.11b) and (3.11c) for L_i^*=50 nm and equation (3.11c) for all other intimal thicknesses. L_{i0}^*=500 nm.

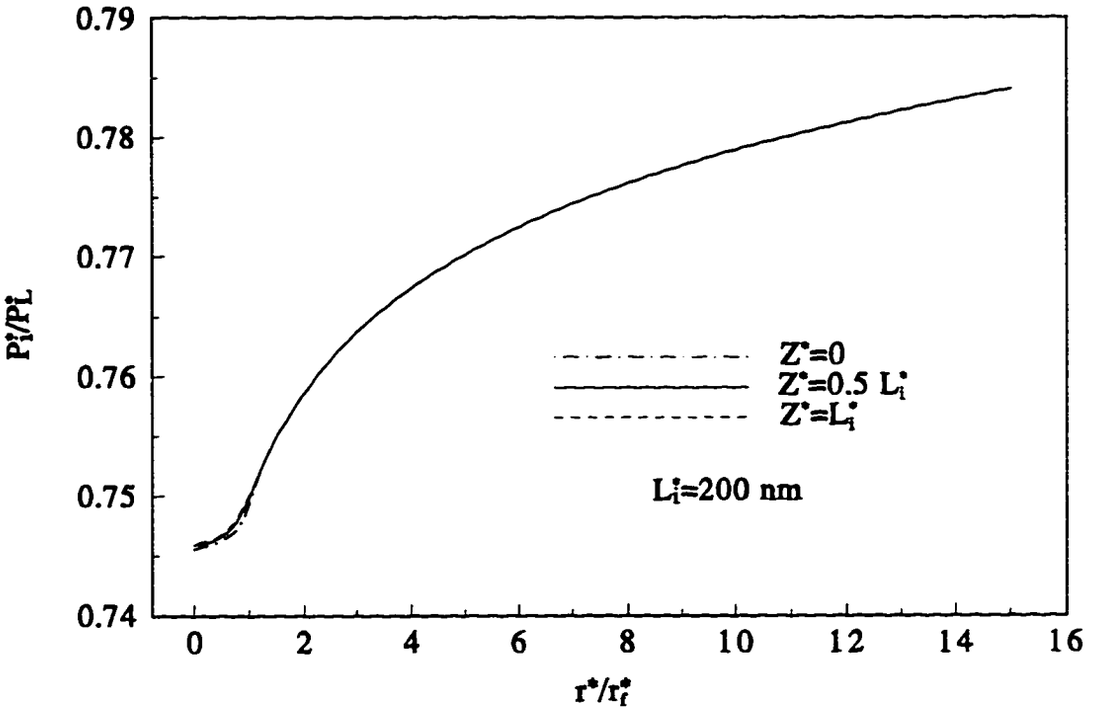

Fig.3.5 The local pressure distributions at $z^*=0$, $0.5L_i^*$ and L_i^* in the intima for intimal thickness $L_i^*=200$ nm. $L_{i0}^*=500$ nm.

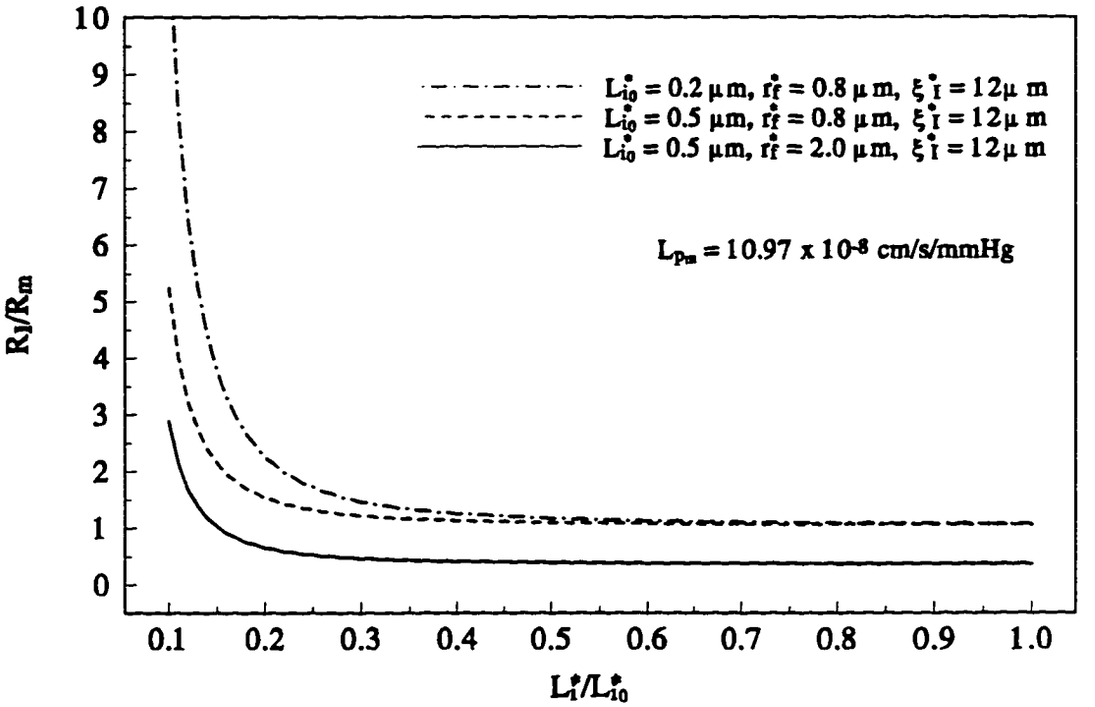

Fig.3.6 The ratio of the resistance R_l across the IEL plus the intima to the resistance R_m across the media as the function of L_i.

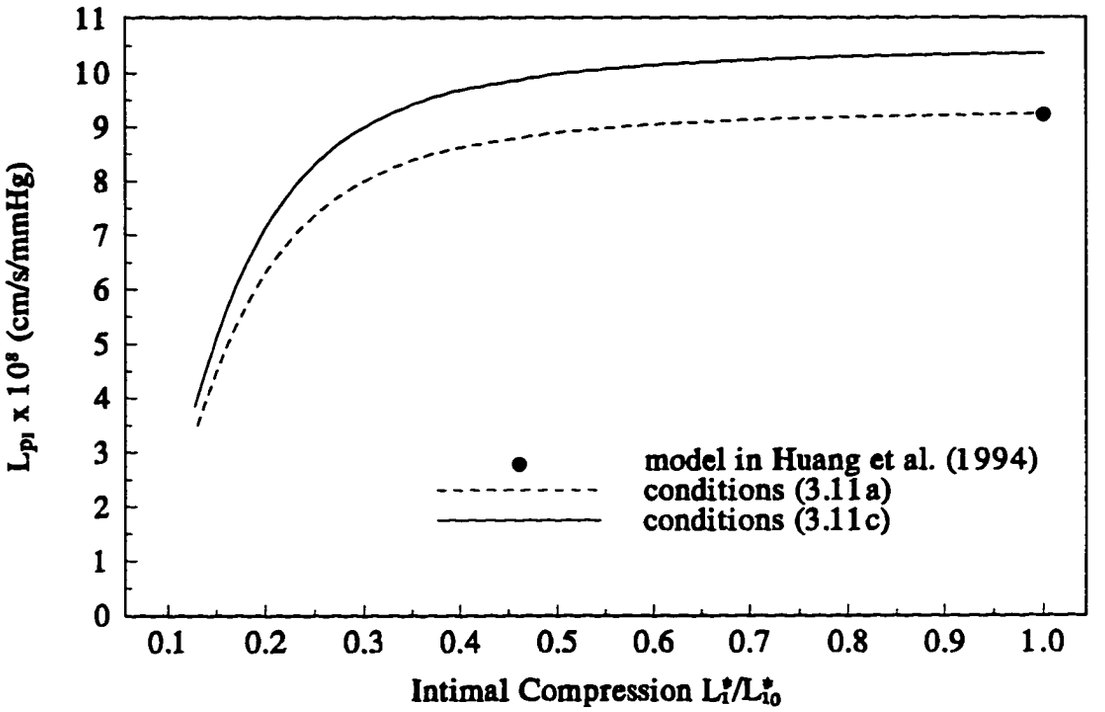

Fig.3.7 The comparison between the L_{pl} value predicted by the present model and that obtained using the previous model in Huang *et al.* (1994). L_{pl-m}=5.32 x 10^{-8} cm/s/mmHg at $L_i^*=L_{i0}^*$=500 nm.

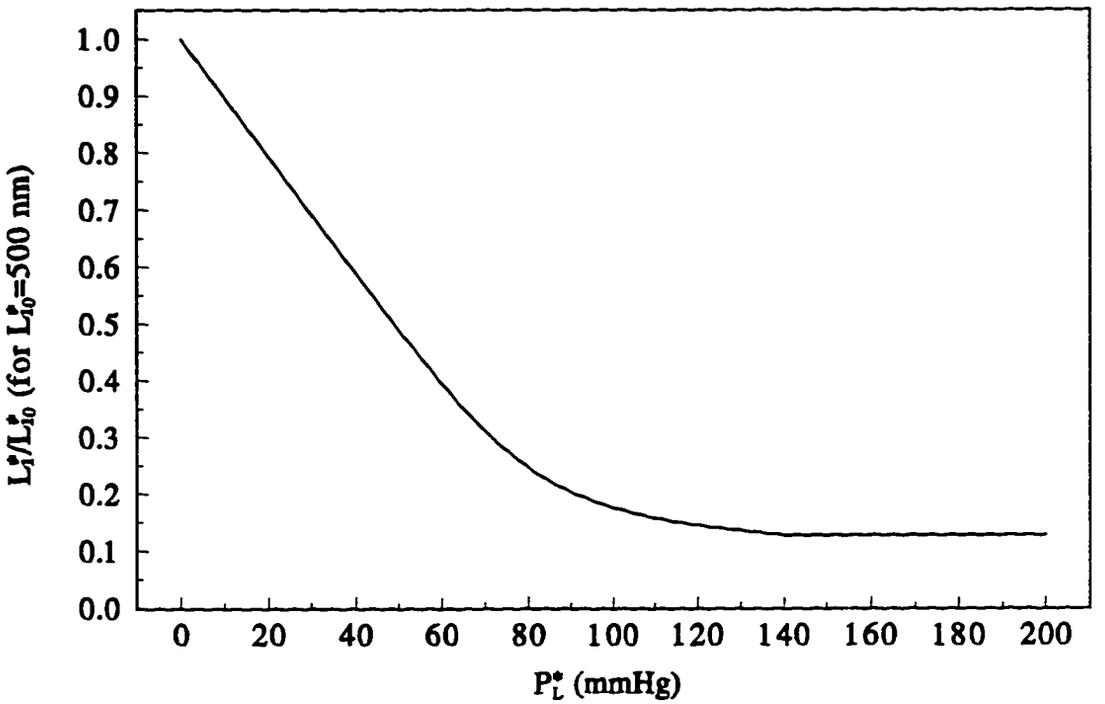

Fig.3.8 The non-linear relationship between the lumen pressure and the intimal thickness. L_{pm}=11.0 x 10^{-8} cm/s/mmHg. L_{pe}=18.0 cm/s/mmHg and k=22.

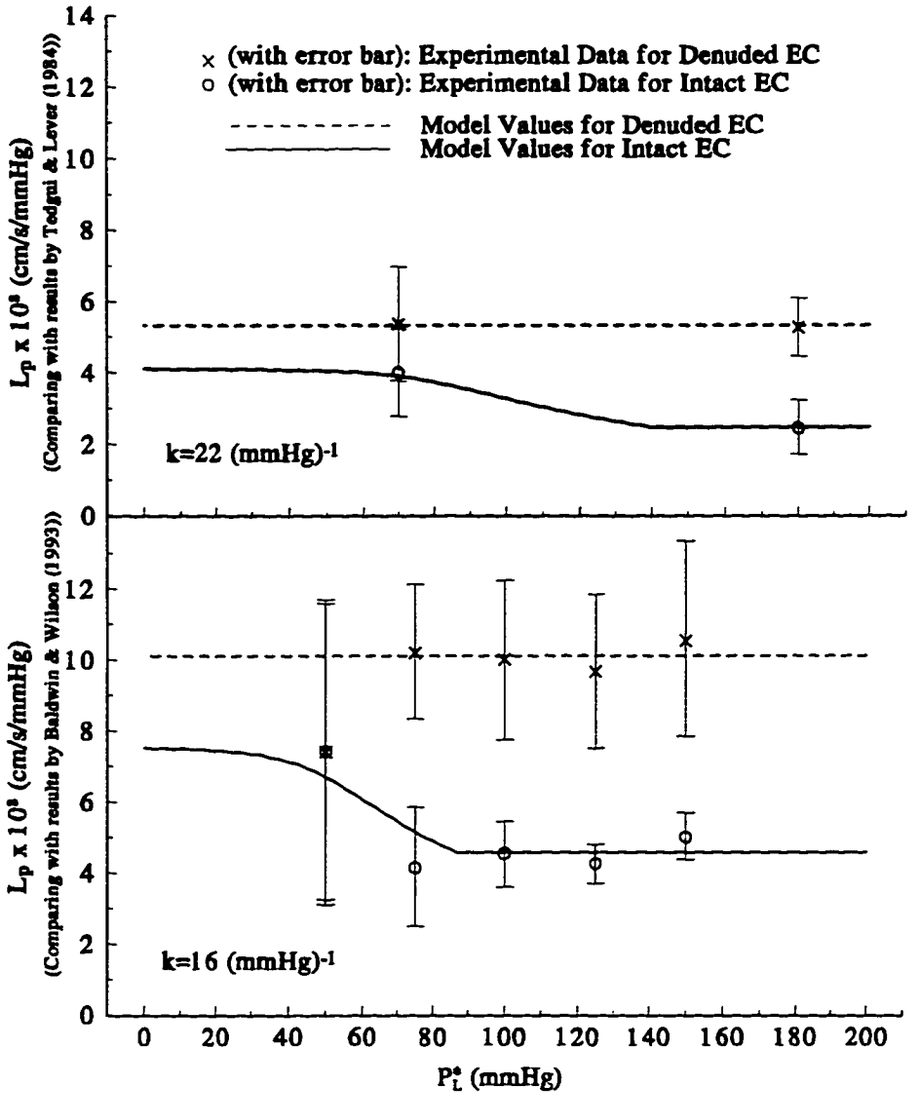

Fig.3.9 Comparison of the model's pressure-dependent hydraulic conductivity in the intact artery wall with the experimental measurements from Tedgui and Lever (1984) and Baldwin and Wilson (1993).

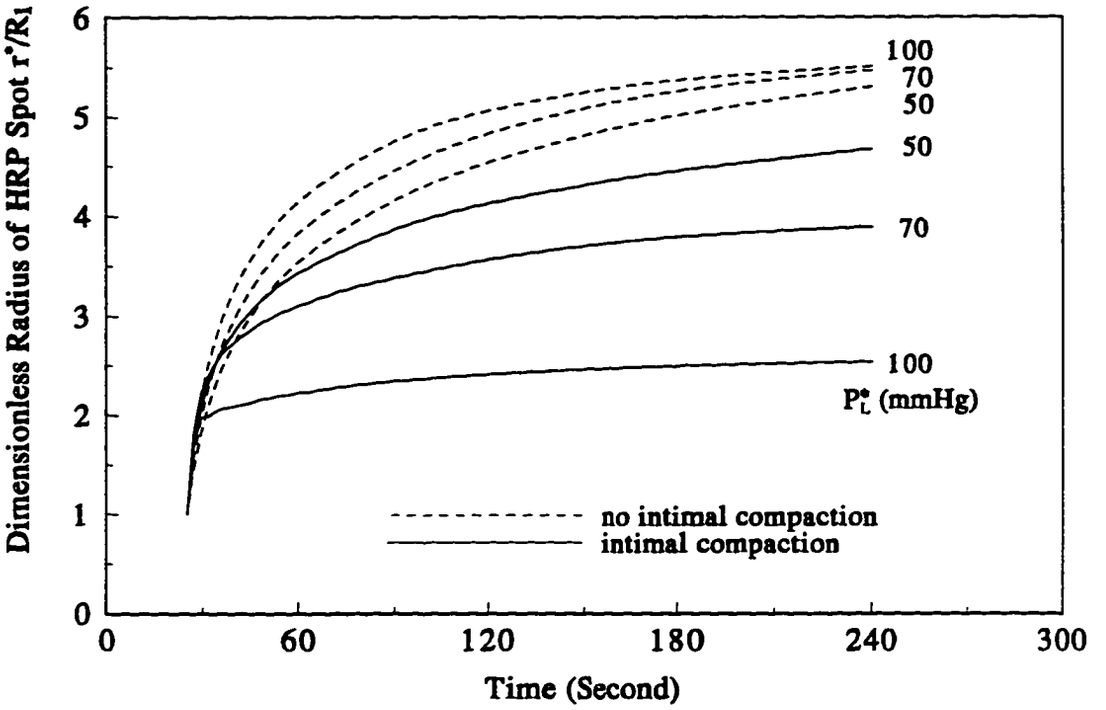

Fig.3.10 The predicted time dependent HRP spot sizes for several different transmural pressures in the rabbit arterial intima. L_{pm}=11.0 x 10^{-8} cm/s/mmHg, L_{pe}=18.0 cm/s/mmHg and k=22. R_1=15 μm.

Chapter 4

Structural Changes in Rat Aortic Intima due to Transmural Pressure

4.1 Introduction

Recent studies (Yuan *et al.*, 1991; Huang *et al.*, 1994) have advanced a new view of water flow and macromolecular transport in the arterial intima. The model for filtration assumes that water crosses the endothelium through all endothelial cell junctions and then spreads laterally in the thin intima before seeping through the fenestral pores of an otherwise nearly impermeable internal elastic lamina (IEL). In these initial studies we neglected the effect of transmural pressure on intimal matrix porosity and IEL pore size. In Chapter 3 we developed a local model for the filtration through fenestral pores in a compressible arterial intima and advanced a new hypothesis to explain how the transmural pressure affects the hydraulic conductivity of the artery wall. This hypothesis suggests that the compaction in the subendothelial intima in the vicinity of the IEL fenestrae can account for the large decrease in the hydraulic conductivity that Tedgui and Lever (1984) and Baldwin and Wilson (1993) measure with increasing transmural pressure in an intact artery wall. The mathematical model predicts that at lumen pressures > 75 - 100 mm Hg there is a five-fold decrease in

intimal thickness and a marked, non-linear steepening of the radial intimal pressure profile near the fenestral pores. If the endothelium is deformable and the local deformation is proportional to the local transendothelial pressure difference, the large drop in intimal pressure as one approaches the fenestral pore would lead to a large, marked endothelial deformation; it would steepen near the edge of pore, bottom out over the fenestral pore and lead to a partial pore blockage. In an *en face* study by Lee and Chien (1979) the scanning electron micrograph shows that at pressures above ~ 80 mm Hg, small crater-like depressions appear on the endothelial surface. These surface indentations had previously been unexplained.

Ultrastructural observations of the intima (Frank and Forgelman, 1989) reveal that the intimal matrix is far less dense than the matrix in the media and the healthy intima is, furthermore, cell-free. The intima has a vastly different proteoglycan structure than the media and the matrix in the fenestral pores of the IEL has a structure which appears to be a continuation of the intimal matrix (Lark *et al.*, 1988; Wight and Hascall, 1983). These results suggest that the intima should be more compressible than the media.

In this chapter we conduct a theoretical and experimental study to (i) characterize the IEL's fenestrae in rat aorta, to (ii) test whether intimal compression due to transmural pressures occurs and to (iii) see if this compression is large enough to account for the measured pressure-induced changes in artery wall hydraulic conductivity in Tedgui and Lever (1984) and Baldwin and Wilson (1993). We perfusion-fixed rat thoracic aortas in situ at 0 mm Hg or 100 mm Hg lumen pressure, the former

corresponding to the relaxed state of the intima and the latter to a physiological pressure that happens to be in the range where the observed hydraulic conductivity dependence on the transmural pressure has become insensitive to further pressure increases (Baldwin and Wilson, 1993), and sectioned for light and electron microscopic observations. We measured the dimension and the number of the fenestral pores from light micrographs of transverse sections and calculated the average pore diameter and the fractional pore area using quantitative stereology. Using a cutting probability, we converted the measured pore dimensions into an IEL pore diameter distribution. The experiments described herein provide the first direct measurements of intimal compaction at high lumen pressures. These experiments strongly support the hypothesis advanced in Chapter 3 for the decrease in hydraulic conductivity at elevated transmural pressure.

4.2 Methods

4.2.1 Animal Experiments

4.2.1.1 Aorta Preparation

This study uses two adult male rats weighing approximately 300-400 g. The rats were anesthetized with intraperitoneal injection of chloral hydrate solution. The neck of one rat was dissected by a midline incision to expose the carotid artery. A ligature was tied around the carotid artery which was cannulated and then 30 units of heparin was injected. The heart was stopped with saturated KCl solution. After flushing with 10 ml phosphate-buffered saline (PBS) at PH=7.4, we perfusion-fixed the vessels *in situ* at room temperature with 2% glutaraldehyde in PBS under a constant lumen pressure

of 100 mm Hg and cut the left femoral vein to drain the perfusate. Figure 4.1 shows the experimental setup for this perfusion. Syringes filled with solutions are connected to an air reservoir linked to a sphygmomanometer which monitors and controls the pressure. After 90 minutes pressure-fixation. we opened the rat's chest. removed the thoracic aorta and cut it into several segments. We further fixed all pieces in the glutaraldehyde solution for another 30 minutes.

After anesthesia we opened the chest of a second. control rat. and injected heparin into the heart. After flushing with PBS. we slowly injected 40 ml 2% glutaraldehyde solution into the left ventricle. Meanwhile. we cut the left femoral vein. The thoracic aorta was removed and fixed in 2% glutaraldehyde solution (0 mm Hg transmural pressure) for 2 hours and sectioned into several segments .

All glutaraldehyde-fixed segments were washed in PBS at PH 7.4. postfixed in 2% OsO_4 in PBS for 90 minutes. washed three times in PBS. and step dehydrated in ethanol and propylene oxide. Then they were embedded in Eponate 12 resin (Ted Pella Inc.. Redding. CA) and polymerized at 60°C for two days.

4.2.1.2 Light and Electron Microscopic Observations

We made the serial transverse sections with thicknesses of 100. 200. 300 or 500 nm from the resin blocks using an MT2-B Ultra Microtome for the light microscopy. All slices were collected in order. fixed on the slides with 2% gelatin. and stained with 1% orcein in acid ethanol for 2 minutes. followed by washing in 70% ethanol. Using the light microscope with an oil emersion lens. we searched for endothelial indentations.

observed the geometrical changes of the IEL between 0 and 100 mm Hg pressure and took microphotographs for the measurements of pore size, density, and wall thickness.

Random transverse sections with a thickness of 60 nm were made using a MT6000 ultramicrotome for the electron microscopy. All sections were poststained with lead citrate. Using a JOEL JEM-100S electron microscope, we observed the endothelial indentations and the changes of the intimal thickness with lumen pressure. Since intimal thicknesses are highly irregular locally (see Figs. 4.8), we determined average values for each slice by measuring the intimal area and dividing by the length of IEL.

4.2.2 Quantitative Stereology

From the transverse sections of the aorta, one can only measure the two dimensional structure of the fenestral pores. Using quantitative stereology (Underwood, 1970; Weibel, 1963), one can calculate the fractional area and the average diameter of the fenestral pores, which is not directly accessible from the two dimensional microtome slices.

4.2.2.1 Fractional Area of Fenestral Pores

Because the slices are all parallel, an interesting relationship between areas and lengths obtains. As in Underwood (1970) and Weibel (1963), Fig. 4.2 (a) represents a square sample of IEL of area $A_{IEL} = L^2$ parallel to the xy-axes which contains some randomly distributed pores and a line in it parallel to the y-axis. A fraction $L_{pore}(x)/L$ of this line lies in one or more pores. The ratio ϕ of the total pore area A_{pore} in A_{IEL} to

A_{IEL} is

$$\phi = \frac{A_{pore}}{A_{IEL}} = \frac{1}{A_{IEL}} \int_0^L L_{pore}(x)dx = \frac{\overline{L_{pore}}L}{A_{IEL}} = \frac{\overline{L_{pore}}}{L} \tag{4.1}$$

where

$$\overline{L_{pore}} = \frac{1}{L_0} \int_0^L L_{pore}(x)dx \tag{4.2}$$

is the average pore length (see Fig. 4.2 (b)) defined by the integral mean value theorem. which is equal to $L_{pore}(x^*)$ for some $0<x^*<L$.

Thus

$$\phi = \frac{A_{pore}}{A_{IEL}} = \frac{\overline{L_{pore}}}{L} = L_L \tag{4.3}$$

where L_L is the length of lineal intercepts per unit length of test line. Thus. the experimental fractional length of the pore intercepts for parallel slices estimates the fractional area of the fenestral pores.

4.2.2.2 The Average Pore Diameter

The raw data that we collect is a number N_L of gaps corresponding to chords of fenestrae in a large number of parallel slices and the length of each gap. totalling L_L. where N_L and L_L are per-unit-total-length-examined. If the pores are circular at 0 mm Hg and elliptical at 100 mm Hg. the aorta having been stretched radially only and not axially. then one can come up with an average pore radius R for each pressure in terms

of N_L and L_L.

Figure 4.3 is a illustration of some geometrical parameters of the aorta. Let a be the fenestral pore's radius at zero pressure and let b and a be its elliptical major and minor axes at non-zero pressure. r and h are the radius and wall thickness of the aorta, respectively. We use the subscript zero to indicate a corresponding value at zero transmural pressure. The results in Tedgui and Lever (1987) reveal that for the intact vessel there is very minor hydration of the wall and both the water volume and sucrose space are nearly constant at pressures up to 180 mm Hg. Therefore, the volume of wall can be assumed to be nearly unchanged during the change of the lumen pressure (Tedgui and Lever, 1987), which yields

$$2\pi rh=2\pi r_0 h_0 \tag{4.4}$$

If all displacements in the azimuthal direction are linear with the increase in circumference with pressure, then

$$\frac{b}{a}=\frac{2\pi r}{2\pi r_0}=\frac{h_0}{h} \tag{4.5}$$

An elliptical pore has area $S_{pore}=\pi ab$ and perimeter $C_{pore}=kb$ where

$$k=4\int_0^{\frac{\pi}{2}}\sqrt{1-[(\frac{a}{b})^2-1]\sin^2 t}\,dt \tag{4.6}$$

Let us define an effective pore radius $R=\sqrt{(ab)}$ by setting $S_{pore}=\pi R^2$. It remains now to come up with an expression for R as a function of N_L and L_L, rather than of a and b. In the following derivation, S_{pore} and C_{pore} represent the mean values of the pore area

and perimeter.

Let L_A be the length of pore perimeter per unit test area and N_L be the number of fenestral chords defined previously. Using a scheme similar to that in Weibel (1963). we first obtain a relationship between L_A and N_L. We then use this relationship to derive an expression for R.

We choose the test IEL area A_{IEL} shown in Fig. 4.2. A set of m vertical test lines randomly passes through this area. and so the number of these lines per unit horizontal length is m/L. Let us approximate the perimeters of all of the pores in A_{IEL} by a set of n line segments. each of average length $\delta L=NC_{pore}/n$ where N is the number of fenestral pores in the A_{IEL}. The ith of these segments forms an angle θ_i with the vertical. and the length of a projection of the elementary segment on the horizontal is $\delta L \sin\theta_i$. Thus the fraction of test lines intersects the segment is $\delta L \sin\theta_i/L$.

If P_i is the number of test line intersections of the ith segment. then one can set the total number of intersections of test lines with segments equal to its expected value for a uniformly distributed random variable θ_i:

$$\sum_{i=1}^{n} P_i = m\sum_{i=1}^{n}(\delta L)\sin\theta_i/L = E(P) = \frac{m(\delta L)n}{L}\overline{\sin\theta} = \frac{mLNC_{pore}}{A_{IEL}}\overline{\sin\theta} \qquad (4.7)$$

where

$$\overline{\sin\theta} = \frac{2}{\pi}\int_0^{\pi/2}\sin\theta d\theta = \frac{2}{\pi} \qquad (4.8)$$

Let P_L be the number of intersections per unit test line length. Rearrangement of equation (4.7) gives

$$L_A=\frac{NC_{pore}}{A_{IEL}}=\frac{\pi}{2}\frac{E(P)}{mL}=\frac{\pi}{2}P_L \tag{4.9}$$

Since almost every intersection of a test line with a pore involves its intersecting two line segments (one to enter and one to leave), $2N_L=P_L$. Therefore.

$$L_A=\pi N_L \tag{4.10}$$

Let $S=A_{IEL}/N$ be the IEL area per pore. Then

$$\pi N_L=\frac{NC_{pore}}{A_{IEL}}=\frac{C_{pore}}{S} \tag{4.11}$$

and

$$L_L=\phi=\frac{NS_{pore}}{A_{IEL}}=\frac{S_{pore}}{S}\ . \tag{4.12}$$

Thus

$$S_{pore}=\pi R^2=\frac{L_L}{\pi N_L}C_{pore}\ . \tag{4.13}$$

Combining (4.5), (4.6) and (4.13) gives an expression for R in terms of N_L, L_L, h and h_0:

$$R=\frac{L_L}{\pi^2 N_L}\sqrt{\frac{h_0}{h}}\left\{4\int_0^{\frac{\pi}{2}}\sqrt{1-[(\frac{h}{h_0})^2-1]\sin^2 t}\ dt\right\}\ . \tag{4.14}$$

For a circular pore, $C_{pore}=2\pi R$, and (4.14) reduces to

$$R=\frac{2L_L}{\pi N_L} \quad . \tag{4.15}$$

4.2.2.3 Model for Diameter Distribution of Pores

Figure 4.4 illustrates that when one sections a single pore serially in 200 nm sections it is difficult to cut directly through the pore's center. Therefore, our measured pore dimension data from transverse sections represent pore chords rather than diameters. One can, however, convert the measured pore dimension distribution into a diameter distribution by introducing a cutting probability p(D:R) that a line segment that intersects a pore will have an intersection of length between D and D+ΔD, given that the pore is characterized by a size R. If one collects a sufficiently large number of intersection data, the distribution g(D) of the lengths of these intersections is related to p(D:R) and the distribution f(R) of pore sizes by

$$g(D)=\int_D^\infty p(R)f(R)dR \tag{4.16}$$

In practice one discritizes the histogram g(D) by introducing a non-zero ΔD. Then, (4.16) becomes

$$g(D_i)=\sum_{j=1}^{\infty} p(D_i:R_j)\Delta D f(R_j), \tag{4.17}$$

where one can, in practice, truncate this sum at a value $M \geq D_{max}/\Delta D$, where D_{max} is the largest observed chord. For a limited set of D_i, one can find $\{f(R_j): j=1, 2, \ldots, m\}$ by inverting the truncated matrix equation (4.17).

For a random cut of an ellipse parallel to its major-axis (see Figure 4.5), the probability p that the length of the intercept is between 2D and 2(D+ΔD) is the ratio of (x_1-x_2) to a, which is

$$p(D:R)\Delta D=\frac{x_1-x_2}{a}=\sqrt{1-(\frac{D}{b})^2}-\sqrt{1-(\frac{D+\Delta D}{b})^2}\approx\frac{\frac{D}{b^2}\Delta D}{\sqrt{1-(\frac{D}{b})^2}} \qquad (4.18)$$

Using the average radius R defined following equation (4.6), one can rewrite (4.18) as

$$p(D:R)\Delta D=\sqrt{1-\frac{a}{b}(\frac{D}{R})^2}-\sqrt{1-\frac{a}{b}(\frac{D+\Delta D}{R})^2}\approx\frac{\frac{a}{b}\frac{D}{R^2}\Delta D}{\sqrt{1-\frac{a}{b}(\frac{D}{R})^2}} \qquad (4.19)$$

4.3 Results

4.3.1 Endothelial Indentation

As mentioned in the introduction, our theoretical model (Chapter 3) predicts that if the subendothelial intima is compressible and if the local endothelial deformation is proportional to the local transendothelial pressure difference, then endothelial indentations should appear over the fenestral pore at higher lumen pressures due to the large pressure drop that will occur in the vicinity of the fenestral pore. Our light and electron microscopic observations of transendothelial sections at 100 mm Hg lumen pressure have verified this prediction. We observe numerous endothelial indentations over the fenestral pores, particularly in regions where the endothelium is thin, i.e. far

from the cell nuclei. Figures 4.6a and 4.6b are electron and light micrographs showing typical endothelial indentations at 100 mm Hg lumen pressure. No endothelial indentations are evident at 0 mm Hg pressure. This behavior is consistent with the theoretical prediction in Chapter 3.

4.3.2 The Changes of Intimal and Wall thickness with Pressure

The shape of the IEL at 0 mm Hg is quite different from that at 100 mm Hg: At 100 mm Hg pressure the IEL is flat, whereas for 0 mm Hg it is highly undulated (see Figure 4.7).

We measured the intimal thickness of the rat thoracic aorta for 0 mm Hg and 100 mm Hg from light micrographs. The mean wall thickness, 75 μm, of aortas fixed at 100 mm Hg is 75 percent of the thickness, 100 μm, of vessels fixed at 0 mm Hg.

Figures 4.8a,b show the subendothelial intima at 0 mm Hg and 100 mm Hg, respectively. Tables 4.1a and 4.1b present the measured results for the average intimal thickness for eight micrographs at 0 mm Hg and eight micrographs at 100 mm Hg. To calculate mean intimal thickness we measured the intimal area in μm^2 and divided this by the length in μm of the intima in each electron micrograph.

Table 4.1a. Mean intimal thickness at 0 mm Hg lumen pressure

Number	area (μm^2)	Length (μm)	mean thickness (μm)
1	14.3	24.9	0.573
2	6.75	15.4	0.439
3	16.3	30.5	0.534
4	9.97	26.3	0.380
5	11.8	26.3	0.448
6	4.02	21.1	0.190
7	3.56	18.3	0.195
8	11.8	25.9	0.458
total	78.5	189	0.42±0.14 (SD)

Table 4.1b. Mean intimal thickness at 100 mm Hg lumen pressure

Number	area (μm^2)	Length (μm)	mean thickness (μm)
1	2.19	23.8	0.092
2	3.13	21.5	0.145
3	3.36	21.9	0.154
4	1.09	23.4	0.047
5	1.72	21.3	0.081
6	1.95	22.8	0.086
7	3.44	18.8	0.183
8	2.63	26.4	0.100
total	19.5	180	0.11±0.04 (SD)

Because the intimal thickness is no more than 1% of the wall thickness, one can equate the wall thickness with the medial thickness. Comparing the ratio, 0.26, of the

intimal thickness at 100 mm Hg to that at 0 mm Hg, with the ratio 0.75 of the medial thickness at 100 mm Hg to that at 0 mm Hg, one concludes that the compression of the subendothelial intima is dramatic compared with the change in medial thickness due to stretching.

4.3.3 Fractional Area and Average Diameter of the Fenestral Pores

In the section on Quantitative Stereology, we described how to estimate the fractional area and the average diameter of the fenestral pores by measuring the fractional length L_L of the pore intercept and the pore number N_L per unit length of test IEL line. We measured these values from hundreds of light micrographs, which were taken from eight randomly selected slices of 100 nm thickness. Figure 4.9 shows these measurements, which involve 653 pores. The average pore diameters were calculated using equation (4.14) with $h/h_0=1.3$ for 100 mm Hg pressure and equation (4.15) for 0 mm Hg pressure, respectively.

Table 4.2 shows the values (mean±SD) of the fractional area and the average diameter of the fenestral pores for 0 mm Hg and 100 mm Hg lumen pressure, respectively.

Table 4.2. Fractional area and average diameter of pores

Lumen pressure	0 mm Hg	100 mm Hg
Fractional pore area	0.052±0.003	0.054±0.003
Average pore diameter (μm)	2.02±0.13	2.32±0.19

It is evident from the data in table 4.2 that there is only a small difference in the fractional pore area between the 0 and 100 mm Hg lumen pressure specimens. The measured value of the fractional pore area, ~5%, in the rat thoracic aorta is larger than that measured in the sheep thoracic aorta, 0.13%-2.34% (Song and Roach, 1983) or in the rabbit thoracic aorta, 0.3% (Potter and Roach, 1983), and is similar to that measured at the bifurcation of human cerebral arteries, 1.8%-15% (Campbell *et al.*, 1981).

4.3.4 Diameter Distribution of the Fenestral Pores

Figure 4.10 shows the distribution of the fenestral pore diameters at 0 mm Hg lumen pressure as determined by stereology. This distribution is similar to that measured by Campbell *et al.* (1981) for the normal fenestrations at the bifurcations of human cerebral arteries. The peak of the distribution is at d=1.3 μm. Figure 4.10 clearly shows the difference between the distributions of pore diameters and of measured pore chords.

Discussion

Orcein provides a clear staining of elastin. We also tried Giemsa stain and toluidine blue, but orcein gave the best results. Using orcein stain one can clearly observe the fenestral pores in the IEL in the transverse sections of the aorta with light microscopy and one can easily measure the pore size and number from the micrographs. However, orcein does not provide a clear image of the endothelial cells. In some cases, the borders of the endothelial layer are too indistinct to determine whether endothelial

indentations occur over some pores. This is the reason we have been unable to quantitatively estimate the percentage of pores with endothelial indentations, although qualitatively we have indeed observed numerous indentations of the endothelium into the fenestral pores. The micrographs taken using the transmission electron microscope do show both the endothelium and the IEL very clearly. However, the electron microscopic observations are not very suitable for measuring the percentage of pores with endothelial indentations because one needs to make measurements over a large region. It would be better if one could find a dye which stains both the endothelium and the elastin, but which is inert for the other tissue components.

There are two major factors which might contribute to the difference between our data for the fractional area of the fenestral pores in the IEL of the rat aorta and those measured in the IEL of the rabbit (Potter and Roach, 1983) or the sheep aorta (Song and Roach, 1983). First, different animals may have different fenestral sizes and densities (number of pores per unit IEL area). Second, our experimental methods differ significantly from those of Roach and coworkers. In our experiments, we fix the aortas *in situ*, so as to maintain the IEL as close to the *in vivo* situation as possible when sectioning the aorta. In Potter and Roach (1983) and Song and Roach (1983), the investigators remove all non-elastin components using hot alkaline prior to the scanning electron microscopic observations. The experimental data in Song and Roach (1983) show that for different digestion times, the pore sizes, and especially the pore densities, are quite different. As the time of digestion increases, more pores appear in the IEL surface. The fractional area of the pores in the sheep thoracic aorta can increase from

0.13 to 2.34% with an increase of digestion time from 1 to 3 hours. When the aorta is immersed in 0.1 M NaOH at 70-90°C for 24 hours, the fractional area of the fenestral pores in the IEL increases to 5.77%, which is similar to what we have obtained in the rat thoracic aorta.

In our theoretical model of Chapter 3, we hypothesized that intimal compaction plays a significant role in modulating the total hydraulic conductivity across the intact artery wall. We predicted a non-linear relationship which links the intimal thickness with the lumen pressure. In the model, the intimal thickness of the rabbit aorta can decrease to about 15% of its unstressed value with the increase of the transmural pressure. The model also assumes that little additional intimal compaction occurs once the lumen pressure exceeds a "critical pressure" at which collagen fibers, which are much stiffer than the proteoglycan components, principally bear the normal load. When modeling the measured values of the pressure-dependent hydraulic conductivity in Baldwin and Wilson (1993) and Tedgui and Lever (1984), we predicted that there was about a five to sixfold intimal compaction in rabbit aorta at 100 mm Hg lumen pressure. In the present study, we have measured a fourfold intimal compaction in rat thoracic aorta at 100 mm Hg, which is close to the predicted values for rabbit aorta in Chapter 3. This discrepancy might in part be due to simplifications introduced in the mathematical model. When calculating the local pressure distribution in Chapter 3, we assumed that the compaction in the intima is uniform at each lumen pressure. This neglects the fact that, as discussed, one can expect an additional compaction in the vicinity of the fenestral pores due to the endothelial deformation at higher lumen

pressures. We anticipate that the larger intimal compaction in this local region will further decrease the local Darcy permeability, lower the local pressure and increase the total hydraulic resistance. Therefore, even if there is only fourfold intimal compaction in the region that is further removed from the pores, it is still possible to decrease the total hydraulic conductivity to the value estimated by the uniform compaction model, which predicts a five to sixfold average intimal compaction, due to the locally enhanced compaction that occurs in the vicinity of the fenestral pores. The present study demonstrates that the arterial intima is indeed very compressible, particularly compared with the medial thickness change due to stretching. However, because the results involve measurements at only two pressures, they cannot provide a relationship between the intimal thickness and the lumen pressure. We leave such measurements to a future study.

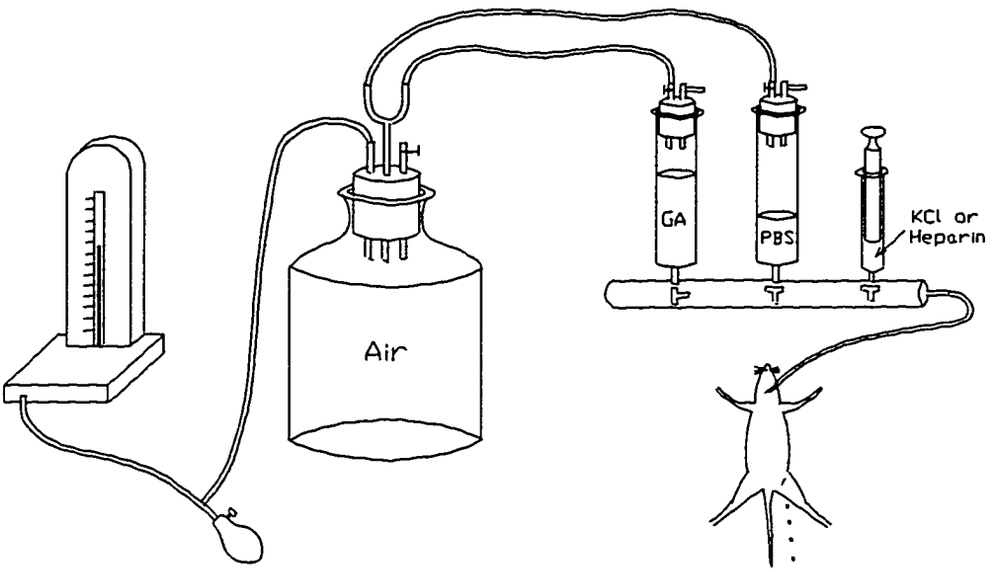

Fig.4.1 Schematic diagram of experimental setup for the perfusion *in situ* under a controlled pressure.

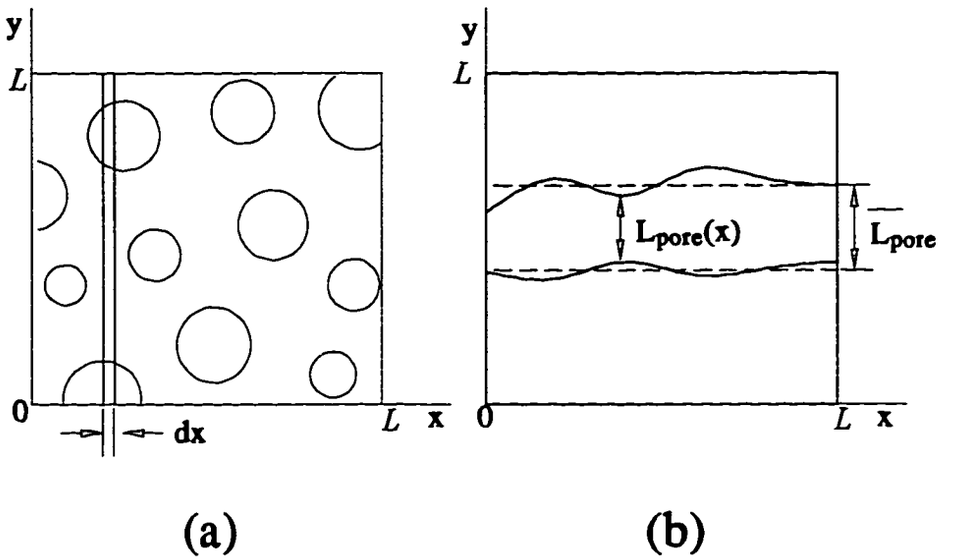

Fig.4.2(a): the IEL surface with the fenestral pores cut by the thin strip; (b) Measured $L_{pore}(x)$ and the mean value L_{pore}.

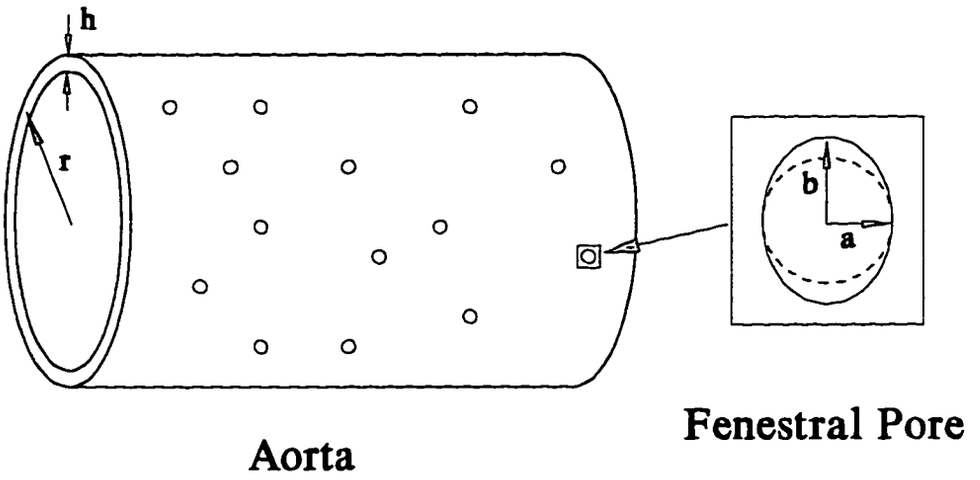

Fig.4.3 Schematic illustration of the geometrical parameters showing elliptical pores in a pressurized aorta.

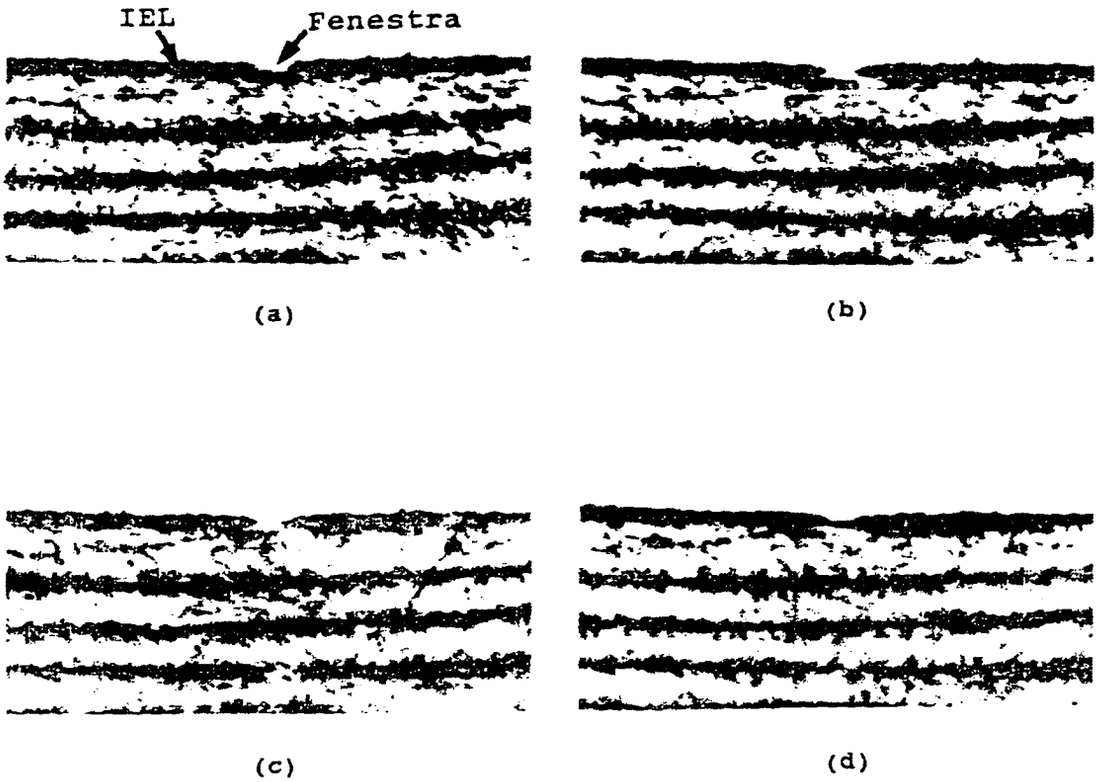

Fig.4.4 Serial section light micrographs traversing one fenestral pore. The thickness of each section is 200 nm. Magnification x 920.

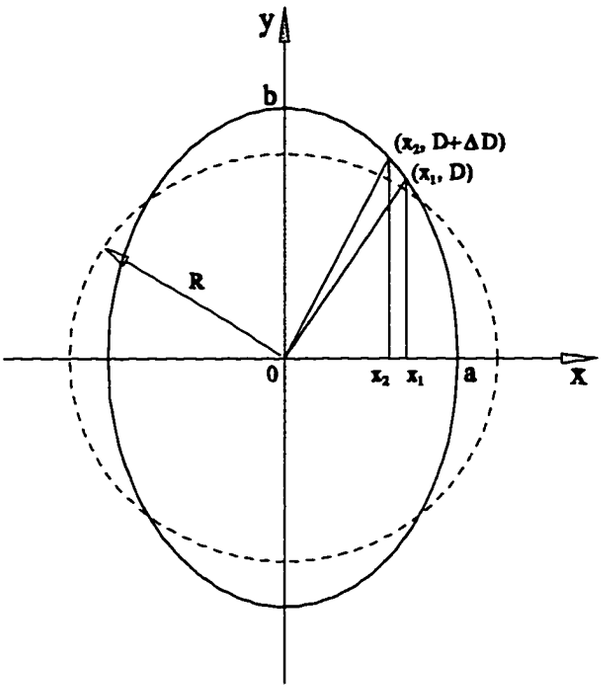

Fig.4.5 Model for deriving the relationship between the measured data obtained from the transverse sections, which are random chords across the pore, and the real diameters of the pores.

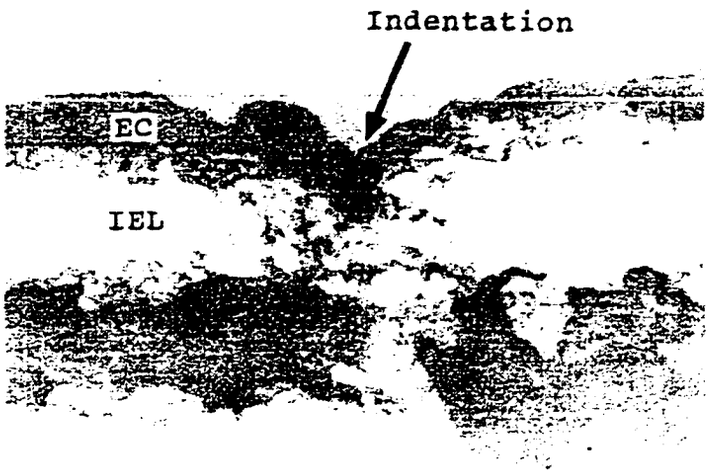

Fig.4.6a Electron micrograph of a typical endothelial indentation above the fenestral pore in the rat thoracic aorta fixed at 100 mm Hg pressure. Magnification x 12,000.

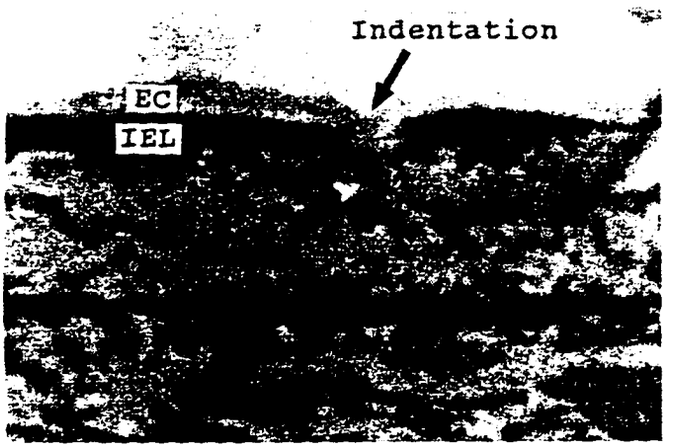

Fig.4.6b Light micrograph of a typical endothelial indentation above the fenestral pore in the rat thoracic aorta fixed at 100 mm Hg pressure. Magnification x 2700.

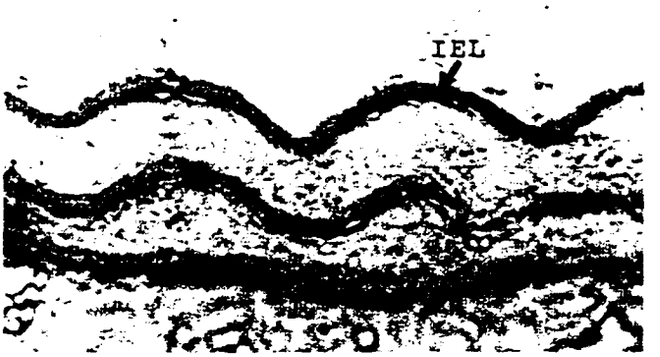

Fig.4.7 Light micrograph showing the shape of the IEL at 0 mm Hg pressure. Magnification x 920.

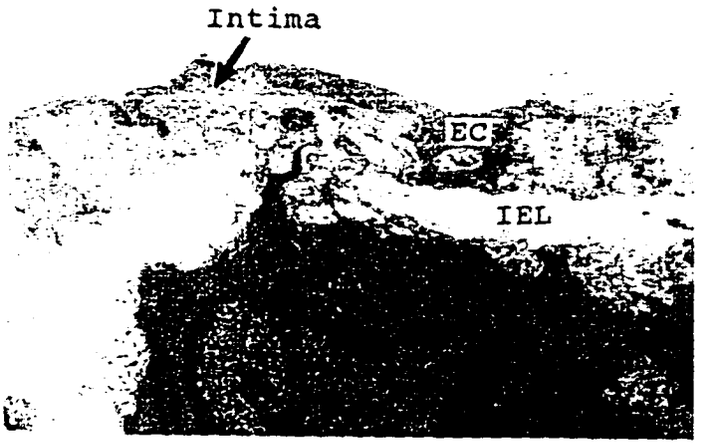

Fig.4.8a Electron micrograph showing the intimal thickness for 0 mm Hg pressure. Magnification x 8,000.

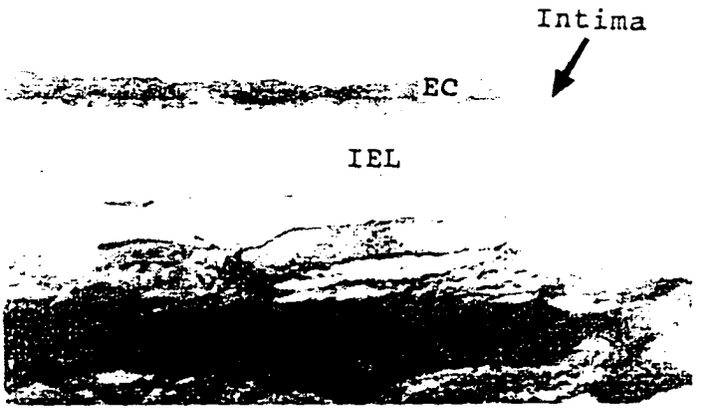

Fig.4.8b Electron micrograph showing the intimal thickness for 100 mm Hg pressure. Magnification x 8,000.

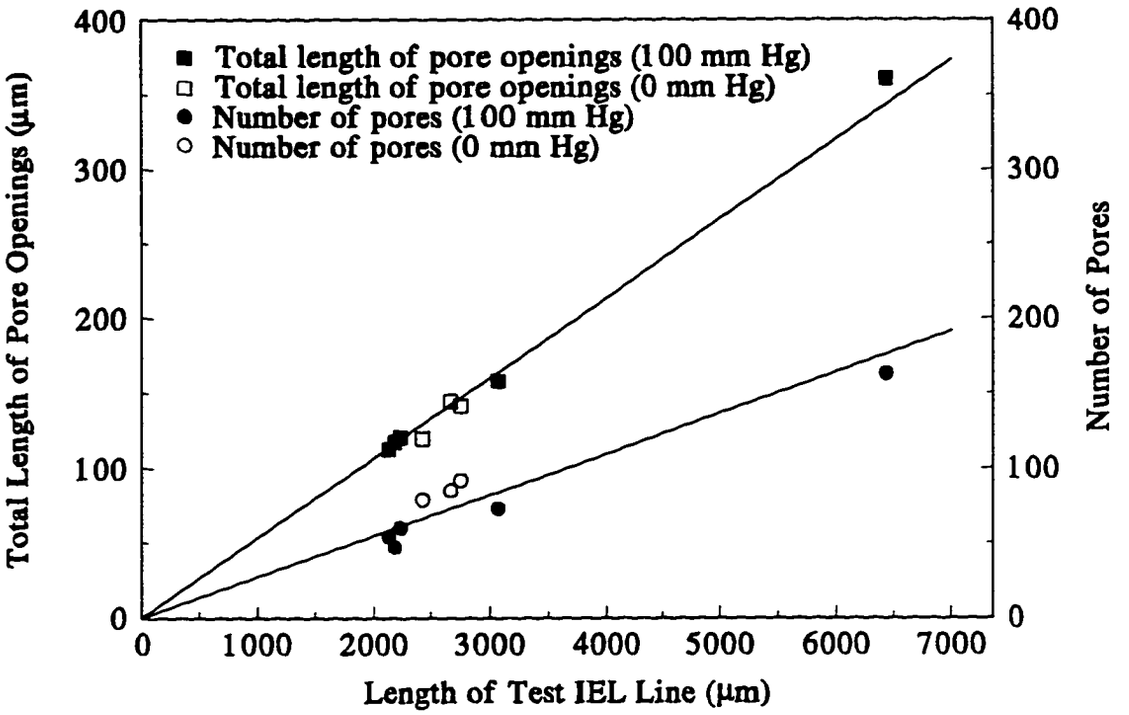

Fig.4.9 Measured data for total length of pore openings and number of pores in each test IEL line.

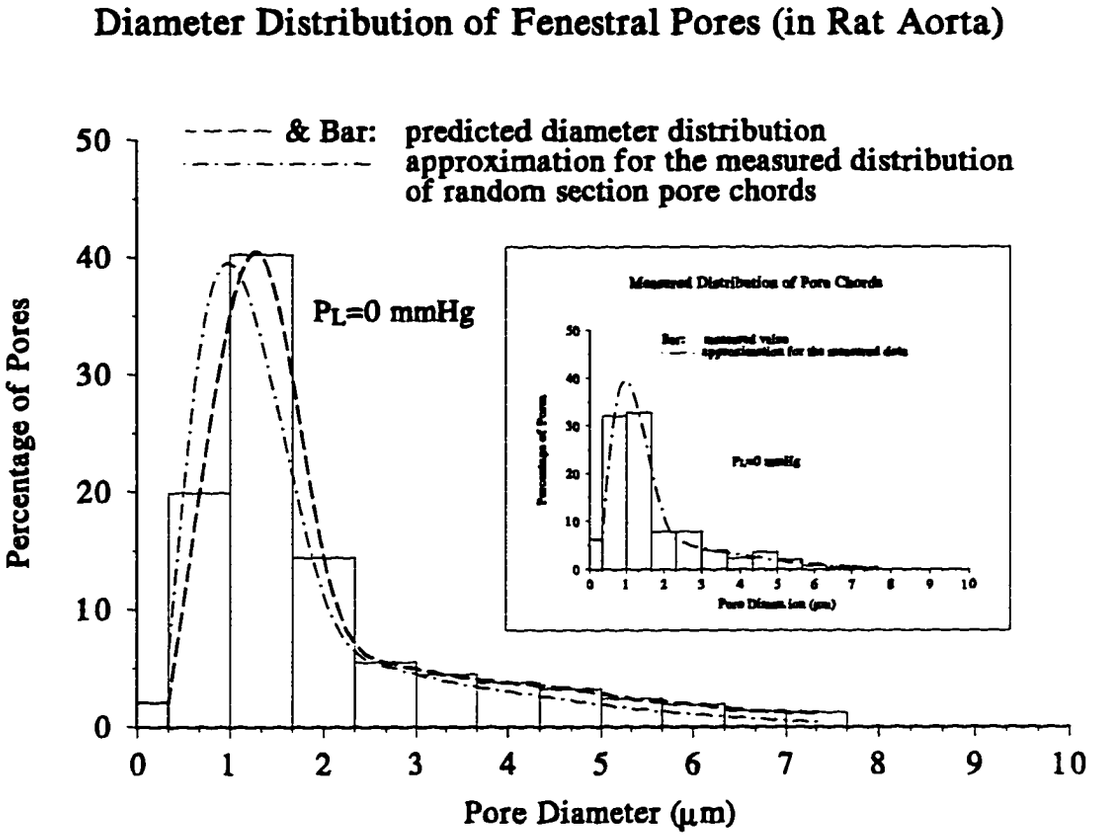

Fig.4.10 Comparison of the measured distribution of the pore dimensions and the predicted distribution of the pore diameters.

Chapter 5

Conclusion

The study in Chapter 2 presents a convective-diffusive filtration model of water flow and macromolecular transport in the artery wall. It goes beyond the earlier model in Yuan *et al.* (1991) in proposing a fundamental theory for predicting the permeability and hydraulic conductivity of the heterogeneous proteoglycan and collagen matrix that resides in the intima and in the fenestral openings of the IEL. Using these predicted values in the overall model provides for a much improved agreement with experiment for the growth of and concentration of the macromolecular cellular level leakage spots observed in the aortic intima of rat and rabbit. This model makes at least three significant predictions. First, the hydraulic conductivity L_{pi}^{*} in the intima is about 40~75 times larger than L_{pm}^{*} in the media (Tedgui and Lever, 1984), and the Darcy permeability $K_p = L_{pi}^{*}\mu\xi$ in the intima is about 130~250 times larger than $K_{pm} = L_{pm}^{*}\mu L_m$ in the media. This accounts for the proclivity towards initial lateral spot spread rather than trans-IEL transport. This abrupt change in the structure of the interstitial matrix at the IEL-media interface is supported by immunolocalization studies of the constituent proteoglycans using monoclonal antibodies. Second, in the region $r \leq \xi/5$ (ξ is about $45R_f$ for $R_f = 15\mu m$ and $\phi = 0.0005$), lateral convection is a significant factor for

macromolecule transport in the intima. Thus, macromolecules spread very rapidly in the lateral direction during the first few minutes after leaking into the intima (Chuang *et al.*, 1990) and the region containing a measurable concentration of macromolecules then approaches a limiting radius as the flow through the leaky cleft penetrates the nearby fenestrae in the internal elastic lamina. Third, the comparison of predicted LDL spot size and the average local concentration of ^{125}I-LDL in the leakage spots with the measured values in Truskey *et al.* (1992) strongly suggest that there is molecular sieving at the IEL-media interface supporting the hypothesis proposed earlier by Fry and co-workers (1986).

Chapter 3 presents a new, local, two-dimensional model for the filtration flow through the fenestral pores in a compressible intima. It considers for the first time the role played by the compaction of the arterial intima in modulating the total hydraulic conductivity of the intact artery wall with changes in the transmural pressure. The model provides several important predictions. First, the model's agreement with measurements for the relative change of hydraulic conductivity with transmural pressure supports the quantitative feasibility of our hypothesis that increased transmural pressure compacts the arterial intima near the IEL fenestral pores and causes the associated hydraulic conductivity changes. Second, there is a marked, non-linear steepening of the radial intimal pressure profile near the fenestral pore when the intima significantly compacts. One thus anticipates that the endothelium deforms near the fenestral pores at high lumen pressures and that the primary pressure drop occurs near the pore's edge. This prediction for the endothelial indentations is consistent with the new experiments

in rat thoracic aorta showing such indentations (Fig. 4.6). Third, the one-dimensional behavior exhibited in the intima for the intimal velocity and pressure distribution suggests that a 1-D approximation for these flow variables will be adequate in a more complex elastohydrodynamic model for a deformable intima to relate endothelial deformation to the local subendothelial pressure field. Fourth, a simple linear elastic behavior for intimal matrix compression is only suitable at low transmural pressures. One anticipates, based on the experimental data, that the loose proteoglycan matrix first compresses at small transmural pressures less than 75 to 100 mmHg; the matrix then exhibits a much stiffer behavior in which the collagen matrix predominantly carries the normal load.

The study presented in chapter 4 for the structural changes in rat aortic intima due to transmural pressure provides the first direct experimental evidence of intimal compaction and endothelium indentation at higher lumen pressures. Following the theoretical predictions in Chapter 3, we find, in both light and electron microscopic observations, numerous sites where the endothelium indents into the fenestral pores at 100 mm Hg. Electron micrographs of the aorta sections show that the subendothelial intima is, indeed, very compressible. We have measured a near fourfold intimal compaction in rat thoracic aorta at 100 mm Hg compared to its initial thickness at 0 mm Hg. This result is close to the predicted values for intimal compression for the rabbit aorta in Chapter 3. These light and electron microscopic observations are consistent with the intimal compaction hypothesis in Chapter 3 and its prediction of a marked, non-linear intimal pressure drop near the fenestral pores at higher lumen

pressures, with a pronounced endothelial deformation at these sites. We have also measured for the first time the change in the IEL's fenestrae due to pressure loading. To this end, we have measured and calculated the fractional area, mean diameter and diameter distribution of the fenestral pores in the rat thoracic aorta in both the relaxed state and at 100 mm Hg lumen pressure.

The research presented in this dissertation has led to a better understanding of water and macromolecular transport in the artery wall, especially in the subendothelial intima. The new theories and experiments in this study bring to light the key roles played by the thin intimal layer and the IEL with fenestral pores in modulating the transport process in the artery wall, and the effects of transmural pressure on the arterial transport properties. This study has hopefully provided new insights into the mechanisms relating intimal transport and the formation of the early foam cell lesion.

Chapter 2 has been published as a paper entitled "A Fiber Matrix Model for the Growth of Macromolecular Leakage spots in the Arterial Intima" in the *Journal of Biomedical Engineering*, 116: 430-445, 1994. This paper received 1996 Melville Medal from The American Society of Mechanical Engineers (ASME) and 1995/1996 Best Paper Award from the Bioengineering Division of ASME. Chapters 3 has been accepted for publication in the *American Journal of Physiology*. The title is "A Fiber Matrix Model for the Filtration through Fenestral Pores in a Compressible Arterial Intima". The material in Chapter 4 will also be submitted for publication.

Appendix A

All coefficients involved in the solutions of the filtration equations are given in the following:

$$\lambda_{1_i}^2 = \frac{L_{pI} + (i-1)L_{pe}}{\eta} \qquad i = 1,2 \tag{A.1}$$

$$\lambda_2 = \frac{L_{pe}}{L_{pe} + L_{pI}} \tag{A.2}$$

$$\lambda_3 = K_1(\lambda_{1_2} R_1) - \frac{K_1(\lambda_{1_2}\xi)}{I_1(\lambda_{1_2}\xi)} I_1(\lambda_{1_2} R_1) \tag{A.3}$$

$$\lambda_4 = \frac{\lambda_{1_2}}{K_0(\lambda_{1_2} R_1) + \dfrac{K_1(\lambda_{1_2}\xi)}{I_1(\lambda_{1_2}\xi)} I_0(\lambda_{1_2} R_1)} \tag{A.4}$$

$$\lambda_5 = \frac{\lambda_4}{\lambda_{1_1}} I_0(\lambda_{1_1} R_1) \tag{A.5}$$

$$\lambda_6 = \lambda_3 \lambda_5 + I_1(\lambda_{1_1} R_1) + \frac{\Delta R}{\eta \lambda_{1_1}} L_{pj} I_0(\lambda_{1_1} R_1) \tag{A.6}$$

$$\lambda_7 = \frac{1}{\lambda_6}(\lambda_2 \lambda_3 \lambda_4 + \frac{\Delta R}{\eta} L_{pj}) \tag{A.7}$$

$$\lambda_8 = \lambda_5\lambda_7 - \lambda_2\lambda_4 \tag{A.8}$$

$$\lambda_9 = \frac{1}{2}L_{pe}(\xi^2 - R_1^2)\frac{\lambda_{1_1}^2}{\lambda_{1_2}^2} \tag{A.9}$$

$$\lambda_{10} = L_{pe}\frac{R_1\lambda_3}{\lambda_{1_2}^2} \tag{A.10}$$

$$a_1' = \frac{\lambda_3\lambda_4}{\lambda_6}\left(\frac{\lambda_{1_1}^2}{\lambda_{1_2}^2} - 1\right) - \frac{\Delta RL_{pj}}{\eta\lambda_6} \tag{A.11}$$

$$a_2' = \lambda_5 a_1' - \lambda_4\left(\frac{\lambda_{1_1}^2}{\lambda_{1_2}^2} - 1\right) \tag{A.12}$$

$$a_1 = -\lambda_7 - a_1' W_m^0 \tag{A.13}$$

$$a_2 = \lambda_8 + a_2' W_m^0 \tag{A.14}$$

$$a_3 = W_m^0 \tag{A.15}$$

$$a_4 = \lambda_2 + \frac{\lambda_{1_1}^2}{\lambda_{1_2}^2} W_m^0 \tag{A.16}$$

The velocity components and pressure distribution in the media are given by

$$U_m^1 = \sum_{n=2}^{\infty} A_n\mu_n J_1(\mu_n r)\frac{\sinh(\mu_n z)}{\sinh(\mu_n)} \tag{A.17}$$

$$W_m^1 = A_1 + \sum_{n=2}^{\infty} A_n \mu_n J_0(\mu_n r) \frac{\cosh(\mu_n z)}{\sinh(\mu_n)} \tag{A.18}$$

$$P_m^1 = A_1 z + \sum_{n=2}^{\infty} A_n J_0(\mu_n r) \frac{\sinh(\mu_n z)}{\sinh(\mu_n)} \tag{A.19}$$

where

$$A_1 = \frac{2L_{pI}}{\xi^2}\left[\left(\frac{\xi^2 - R_1^2}{2}\right)(a_4 - a_3) - \frac{R_1}{\lambda_{1_1}^2} I_1(\lambda_{1_1} R_1) a_1 + \frac{R_1 \lambda_3}{\lambda_{1_2}^2} a_2\right] \tag{A.20}$$

$$A_n = \beta_1\left[-\frac{a_1}{\lambda_{1_1}} E_A(\lambda_{1_1}) + \frac{a_2}{\lambda_{1_2}}\left(E_B(\lambda_{1_2}) + \frac{K_1(\lambda_{1_2}\xi)}{I_1(\lambda_{1_2}\xi)} E_C(\lambda_{1_2})\right) + \beta_2\right] \tag{A.21}$$

$$E_A(\lambda) = \frac{R_1[\mu_n J_1(\mu_n R_1) I_0(\lambda R_1) + \lambda J_0(\mu_n R_1) I_1(\lambda R_1)]}{\lambda^2 + \mu^2} \tag{A.22}$$

$$E_B(\lambda) = -\frac{\mu_n R_1 J_1(\mu_n R_1) K_0(\lambda R_1)}{\lambda^2 + \mu_n^2} + E_D(\lambda) \tag{A.23}$$

$$E_C(\lambda) = \frac{\lambda \xi J_0(\mu_n \xi) I_1(\lambda \xi)}{\lambda^2 + \mu^2} - E_A(\lambda) \tag{A.24}$$

$$E_D(\lambda) = -\frac{\lambda \xi J_0(\mu_n \xi) K_1(\lambda \xi) - \lambda R_1 J_0(\mu_n R_1) K_1(\lambda R_1)}{\lambda^2 + \mu_n^2} \tag{A.25}$$

$$\beta_1 = \frac{2L_{PI}}{\mu_n \coth(\mu_n) \xi^2 J_0^2(\mu_n \xi)} \tag{A.26}$$

$$\beta_2=(a_3-a_4)\frac{R_1}{\mu_n}J_1(\mu_n R_1) \qquad \textbf{(A.27)}$$

$J_m(x)$, $I_m(x)$ and $K_m(x)$ (m=0,1) are the mth order regular and modified Bessel functions of the first and second kind, respectively. μ_n (n=1,2 ...) are the roots of eigenvalue equation $J_1(\mu_n\xi)=0$.

Appendix B

This Appendix gives the coefficients involved in the solution (12)-(17) of the boundary value problem in the text.

For matching condition (11a) and (11b),

$$A_n=\alpha_m(W_f^*/P_0^*)E_n \qquad n=1,2,...,\infty \tag{B.1}$$

$$B_n=\alpha_i(W_f^*/P_0^*)F_n \qquad n=1,2,...,\infty \tag{B.2}$$

where

$$E_1=\frac{1}{\xi_I^2} \tag{B.3}$$

$$E_n=\frac{2J_1(\mu_n)}{h_m\xi_I^2\mu_n^2\coth(\mu_n h_m)J_0^2(\mu_n\xi_I)} \qquad n=2,3,...,\infty \tag{B.4}$$

$$F_n=-\frac{2J_1(\lambda_n)}{h_i\xi_I^2\lambda_n^2\tanh(\lambda_n h_i)J_1^2(\lambda_n\xi_I)} \qquad n=1,2,...,\infty \tag{B.5}$$

$$\alpha_i=\frac{\mu L_i^*}{K_{P_i}} \quad and \quad \alpha_m=\frac{\mu L_m^*}{K_{P_m}}. \tag{B.6}$$

For matching condition (11a), W_f^* is

$$W_f^* = \frac{P_0^*}{\alpha_m \sum_{n=1}^{\infty} E_n - \alpha_i \sum_{n=1}^{\infty} F_n}. \tag{B.7}$$

For matching condition (11b), W_f^* is

$$W_f^* = \frac{P_0^*}{\alpha_m [E_1 + 2\sum_{n=2}^{\infty} \frac{E_n}{\mu_n} J_1(\mu_n)] - 2\alpha_i \sum_{n=1}^{\infty} \frac{F_n}{\lambda_n} J_1(\lambda_n)}. \tag{B.8}$$

In the case of matching condition (11c),

$$A_n = G_n(a_0 I_{m1}^n + c_0 I_{m3}^n + d_0 I_{m4}^n) \qquad n = 1,2,...,\infty \tag{B.9}$$

$$B_n = -H_n(a_0 I_{i1}^n + c_0 I_{i3}^n + d_0 I_{i4}^n) \qquad n = 1,2,...,\infty \tag{B.10}$$

where

$$G_1 = \frac{2\alpha_m}{\xi_l^2} \tag{B.11}$$

$$G_n = \frac{2\alpha_m}{h_m \xi_l^2 \mu_n \coth(\mu_n h_m) J_0^2(\mu_n \xi_l)} \qquad n = 2,3,...,\infty \tag{B.12}$$

$$H_n = \frac{2\alpha_i}{h_i \xi_l^2 \lambda_n \tanh(\lambda_n h_i) J_1^2(\lambda_n \xi_l)} \qquad n = 1,2,...,\infty \tag{B.13}$$

and

$$I_{mk}^{1}=\int_{0}^{1} r^{k}dr \qquad k=1,3,4 \tag{B.14}$$

$$I_{mk}^{n}=\int_{0}^{1} r^{k}J_0(\mu_n r)dr, \qquad k=1,3,4, \quad n=2,3,...,\infty \tag{B.15}$$

$$I_{ik}^{n}=\int_{0}^{1} r^{k}J_0(\lambda_n r)dr, \qquad k=1,3,4, \quad n=1,2,...,\infty, \tag{B.16}$$

which admit analytic evaluation for any n. k.

The coefficients a_0. c_0 and d_0 are the solutions of the following algebraic equations

$$\begin{aligned} b_{11}a_0+b_{13}C_0+b_{14}d_0&=1\\ b_{21}a_0+b_{23}C_0+b_{24}d_0&=0\\ b_{31}a_0+b_{32}C_0+b_{33}d_0&=0. \end{aligned} \tag{B.17}$$

where

$$b_{1k}=\sum_{n=1}^{\infty}(G_n I_{mk}^{n}+H_n I_{ik}^{n}) \qquad k=1,3,4 \tag{B.18}$$

$$b_{2k}=Q_k(0.5) \qquad k=1,3,4 \tag{B.19}$$

$$b_{3k}=Q_k(0.9) \qquad k=1,3,4 \tag{B.20}$$

$$Q_k(r)=\sum_{n=1}^{\infty}\{[1-J_0(r\mu_n)]G_n I_{mk}^{n}+[1-J_0(r\lambda_n)]H_n I_{ik}^{n}\}-[1-J_0(r\mu_n)]G_1 I_{mk}^{1} \tag{B.21}$$

Bibliography

1 Adamson, R. H. Permeability of Frog Mesenteric Capillaries After Partial Pronase Digestion of the Endothelial Glycocalyx. *J. Physiol.* 428: 1-13, 1990.

2 Adamson, R. H., and G. Clough. Plasma Proteins Modify the Endothelial Cell Glycocalyx of Frog Mesenteric Microvessels. *J. Physiol.* 445: 473-486, 1992.

3 Baldwin, A. L., and L. M. Wilson. Endothelium Increases Medial Hydraulic Conductance of Aorta, Possibly by Release of EDRF. *Am. J. Physiol.* 264: H26-H32, 1993.

4 Baldwin, A. L., and Chien, S. Effects of Dextran 40 on Endothelial Binding and Vesicle Loading of Ferritin in Rabbit Aorta. *Arteriosclerosis* 8: 140-146, 1988.

5 Baldwin, A. L., L. M. Wilson, and B. R. Simon. Effect of Pressure on Hydraulic Conductance. *Arteriosclerosis and Thrombosis* 12: 163-171, 1992.

6 Bird, R., Stewart, W., and Lightfoot, E. *Transport Phenomena* New York, Wiley, 1960.

7 Bratzler, R. L., Chisolm, G. M., Colton, C. K., Smith, K. A.,and Lees, R. S. The Distribution of Labeled Low Density Lipoproteins Across the Rabbit Thoracic Aorta In Vivo *Atherosclerosis* 28 289-308, 1977.

8 Buckwalter, J. A., and Rosenberg, L. C. Electron Microscopic Studies of Cartilage Proteoglycans *The Journal of Biological Chemistry* 257 (16): 9830-9839, 1982.

9 Bundgaard, M. The Three-Dimensional Organization of Tight Junctions in a Capillary Endothelium Revealed by Serial-Section Electron Microscopy *J. Ultra. Res.* 88: 1-7, 1984.

10 Bundgaard, M., Frokjaer-Jensen, J., and Crone, C. Endothelial Plasmalemmal Vesicles as Elements in a System of Branching Invaginations from the Cell Surface. *Proc. Natl. Acad. Sci.* 276: 6439, 1979.

11 Bundgaard, M., Hagman, P., and Crone, C. The Three-Dimensional Organization of Plasmalemmal Vesicular Profiles in the Endothelium of Rat heart Capillaries. *Microvasc. Res.* 25: 358-368, 1983.

12 Campbell. G. J.. P. Eng. M. A. Sc., and M. R. Roach. Fenestrations in the Internal Elastic Lamina at Bifurcation of Human Cerebral Arteries. *Stroke* 112 (4): 489-496. 1981.

13 Carew. T. E.. D. C. Schwenke. and D. Steinberg. Antiatherogenic Effect of Probucal Unrelated to Its Hypocholesterolemic Effects: Evidence That Antioxidant in vivo can Selectively Inhibit Low density Lipoprotein Degradation in Macrophage-Rich Fatty Streaks and Slow the Progression of Atherosclerosis in the Watanabe Heritable Hyperlipidemic Rabbit. *Proc. Natl. Acad. Sci. USA. Medical Sciences* 84: 7725-7729. 1987.

14 Chien. S.. Laufer. L.. and Handley. D. A. Vesicle Distribution in the Arterial Endothelium Determined with Ruthenium as an Extracellular Marker. *J. Ultrastr. Res.* 79: 198-206. 1982.

15 Chien. S.. Lin. S.. Weinbaum. S.. Lee. M. M. L.. and Jan. K. The Role of Arterial Endothelial Cell Mitosis in Macromolecular Permeability *Advances in Experimental Medicine and Biology* 242: 59-73. 1988.

16 Chuang. P.. J. Cheng. S. Lin. K. Jan. D. Wang. and S. Chien. Macromolecular transport Across Arterial and Venous Endothelium in Rats: Studies with Evans Blue-Albumin and Horseradish Peroxidase. *Arteriosclerosis* 10: 188-197. 1990.

17 Clark. J. M.. and Glagov. S. Luminal Surface of distended Arteries by Scanning Electron Microscopy. Elimination of Continuational and Technical Artefacts. *Br. J. Exp. Pathol.* 57: 129-135. 1976.

18 Curmi. P. A.. L. Juan. and A. Tedgui. Effect of Transmural Pressure on Low Density Lipoprotein and Albumin Transport and Distribution Across the Intact Arterial Wall. *Circ. Res.* 66:1692-1702. 1990.

19 Curry. F. E. Mechanics and Thermodynamics of Transcapillary Exchange. *Handbook of Physiology* Section 2. The Cardiovascular System. Vol. 4. Microcirculation. American Physiology Society. Bethesda. MD. 309-374. 1984.

20 Curry. F. E. Determinants of Capillary Permeability: A Review of Mechanism Based on Single Capillary Studies in the Frog *Circulation Research* 59:(4) 367-380. 1986.

21 Curry. F. E.. and C. C. Michel. A Fiber Matrix Model of Capillary Permeability. *Microvascular Research* 20: 96-99. 1980.

22 Davies. P. F.. and Bowyer. D. E. Scanning Electron Microscopy: Arterial Endothelial Integrity After Fixation at Physiological Pressure. *Atherosclerosis*

21: 463-469, 1975.

23 Drumond, M. C., and W. M. Deen. Structural determinants of glomerular hydraulic permeability. *Am. J. Physiol.* 266 (*Renal Fluid Electrolyte Physiol.* 35): F1-F12, 1994.

24 Dunmore, P. J., S. H. Song, and M. R. Roach. A Comparison of the Size of Fenestrations in the Internal Elastic Lamina of Young and Old Porcine Aortas as Seen with the Scanning Electron Microscope. *Can. J. Physiol. Pharmacol.* 68: 139-143, 1990.

25 Ethier, C. R. and Kamm, R. D. *PhysicoChemical Hydrodynamics* 11: 11, 1989.

26 Frank, J. S., and A. M. Fogelman. Ultrastructure of the Intima in WHHL and Cholesterol-Fed Rabbit Aortas Prepared by Ultra-Rapid Freezing and Freeze-Etching," *Journal of Lipid Research* 30: 967-978, 1989.

27 Fry, D. L. Effect of Pressure and Stirring on In Vitro Aortic Transmural ^{125}I-Albumin Transport *American Journal of Physiology* 245: H977-H991, 1983.

28 Fry, D. L. Mathematical Models of Arterial Transmural Transport *American Journal of Physiology* 248: H240-H263, 1985.

29 Fry, D. L. Mass transport, Atherogenesis, and Risk *Arteriosclerosis* 7: 88-100, 1987.

30 Fry, D. L., J. F. Cornhill, H. Sharma, J. M. Pap, and J. Mitschelen. Uptake of Low Density Lipoprotein, Albumin, and Water by Deendothelialized In Vitro Minipig Aorta. *Arteriosclerosis* 6: 475-490, 1986.

31 Happel, J., and H. Brenner. *Low Reynolds Number Hydrodynamics, with Special Application to Particulate Media* Englewood Cliffs, N.J., Prentice-Hall, 392-404, 1965.

32 Holman, J. P., *Heat Transfer* sixth edition, McGraw-Hill, New York, 647, 1986.

33 Huang, Y., D. Rumschitzki, S. Chien, and S. Weinbaum. A Fiber Matrix Model for the Growth of Macromolecular Leakage Spots in the Arterial Intima *Journal of Biomechanical Engineering* 116: 430-445, 1994.

34 Huang, Y., D. Rumschitiki, S. Chien, and S. Weinbaum. A Fiber Matrix Model for the Filtration through Fenestral Pores in a Compressible Arterial Intima. *Am. J. Physio.: Heart and Circulatory Physiology*. In press.

35 Kim. W-S.. and J. M. Tarbell. Macromolecular Transport through the Deformable Porous Media of Artery Wall *Journal of Biomechanical Engineering* 116: 156-163, 1994.

36 Klanchar, M., and J. M. Tarbell. Modeling Water Flow Through Arterial Tissure. *Bulletin of Mathematical Biology* 49: (6) 651-669. 1987.

37 Lark. M. W.. T. Yeo. H. Mar. S. Lara. I. Hellström. K. Hellström. and T. N. Wight. Arterial Chondroitin Sulfate Proteoglycan: Localization with a Monoclonal Antibody. *The Journal of Histochemistry and Cytochemistry* 36: 1211-1221. 1988.

38 Lee. M. M.. and S. Chien. Morphologic Effects of Pressure Changes on Canine Carotid Artery Endothelium as Observed by Scanning Electron Microscopy. *ANAT. REC.* 194: 1-14. 1979.

39 Lever. M. J.. and N. Sharifi. The Effects of Transmural Pressure and Perfusate Albumin Concentration on the Hydraulic Conductivity of the Isolated Rabbit Common Carotid Artery (Abstract). *J. Physiol. Lond.* 387: 68P. 1987.

40 Levick. J. R. Flow through Interstitium and Other Fibrous Matrices *Quarterly Journal of Experimental Physiology* 72: 409-438. 1987.

41 Lin. S.. Jan. K.. and Chien. S. Role of Dying Endothelial Cells in Transendothelial Macromolecular Transport *Arteriosclerosis* 10 (5): 703-709. 1990.

42 Lin. S.. K. Jan. G. Schuessler. S. Weinbaum. and S. Chien. Enhanced Macromolecular Permeability of Aortic Endothelial Cells in Association with Mitosis. *Arteriosclerosis* 73: 223-232. 1988.

43 Lin. S.. Jan. K.. Weinbaum. S.. and Chien. S. Transendothelial Transport of Low Density Lipoprotein in Association with Cell Mitosis in Rat Aorta *Arteriosclerosis* 9: 230-235. 1989.

44 Michel. C. C. Capillary Permeability and How It May Change. *J.Physiol.* 404: 1-29. 1988.

45 Nerem. R. M.. and Levesque. M. J. The Case for Fluid Dynamics as a Localizing Factor in Atherogenesis *Fluid Dynamics as Localizing Factor for Atherosclerosis*. Schettler. G.et al.eds..Springer-Verlag. Berlin. 1983. pp.26-37.

46 Nievelstein. P. F.E.M.. A. M. Fogelman. G. Mottino. and J. S. Frank. Lipid Accumulation in Rabbit Aortic Intima 2 Hours After Bolus Infusion of Low

Density Lipoprotein: A Deep-Etch and Immunolocalization Study of Ultrarapidly Frozen Tissue. *Arteriosclerosis and Thrombosis* 11:(6) 1795-1805. 1991.

47 Ogston. A. G., Preston. B. N., and Wells. J. D. On the Transport of Compact Particles Through Solutions of Chainpolymers *Proc. R. Soc. London Ser.* A 333: 297-316. 1973.

48 Potter. R. F., and M. R. Roach. Are Enlarged Fenestrations in the Internal Elastic Lamina of the Rabbit Thoracic Aorta Associated with Poststenotic Dilatation? *Can. J. Physiol. Pharmacol.* 61: 101-104. 1983.

49 Reidy. M. A., and Schwartz. S. M. Developments in the Study of endothelial Cells by Scanning Electron Microscopy. *Artery* 8: 236-243. 1980.

50 Ross. R. The Pathogenesis of Atherosclerosis-An Update. *New England Journal of Medicine* 314: 488-500. 1986.

51 Ross. R., and Glomset. J. The Pathogenesis of Atherosclerosis *New England J. Med.* 295: 420-425. 1976.

52 Sampson. R. A. *Phil. Trans. R. Soc. Lond.* A 182: 449. 1891.

53 Sangani. A. S., and Acrivos. A. Slow Flow Past Periodic Arrays of Cylinders with Application to Heat Transfer *Int. J. Multiphase Flow* 8: 193-206. 1982.

54 Schwenke. D.C., and Carew. T.E. Initiation of Atherosclerotic Lesions in Cholesterol-fed Rabbits. I. Focal Increases in Arterial LDL Concentration Precede Development of Fatty Streak Lesions *Arteriosclerosis* 9: 895-907. 1989.

55 Seifter. S. and P. M. Gallop. *The Proteins* (H.Neurath. ed.). Vol. 4. Chapter 20. Academic Press. New York. 1966.

56 Short. C., C. Gochard. and M. J. Lever. Interstitial Fluid Transport through Wall Tissue of Arteries and Veins. *J. Physio.* 483.P: 146P-147P. 1995.

57 Simionescu. N., Mora. R., Vasile. E., Lupu. F., Filip. D.A., and Simionescu. M. Prelesional Modifications of the Vessel Wall in Hyperlipidemic Atherogenesis *Ann.N.Y.Acad.Sci.* 598: 1-16. 1990.

58 Simionescu. N., Simionescu. M., and Palade. G. E. Structural Basis of Permeability in sequential Segments of the Microvasculature. II. Pathways Followed by Microperoxidase Across the Endothelium. *Microvasc. Res.* 15: 17-36. 1978.

59 Simionescu, N., E. Vasile, F. Lupo, G. Popescu, and M. Simionescu. Prelesional Events in Atherogenesis. Accumulation of Extracellular Cholesterol-Rich Liposomes in the Arterial Intima and Cardiac Valves of the Hyperlipidemic Rabbit *Am. J. Pathol.* 123: 1109-1125, 1986.

60 Smith, E. B., and Staples, E. M. Plasma Protein Concentrations in Interstitial Fluid from Human Aortas *Proceeding of Roy. Soc. London*, Series B, 217: 59-75, 1982.

61 Song, S. H., and M. R. Roach. Quantitative Changes in the Size of Fenestrations of the Elastic Laminae of Sheep Thoracic Aorta Studied with SEM. *Blood Vessels* 20: 145-153, 1983.

62 Song, S. H., and M. R. Roach. Comparison of Fenestrations in Internal Elastic Lamina of Canine Thoracic and Abdominal Aortas. *Blood Vessels* 21: 90-97, 1984.

63 Steinberg, D., S. Parthasarathy, T. E. Carew, J. C. Khoo, and J. L. Witztum. Modifications of Low-Density Lipoprotein that Increase its Atherogenicity. *New England J. of Medicine* 320: 915-924, 1989.

64 Stemerman, M. B., Morrel, E. M., Burke, K. R., Colton, C. K., Smith, K. A., and Lees, R. S. Local Variation in Arterial Wall Permeability to Low Density Lipoprotein in Normal Rabbit Aorta *Arteriosclerosis* 6: 64-69, 1986.

65 Tedgui, A., and M. J. Lever. Filtration Through Damaged and Undamaged Rabbit Thoracic Aorta *American Journal of Physiology* 247: H784-H791, 1984.

66 Tedgui, A., and Lever, M. J. The Interaction of Convection and Diffusion in the Transport of ^{131}I-Albumin within the Media of Rabbit Thoracic Aorta *Circulation Research* 57: 856-863, 1985.

67 Tedgui, A., and M. J. Lever. Effect of Pressure and Intimal Damage on ^{131}I-Albumin and [^{14}C]Sucrose Spaces in Aorta. *American Journal of Physiology* 253: H1530-H1539, 1987.

68 Tompkins, R. G., Yarmush, M. L., Schnitzer, J. J., Colton, C. K., Smith, K. A., and Stemerman, M. B. Low-Density Lipoprotein Transport in Blood Vessel Walls of Squirrel Monkeys *American Journal of Physiology* 257: H452-H464, 1989.

69 Truskey, G. A., C. K. Colton, and K. A. Smith. Quantitative Analysis of Protein Transport in the Arterial Wall. *Structure and Function of the Circulation* 3: 287-355, 1981, edited by Schwartz, C. J., Werthessen, J. T. and Wolf, S., Plenum

Publishing Corporation. New York.

70 Truskey. G. A.. W. L. Roberts. R. A. Herrmann. and R. A. Malinauskas. Measurement of Endothelial Permeability to ^{125}I-Low Density Lipoproteins in Rabbit Arteries by Use of En Face Preparations *Circulation Research* 71:(4) 883-897. 1992.

71 Tsay. R.. and S. Weinbaum. Viscous Flow in a Channel with Periodic Cross-Bridging Fibers: Exact Solutions and Brinkman Approximation. *Journal of Fluid Mechanics* 226: 125-148. 1991.

72 Tsay. R.. Weinbaum. S.. and Pfeffer. R. A New Model for Capillary Filtration Based on Recent Electron Microscopic Studies of Endothelial Junctions *Chemical Engineering Communication* 82: 67-102. 1989.

73 Tzeghai. G.. Ganatos. P.. Pfeffer. R.. Weinbaum S.. and Nir. A. A Theoretical Model to Study the Effect of Convection and Leaky Junctions on Macromolecular Transport in Artery Walls *Journal of Theoretical Biology* 121: 141-162. 1986.

74 Underwood. E. E. Quantitative Stereology *Addison-Wesley Publishing Company* 1970.

75 Vargas. C. B.. F. F. Vargas. J. G. Pribyl. and P. L. Blackshear. Hydraulic Conductivity of the Endothelial and Outer Layers of the Rabbit Aorta. *Am. J. Physiol.* 236: H53-H60. 1979.

76 Wakeham. W. A.. Salpadoru. N. H.. and Cao. C. G. Diffusion Coefficients for Protein Molecules in Blood Serum *Atherosclerosis* 25: 225-235. 1976.

77 Walton. A. G. and J. Blackwell. *Biopolymers* Academic Press. New york. 433-439. 1973.

78 Weibel. E. R. *Morphometry of the Human Lung*. Berlin: Spring-Verlag. 1963.

79 Weinbaum. S.. and S. Chien. Lipid Transport Aspects of Atherogenesis. *J. Biomech. Engr.* 115: 602-610. 1993.

80 Weinbaum. S.. Pfeffer. R.. and Chien. S. The Search for the Large Endothelial Pore and Its Possible Link to the Localization of Atherogenesis. PCH *PhysicoChemical Hydrodynamics* 10: 705-726. 1988 a.

81 Weinbaum. S.. Tsay. R.. and Curry. F. E. A Three-Dimensional Junction-Pore-Matrix Model for Capillary Permeability *Microvascular Research* 44: 85-111.

1992.

82 Weinbaum, S., Tzeghai, G., Ganatos, P., Pfeffer, R., and Chien, S. Effect of Cell Turnover and Leaky Junctions on Arterial Macromolecular Transport *American Journal of Physiology* 248: H945-H960, 1985.

83 Weinbaum, S., Wen, G., Ganatos, P., Pfeffer, R., Lee, M.M.L., and Chien, S. On the Time-Dependent Diffusion of Macromolecules Through Transient Open Junctions and Their Subendothelial Spread, I. Short-Time Model for Cleft Exit Region *Journal of Theoretical Biology* 135: 1-30, 1988 b.

84 Wen, G., S. Weinbaum, P. Ganatos, R. Pfeffer, and S. Chien. On the Time-Dependent Diffusion of Macromolecules Through Transient Open Junctions and Their Subendothelial Spread, II. Long-Time Model for Interaction Between Leakage Sites. *J. Theor. Physiol.* 135: 219-253, 1988.

85 Wight, T. N., and V. C. Hascall. Proteoglycans in Primate Arteries. III. Characterization of the Proteoglycans Synthesized by Arterial Smooth Muscle Cells in Culture *J. Cell Biol.* 96: 167-176, 1983.

86 Wu, C., Chi, J., Jerng, J., Lin, S., Jan, K., Wang, D., and Chien, S. Transendothelial macromolecular Transport in the Aorta of Spontaneously Hypertensive Rats *Hypertension* 16: 154-161, 1990.

87 Yin, Y., K. Lim, S. Weinbaum, S. Chien, and D. Rumschitzki. A Model for the Initiation and Growth of extracellular Lipid Liposomes in Arterial Intima. *Am. J. Physiol.* in review.

88 Yuan, F., S. Chien, and S. Weinbaum. A New View of Convective-Diffusive Transport Processes in the Arterial Intima. *J. Biomech. Engr.* 113: 314-329, 1991.

89 Zeng, Y. and S. Weinbaum. Stokes Flow through Periodic Orifices in a Channel. *J. Fluid Mech.* 263: 207-226, 1994.